Project 09-792

Viscosity Measurement Technique for Metal Fuels

Integrated University Programs

Dr. Heng Ban
Utah State University

In collaboration with:
Idaho National Laboratory

Jon Carmack, Technical POC

National Nuclear Security Administration

Final Technical Report

Viscosity Measurement Technique for Metal Fuels

BEA Standard Research Subcontract No. 00091896

Heng Ban, PhD, PE

Mechanical and Aerospace Engineering

Utah State University

4130 Old Main Hill, Logan, UT 84322

Heng.ban@usu.edu

June 15, 2014

DISCLAIMER

ABSTRACT

Metallic fuels have exceptional transient behavior, excellent thermal conductivity, and a more straightforward reprocessing path, which does not separate out pure plutonium from the process stream. Fabrication of fuel containing minor actinides and rare earth (RE) elements for irradiation tests, for instance, U-20Pu-3Am-2Np-1.0RE-15Zr samples at the Idaho National Laboratory, is generally done by melt casting in an inert atmosphere. For the design of a casting system and further scale up development, computational modeling of the casting process is needed to provide information on melt flow and solidification for process optimization. Therefore, there is a need for melt viscosity data, the most important melt property that controls the melt flow. The goal of the project was to develop a measurement technique that uses fully sealed melt sample with no Americium vapor loss to determine the viscosity of metallic melts and at temperatures relevant to the casting process. The specific objectives of the project were to: develop mathematical models to establish the principle of the measurement method, design and build a viscosity measurement prototype system based on the established principle, and calibrate the system and quantify the uncertainty range. The result of the project indicates that the oscillation cup technique is applicable for melt viscosity measurement. Detailed mathematical models of innovative sample ampoule designs were developed to not only determine melt viscosity, but also melt density under certain designs. Measurement uncertainty were analyzed and quantified. The result of this project can be used as the initial step toward the eventual goal of establishing a viscosity measurement system for radioactive melts.

TABLE OF CONTENTS

LIST OF FIGURES

LIST OF TABLES

1. INTRODUCTION

The National Energy Policy (NEP) recommends that the United States "develop reprocessing and fuel treatment technologies that are cleaner, more efficient, less waste-intensive, and more proliferation-resistant." The mission of the U.S. Department of Energy’s (DOE) Fuel Cycle R&D (FCRD) program is to develop fuel cycle technologies that will meet the need for economic and sustained nuclear energy production while satisfying requirements for controlled proliferation-resistant nuclear materials management system. FCRD is designed to develop new technologies so they may be deployed to support the operation of current nuclear power plants, including advanced light water reactors and Generation IV advanced reactors. Deployment of new fuel cycle technologies is necessary in order for the U.S. to achieve a significant reduction in the amount of high-level radioactive waste that requires geologic disposal, to reduce significantly accumulated plutonium in civilian spent fuel, and to extract more useful energy from nuclear fuel.

One of FCRD's goals has been to develop and demonstrate advanced, proliferation-resistant fuel cycle technologies for treatment of commercial light water reactor spent fuel and to develop an integrated spent fuel recycling plan. In the longer term, FCRD’s development of a system involving spent-fuel partitioning and recycling of actinides (highly-radioactive materials contained in spent fuel) and other long-lived radioactive components in fast reactors for destruction through transmutation could result in a de facto fifty-fold increase in the technical capacity of the repository. This increase would come principally from the destruction of actinides that generate heat that limits repository capacity. FCRD R&D program has campaigns in separation and waste forms, transmutation fuels, reactors, system analysis, safeguards, and modeling and simulation. FCRD fuels campaign develops for qualification of transmutation fuels for use in recycling reactors over a range of potential compositions in order to enable closure of the fuel cycle while maintaining the commercial competitiveness of nuclear energy. A key research need for FCRD fuels is advanced fabrication techniques that are capable of remote and industrial scale operation with low losses and performance of the fuel during irradiation.

Metallic fuels have exceptional transient behavior, excellent thermal conductivity, and a more straightforward reprocessing path, which does not separate out pure plutonium from the process stream. U-Pu-Zr based alloy fuels have outstanding reactor core performance, simplicity of reprocessing and fuel-fabrication, and low fuel cycle cost even in a relatively small-scale fuel cycle plant. One of the key challenges for metal fuel fabrication is the demonstration of an advanced casting system that incurs low americium vapor loss. Metallic fuel has been fabricated through a variety of processes. Rolling and swaging to size, co-extrusion with the cladding, or centrifugal casting were used for fuel fabrication for the Experimental Breeder Reactor I (EBR-I). The most extensive experience with fuel casting in the U.S. was with the Experimental Breeder Reactor II (EBR-II) fuel, which was cast through counter gravity injection casting into precision bored glass molds. This method was used to cast fuel for EBR-II throughout its life and was found to be reliable in both remote and "hands-on" operation. However, the addition of minor actinides, particularly americium, to the fuel introduces complications not easily dealt with using counter gravity injection casting. During counter gravity injection casting the melt is placed under a vacuum, which due to the high vapor pressure of americium, leads to americium losses from the fuel because of volatilization. In order for metallic fuel to be used for transmutation purposes, a casting system must be developed which will retain americium during the casting cycle.

Fabrication of fuel rodlets containing minor actinides and rare earth (RE) additions (for instance, U-20Pu-3Am-2Np-1.0RE-15Zr) for irradiation tests was performed by arc melting and casting at the Idaho National Laboratory (INL). The casting was conducted in an inert atmosphere (argon) glovebox using an electric discharge plasma arc melter with a suction or gravity drop casting method. The feedstock materials were melted and thoroughly homogenized. The slug dimensions for the fuels cast were approximately 5 cm in length and 4.9 mm in diameter. Currently, an induction heated, pressure differential assisted, bottom pour casting system is being developed at INL at bench scale. Americium retention will be accomplished by reducing the application of vacuum, covering the crucible, and utilizing short melt cycles.

For the optimal design of a casting system and further scale up development, computational modeling of the casting process is needed to provide information on melt flow and solidification for process optimization. Model development for metal fuel casting has been initiated at Los Alamos National Laboratory (LANL). The most important melt property that controls the melt flow is its viscosity. However, there is no data available on the viscosity of metal fuel melts and there is no commercial measurement system available to perform such measurements.

2. METALLIC FUEL AND VISCOSITY BACKGROUND

Currently, the FCRD fuels program is focused on and principally interested in the development of oxide and metal alloy fuel systems. This includes improvement of the fundamental understanding of fuel behavior through characterization of microstructure, chemistry, and thermophysical properties of unirradiated fuel specimens, and the integration of these studies with theory and simulation. Of primary interest in fuels fabrication is the development of industrially viable, remote fabrication processes for oxide and metal alloy fuels, which have minimal losses of fuel material and generate a minimal amount of secondary waste.

The primary metal fuel of interest is U-Pu-Zr system, with additions of the minor actinides and rare earth elements. Argonne National Laboratory (ANL) conducted some studies relative to phase diagram development and some thermophysical property determination (density, heat capacity) for a number of concentrations (Ofte, 1965, Zegler 1965 Grove, 1966, 1967). After those limited measurements done in the 1960s, there were few studies until the FCRD program initiated its thermal properties effort in the early 2000's (Kennedy, 2004,). The lack of information on thermophysical and thermomechanical properties and the knowledge about these alloy fuels presents a significant challenge for the development of advanced fuels.

The U-Zr binary alloy system is an important subsystem of the U-Pu-Zr ternary alloy, and also the starting fuel composition. Figure 1 shows the phase diagram of the system (Massalski, 1986). However, available data of the U-Zr system are sparse. Thermodynamics of the U-Zr alloy such as phase identification, stability and transition has been studied more than thermophysical properties. Fedorov et al. (Federov, 1968) measured heat capacity of U-Zr from room temperature to 1123 K. However, their data is generally believed to be too large in comparison with those estimated from those of uranium and zirconium using the additivity law and did not clearly show the existence of four phase transitions indicated in the phase diagram. For instance, above 870 K, U(γ)Zr(β) solid solution is formed. Japanese researchers later obtained more reasonable data for heat capacity at elevated temperatures (Nakamura, 1980). Rodríguez (Rodríguez, 1994) measured melting points, phase transformations, and the phase relationships of U-Zr-Np using dilatometry and electron probe microanalysis. Kanno et al. (Kanno, 1988) measured the absolute vapor pressures and the thermodynamic activities of both liquid and solid solutions in the temperature range 1700-1800 K. Takahashi et al. (Takahashi, 1988, 1989) measured the thermal diffusivity and heat capacity of four U-Zr alloys from 300-1100 K, including the temperature region of phase transitions of these alloys. Matsui et al. (Matsui, 1989) also measured the heat capacity and electrical conductivity of U0.8Zr0.2 from 300-1300 K, and calculated the thermal conductivity based on thermal diffusivity data, as well as the Wiedemann-Franz's Law using electrical conductivity. These thermophysical property measurements, performed in Europe and Japan about twenty years ago, did not include viscosity. In the US, early work in 1960sm collected in Touloukian's database (Touloukian, 1967), still represent the best available information for thermophysical properties. It is apparent that such scattered and scarce data points fall far short of the need for the renewed effort in alloy fuel development under FCRD. The lack of viscosity information makes it imperative to develop a viscosity measurement capability for the alloy fuels to be fabricated and tested. Viscosity can also contribute to the basic understanding and broad knowledge of the alloy systems, in addition to enabling fuel fabrication and fuel casting design and optimization.

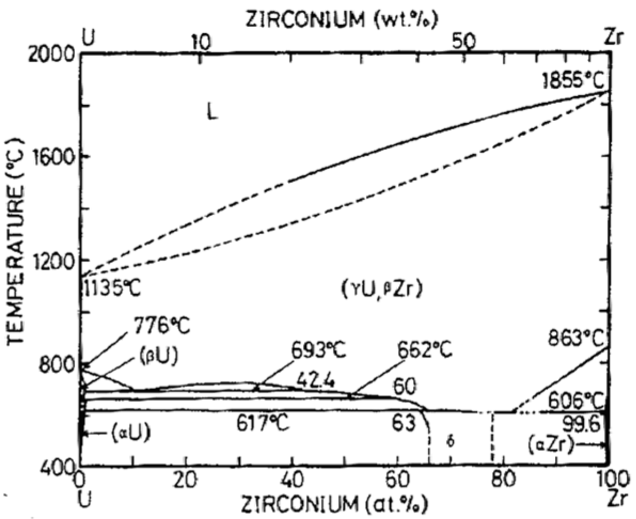

FIGURE 2: PHASE DIAGRAM OF U-ZR SYSTEM.

The measurement of viscosity at high temperatures is quite challenging. Iida published the review on the properties including viscosity and density of molten metals (Iida, 1988), and the comparison among the viscosities of molten iron reported by many researchers showed considerable difference of several dozen percent. The method for measurements should be chosen carefully by considering physical and chemical properties of the melt. Three types of measurement techniques, i.e., the capillary, oscillation cup, and rotation methods are commonly used to measure liquid viscosity at high temperatures. Another method, the falling sphere method, is not applicable here because it requires synchrotron X-rays to observe sphere movement in the melt. The capillary method can only be used at temperatures less than 1000 C, which is too low for this proposed project as Figure 1 shows that the U-Zr system melts at above 1135 C. The oscillating method and rotating method can be used at temperatures above 1000 C. Rotating spindle viscometers use an open melt pool and it is applicable to melts with low vapor pressures such as glasses or molten salts, as described in ISO 7884-2 and ASTM C965. The method is less likely to be easily adaptable to glovebox applications. The oscillation cup method is used when the vapor pressure of the melt is high since the sample can be sealed and the volume of sample needed for measurement can be small (Li, 2004, 2005). However, the theoretical and mathematical aspects of the method are complex and there have been only a few of this type of viscometer ever developed in the world. Molten uranium dioxide was measured in the early 1970s in DOE national laboratories with vastly different values (Tsai, 1972, Woodley 1974). Two oscillation systems were developed in the U.S. in last three decades but none are currently operational.

This proposed project aligns well with the technical objectives of the metal fuel casting program of the FCRD fuels campaign. The scope of work of this project is practical with respect to the specified funding range and period of performance listed in the solicitation. Viscosity is the most important parameter for melt processing in casting for fuel rod fabrication. Viscosity information can provide essential science-based understanding of the melt structure and the necessary data for the computational modeling of the casting process.

3. RESEARCH GOALS AND BJECTIVES

The overall goal of research is conduct proof-of-principle studies of the proposed measurement method. The objectives of the project were to: design and develop mathematical models to establish the principle of the measurement method, build a viscosity measurement prototype system based on the established principle, calibrate the system and quantify the uncertainty range, and evaluate its application potential in a glovebox. This includes design, theoretical modeling, construction, testing, calibration, and uncertainty quantification. The following major tasks are to be planned to achieve the specific objectives in project.

Theoretical Model Development

Detailed mathematical models have to be developed for the measurement system as part of the design process, because the system design will rely of the models to determine system parameters. The models are also critical for data processing and system optimization. The uncertainty analysis will also use these models to evaluate measurement uncertainty.

(1) System Design, Construction and Testing

With available technical options for the range of material properties to be measured, such as density, viscosity and electrical conductivity, the experimental system will be designed accordingly. Although the general principle of oscillation method is available, the parameters of measurement system have to be carefully calculated for the new measurement requirements. Due to the increase in operation temperature up to 1000 ^{o}C, most of the components and the system have to be designed to meet the high temperature requirements. In addition to using the transient torque method which requires the electromagnetic field to stir the melt, the design can be also based the oscillation cup method first. For oscillation methods, the sample can be in the furnace and the electromagnetic field is only used to initialize the rotation, which can be realized with an additional conductive component far away from the sample and high temperature zone. Therefore, the electromagnetic field does not need to penetrate the furnace and a commercial high temperature furnace will be used.

This task will modify the initial design as required to resolve issues encountered during construction. The systems will be built and tested. Samples of materials with the similar range of properties and known viscosity will be used for shakedown and calibration of the prototype measurement system, which may be modified depending on the results of the calibration measurement, until an acceptable measurement response is achieved. Measurement repeatability and uncertainty range based on precision and bias uncertainties will be evaluated. The procedure for extracting viscosity data from the measured angular oscillations will be established.

(2) Uncertainty Quantification

Measurement uncertainty will be evaluated based on the design parameters and experimental data. Monte Carlo uncertainty estimation will be performed to quantity the contributions of each parameter to the final uncertainty of the result. Measurement uncertainty of both oscillation cup the transient toque methods will be compared.

4. THEORY AND MATHEMATICAL MODELS

4.1. Introduction

A noncontact rotational technique, called electromagnetic viscometer (EMV), can simultaneously measure the viscosity and electrical conductance of liquid metals at high temperatures. The sample is sealed in a fused silica cup suspended by a quartz fiber. Once a rotational magnetic field (RMF) surrounding the cup is applied, a rotational flow of the sample is triggered, further causing the axial oscillation of the cup. The transient angular motion of the suspension system is measured to determine the electrical conductance and viscosity of fluids.

The EMV has potential to be an important method of measuring viscosities of high temperature electrically conducting fluids. This technique combines the noncontact rotational technique for measuring the electrical conductance (Bakhtiyarov, 1999) and the widely-used oscillating cup viscometers (OCV) for measuring the viscosities (Kehr, 2007, Gruner, 2008, Wang, 2002, Torklep, 1979, Sasaki, 1995, Sato, 1995)). As an improved version of the OCV, the EMV has all advantages of the OCV, such as high measurement accuracy, noncontact inductive technique, and only small amount of sample required. Furthermore, the EMV method has exclusive advantage due to the capability of simultaneous measurements of electrical conductance and viscosity.

To provide better experimental design of EMVs, theoretical study is necessary to improve the understanding its mechanism. Currently there is a lack of theoretical analyses of the EMV, though the theory of the OCV has already been well established since 1950s. The OCV behavior was first modeled by a pair of coupled transcendental equations (Kestin, 1957). Special mathematical treatments were further performed (Roscoe 1958, Beckwith, 1957) to establish a simpler and useful relation between viscosity and measurable parameters, i.e. the decrement and time period of the oscillation. As a newly developed technique, the EMV has not drawn too much attention yet. The only theoretical study relating to the EMV is the numerical modeling in (Li, 2004).

The main objective of this chapter is to establish analytical models for the EMV. On the basis of these models, the EMV behavior is discussed to come up with some application principles. Specific objectives of this work include:

1) Establish an analytic model for 1D EMV, improve understanding of the mechanism, and provide some guidance for experimental design;

2) Establish an analytic model for 2D EMV to improve the accuracy of modeling, perform numerical experiments, and fundamentally optimize the experimental conditions for higher measurement accuracy;

3) Establish an analytic model for a stepped-cylindrical cup EMV, and examine the feasibility of simultaneously measuring density, viscosity and electrical conductance with the EMV method.

4.2. One Dimensional Model

A 1-D EMV model is developed in this section. The relationships between fluids properties and experimental design parameters are discussed aiming to better understand the mechanism of EMVs and to provide some general guidance for future experiment design.

4.2.1. Analytical Model

4.2.1.1. Mathematic and Physical Description

A cylindrical cup with tested fluids enclosed is suspended by a torsional wire and surrounded by a rotational electromagnetic field as schemed in Fig. 4.2.1. The magnetic field which is uniform everywhere, rotates around the centerline of the cup with constant frequency. Once the RMF turns on, the Lorentz force induces a fluid flow, exerting a viscous shear on the inner wall of the cup. The viscous effects interacts with the elastic deformation of the torsional wire, creating an axial oscillation of the cup.

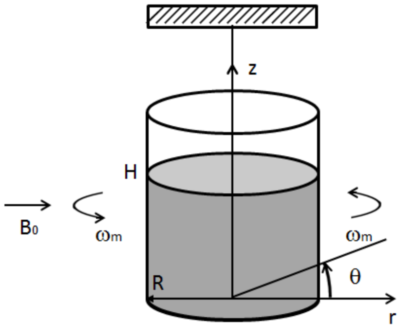

Fig. 4.2.1 Schematic of a single-cylindrical cup EMV

An EMV consists of two physically interacting subsystems: the fluid flow in the cup and the oscillation of the cup assembly. They affect each other through the viscous shear on the inner wall of the cup. On one hand, the fluid motion acts like an engine to trigger and maintain the motion of the cup. At the same time, it adds extra drag to the damping of the cup oscillation. On the other hand, the oscillation of the cup give rise to a similar oscillation in the fluid, especially in the vicinity of the wall. Different governing equations are needed to describe these phenomena. The motion of the cup is governed by,

$$\bar{I}_0\left[\frac{d^2\alpha(\bar{t})}{d\bar{t}^2} + 2\Delta_0\bar{\omega}_0\frac{d\alpha(\bar{t})}{d\bar{t}} + (1+\Delta_0^2)\bar{\omega}_0^2\alpha(\bar{t})\right] = \bar{M}(\bar{t}) \qquad \text{Eq. 4.2.1a)}$$

where $\alpha(t)$ is the angular displacement of the cup away from its initial position. $\bar{\omega}_0$, Δ_0 and $\bar{I}_0$ are the parameters related to the cup assembly in the absence of fluid, namely the damped angular frequency, the damping parameter, and the moment of inertial of the empty cup, respectively. Δ_0 evaluates the rate of the damping due to the internal friction of the suspension wire and the resistance in the surrounding air, and its value is equal to the logarithmic decrement decreasing by a factor of 2π. As the under damping oscillation with $\Delta_0 < 0.01$ is usually applied in measurements, $\mathit{\Delta}_0$ approaches the damping ratio of the oscillation with a difference of less than 0.01%. $\bar{M}(\bar{t})$ is the viscous torque on the inner wall of the cup. The over bar, hereafter, is used to denote the dimensionless quantities.

To investigate the fluid motion, we assume that a) the inertial forces are negligible compared to the viscous forces and b) the interaction at the bottom of the cup is negligible compared to that from the side wall so as to make the 1D assumption. It is reasonable once if the liquid depth is much larger than the inner radius of the cup. Thus, the fluid motion is governed by the 1D Stokes equation with the Lorentz force.

$$\frac{\partial\bar{\mathit{\Omega}}(\bar{r},\bar{t})}{\partial\bar{t}} = \frac{\bar{\sigma}\bar{B}^2}{2\bar{\rho}}(\bar{\omega}_m - \bar{\mathit{\Omega}}(\bar{r},\bar{t})) + \nu\left[\frac{\partial^2\bar{\mathit{\Omega}}(\bar{r},\bar{t})}{\partial\bar{r}^2} + \frac{3}{\bar{r}}\frac{\partial\bar{\mathit{\Omega}}(\bar{r},\bar{t})}{\partial\bar{r}}\right] \qquad \text{Eq. 4.2.1b)}$$

in which, $\bar{\mathit{\Omega}}$ is the angular velocity, $\bar{\sigma}$ is the electrical conductance, $\bar{B}$ is the strength of the RMF and $\bar{\omega}_m$ is the angular frequency of the RMF. The first term in the RHS represents the Lorentz force induced by the RMF, causing the fluid in motion. Because low-frequency RMFs are usually applied, the magnetic field induced by the fluid motion is negligible comparing to the external magnetic field (Volz, 1999). Hence, the Lorentz force is linear to the difference of the rotational rate between the magnetic field and the flow. If getting rid of the Lorentz force term, Eq. 4.2.1b) describes the flow at the situation without RMFs applied, such as in the traditional OCVs.

The viscous torque exerted on the cup is related to the fluid motion,

$$\bar{M}(\bar{t}) = -4\frac{\bar{I}\bar{\nu}}{\bar{R}}\frac{\partial\mathit{\Omega}(\bar{r}=\bar{R},\bar{t})}{\partial\bar{r}} \qquad \text{Eq. 4.2.1c)}$$

in which $\bar{R}$ is the inner radius of the cup, $\bar{\nu}$ the kinetic viscosity, $\bar{I}$ the momentum inertia of the fluid column. $\bar{I} = \frac{\pi}{2}\bar{\rho}\bar{R}^4\bar{H}$, $\bar{\rho}$ is the density of the fluid, and $\bar{H}$ is the depth of the liquid hold in the cup. Again, the viscous torque occurring at the bottom wall is ignored.

Eq. 4.2.1a) and b) are subjected to initial conditions such as:

$$\alpha(\bar{t} = 0) = \alpha_0, \qquad \text{Eq. 4.2. 2a)}$$

$$\bar{\mathit{\Omega}}(\bar{r},\bar{t} = 0) = 0 \qquad \text{Eq. 4.2.2b)}$$

An initial angular displacement α_0 is set in Eq. 4.2.2a), which is suitable for both OCVs and EMVs. In the OCVs, appropriate initial displacement is necessary to start the motion of the cup as well as the fluid. In contrast, the EMVs are at rest before adding the RMF, so that $\alpha_0 = 0$. The fluid is always static for either the OCVs or the EMVs as described by Eq. 4.2.2b).

Bu assuming the no-slip conditions at the interface between the fluid and the cup, Eq. 4.2.1b) is subjected to the following boundary conditions,

$\bar{\Omega}(\bar{r} = \bar{R}, \bar{t}) = \frac{d\alpha(\bar{t})}{d\bar{t}}.$ Eq. 4.2.2c)

The fluid and the cup share the same angular velocity at the interface.

It is convenient to scale the governing equations by introducing the dimensionless parameters

$t = \bar{t}\bar{\omega}_0, M = \frac{\bar{M}}{\bar{I}_0\bar{\omega}_0^2}, \Omega = \frac{\bar{\Omega}}{\bar{\omega}_0}, r = \frac{\bar{r}}{\bar{\delta}}, R = \frac{\bar{R}}{\bar{\delta}}, I = \frac{\bar{I}}{\bar{I}_0}, \omega_m = \frac{\bar{\omega}_m}{\bar{\omega}_0}, Ha = \bar{B}\bar{\delta}\sqrt{\frac{\bar{\sigma}}{\bar{\rho}\bar{\nu}}}.$ Eq. 4.2.3

where $\bar{\delta} = \sqrt{\frac{\bar{\nu}}{\bar{\omega}_0}}$, can be regarded as an average boundary layer thickness (Kestin, 1957). Ha is the Hartmann number, representing the ratio of the driving electromagnetic force to the viscous force in the fluid.

With the introduction of Eq. 4.2.3, Eq. 4.2.1 is rewritten as

$\frac{d^2\alpha(t)}{dt^2} + 2\Delta_0\frac{d\alpha(t)}{dt} + (1 + \Delta_0^2)\alpha(t) = M(t)$ Eq. 4.2.4a)

$\frac{\partial\Omega(r,t)}{\partial t} = \frac{Ha^2}{2}(\omega_m - \Omega(r,t)) + \frac{\partial^2\Omega(r,t)}{\partial r^2} + \frac{3}{r}\frac{\partial\Omega(r,t)}{\partial r}$ Eq. 4.2.4b)

$M(t) = -4\frac{I}{R}\frac{\partial\Omega(r=R,t)}{\partial r}$ Eq. 4.2.4c)

while Eq. 4.2.2 changes to

$\alpha(t = 0) = \alpha_0$ Eq. 4.2.5a)

$\Omega(r, t = 0) = 0$ Eq. 4.2.5b)

$\Omega(r = R, t) = \frac{d\alpha(t)}{dt}.$ Eq. 4.2.5c)

The PDEs in Eq. 4.2.4 are coupled. Seeking their solution benefits from the use Laplace transform. Eq. 4.2.4 subject to Eq. 4.2.5 has Laplace transform with complex argument s,

$(2\Delta_0 + s)[s\alpha_L(s) - \alpha_0] + (1 + \Delta_0^2)\alpha_L(s) = M_L(s)$
Eq. 4.2.6a)

$s\Omega_L(r,s) = \frac{Ha^2}{2}\left[\frac{\omega_m}{s} - \Omega_L(r,s)\right] + \frac{\partial^2\Omega_L(r,s)}{\partial r^2} + \frac{3}{r}\frac{\partial\Omega_L(r,s)}{\partial r}$ Eq. 4.2.6b)

$M_L(s) = -4\frac{I}{R}\frac{\partial\Omega_L(r=R,s)}{\partial r}$ Eq. 4.2.6c)

with the boundary condition:

$\Omega_L(r = R, s) = R(s\alpha_L(s) - \alpha_0)$ Eq. 4.2.7

The subscript L represents the notation for the Laplace transform of functions.

Eq. 4.2.6b) subjected to Eq. 4.2.7 is solved, yielding

$$\Omega_L(r,s) = \left[s\alpha_L(s) - \alpha_0 - \frac{Ha^2\omega_m}{s(2s+Ha^2)}\right]\frac{R}{r}\frac{I_1\left(r\sqrt{s+\frac{Ha^2}{2}}\right)}{I_1\left(R\sqrt{s+\frac{Ha^2}{2}}\right)} + \frac{Ha^2\omega_m}{s(2s+Ha^2)} \qquad \text{Eq. 4.2.8}$$

where I_1 and I_2 are first and second order, modified Bessel functions of the first kind, respectively.

Substituting Eq. 4.2.8 into Eq. 4.2.6c), we obtain

$$M_L(s) = -D(s)\left[\alpha_L(s) - \frac{\alpha_0}{s} - \frac{Ha^2\omega_m}{s^2(2s+Ha^2)}\right] \qquad \text{Eq. 4.2.9}$$

where,

$$D(s) = \frac{4Is\sqrt{s+\frac{Ha^2}{2}}}{R}\frac{I_2\left(R\sqrt{s+\frac{Ha^2}{2}}\right)}{I_1\left(R\sqrt{s+\frac{Ha^2}{2}}\right)} \qquad \text{Eq. 4.2.10}$$

Substituting Eq. 4.2.9 into Eq. 6a) yields the angular displacement in Laplace transform,

$$\alpha_L(s) = \frac{Ha^2\omega_m D(s)}{s^2(2s+Ha^2)[1+(s+\Delta_0)^2+D(s)]} + \frac{\alpha_0[s^2+2s\Delta_0+D(s)]}{s[1+(s+\Delta_0)^2+D(s)]} \qquad \text{Eq. 4.2.11}$$

The first term of the RHS reflects the influence of the RMF on the motion of the cup. The second term contributes to the initial angle deflection which is only required for OCVs. Thus, setting $Ha = 0$ in Eq. 4.2.11 to get rid of the influence of RMFs, leads to the angular displacement for the OCVs,

$$\alpha_L(s) = \frac{[s^2+2s\Delta_0+D(s)]}{s[1+(s+\Delta_0)^2+D(s)]}\alpha_0, \qquad \text{Eq. 4.2.12}$$

which is in accordance with the previous OCV models. If setting $\alpha_0 = 0$ instead, the transient angular displacement for the EMVs is obtained,

$$\alpha_L(s) = \frac{Ha^2\omega_m D(s)}{s^2(2s+Ha^2)[1+(s+\Delta_0)^2+D(s)]}. \qquad \text{Eq. 4.2.13}$$

4.2.1.2. Features of characteristic equations

The inverse Laplace transforms of Eq. 4.2.13 is needed to model the actual angular displacement of the EMVs. The features of the transform equation are first examined before taking the inverse transform. Applying the orthogonality of Bessel functions to Eq. 4.2.10 yields,

$$D(s) = \frac{4Is(2s+Ha^2)}{R^2}\sum_{i=1}^{\infty}\left[s + \frac{Ha^2}{2} + \left(\frac{\mu_i}{R}\right)^2\right]^{-1}$$ Eq. 4.2.14

where the value of μ_i is given by $J_1(\mu_i) = 0$, while J_1 is the first order Bessel function of the first kind. After substituting Eq. 4.2.14 to Eq. 4.2.13, it has been easily seen that $\alpha_L(s)$ is a single-valued function which has a simple pole at $s = 0$ and the remaining poles occurring where

$$1 + (s + \Delta_0)^2 + D(s) = 0$$ Eq. 4.2.15

In contrast, $-Ha^2/2$ is only a removable singularity of Eq. 4.2.13, but not its pole. The roots of Eq. 4.2.15 can be divided into two groups. One group consists of infinitely many real poles, denoted by s_k with $k = 1,2,3 \ldots.$ and the other group includes two conjugate complexes, denoted by s_+ and s_-.

We first investigate the real-root group. Substituting Eq. 4.2.14 into Eq. 4.2.15 yields,

$$-\frac{1+(s+\Delta_0)^2}{s\left(s+\frac{Ha^2}{2}\right)} = \frac{8I}{R^2}\sum_{i=1}^{\infty}\left[s + \frac{Ha^2}{2} + \left(\frac{\mu_i}{R}\right)^2\right]^{-1}$$ Eq. 4.2.16

Both sides of the equation above are plotted in Fig. 4.2.2.2 by setting each as a function of s.

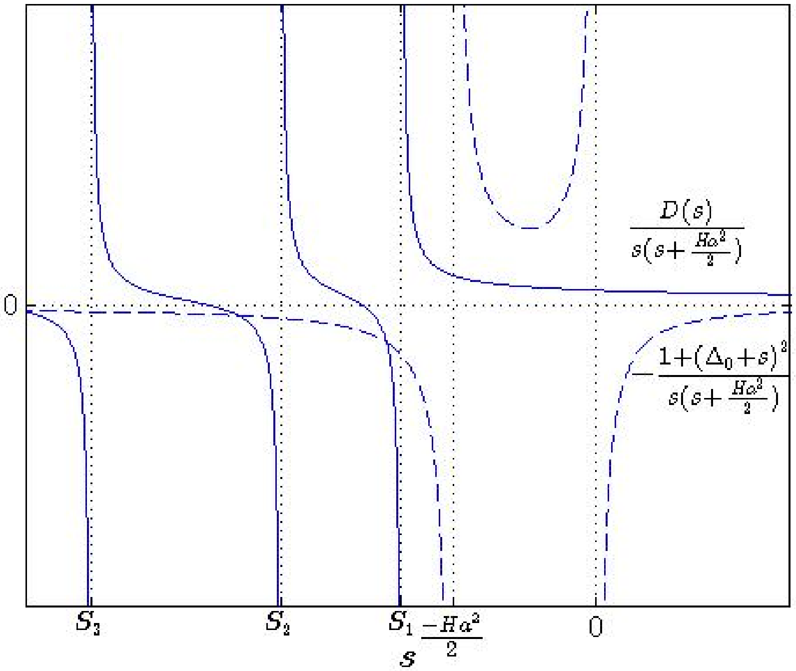

Fig. 4.2.2.2. Graphic scheme for locating negative real roots

Fig. 4.2.2.2 is not drawn to scale but only to illustrate the location of real roots. The shape of the curves and the positions of their intersecting points s_k are very similar to those plotted by Kestin and Newell (1957) for locating the real roots of OCVs. The slight difference between them will be completely removed if setting $Ha = 0$ in Fig. 4.2.2.2. Some facts that we can tell from the figure include a) In the positive range, there is no intersections, suggesting that all real roots must be negative only, b) In the range between $-Ha^2/2$ and 0, the RHS curve is always higher than the LHS one. It is shown from the analysis of Eq. 4.2.14 and 4.2.16 that this feature is always true only if $Ha^2 I < 16$. This is a loose condition as both Ha and I are generally less than unity. c) In the range of less than $-Ha^2/2$, there is one and only one intersection between every pair of consecutive $S_k = -\left[\frac{Ha^2}{2} + \left(\frac{\mu_k}{R}\right)^2\right]$. In any interval between S_k and S_{k+1}, the RHS curve decreases monotonically from positive infinity to negative infinity. It is guaranteed to have only one intersection s_k with the monotonic LHS curve. All s_k are slightly less than S_k, and the difference is mainly dependent on the value of I/R^2. As I/R^2 increases, s_k move continuously to the left and away from S_k, but never jump over to next interval. Provided that the tests are performed with the same suspension system, the real roots for the EMVs are larger by about $Ha^2/2$ in magnitude than those for OCVs.

Based on the above features of real roots, an approximate solution is derived. It is impossible to obtain an explicit expression of the roots from the transcendental equation Eq. 4.2.15 or 4.2.16, although the intervals in which the roots are confined are easily located. With the knowledge of intervals, there are a few numerical methods that can be used to find approximate solutions of the intersections. When fitting experimental data to determine the parameters of interest, the preset condition may vary hundreds of times, and at least twenty roots are solved for each change. The numerical iteration solving for these roots takes most of the computation time. In order to achieve fast processing speed, an approximate analytic solution is then developed on the basis of truncating the Taylor series. This solution also facilitates future error analysis of the EMV experiments. We first set

$$s_k = -\left[\frac{Ha^2}{2} + \left(\frac{\mu_k + \varepsilon_k}{R}\right)^2\right] \qquad \text{Eq. 4.2.17}$$

where $\varepsilon_k = O(1)$, accounting for the difference between s_k and S_k. Combining Eq. 4.2.10, 4.2.15 and 4.2.17 yields,

$$\left[1 + \left[\varDelta_0 - \left(\frac{\mu_k + \varepsilon_k}{R}\right)^2 - \frac{Ha^2}{2}\right]^2\right] J_1(\mu_k + \varepsilon_k) - \frac{4I}{R^2}(\mu_k + \varepsilon_k)\left[\left(\frac{\mu_k + \varepsilon_k}{R}\right)^2 + \frac{Ha^2}{2}\right] J_2(\mu_k + \varepsilon_k) = 0$$

Eq. 4.2.18

in which J_2 is the second order Bessel function of the first kind. Their Taylor series expansion at μ_k is given by

$$J_1(\mu_k+\varepsilon_k)=J_0(\mu_k)\varepsilon_k+O(\varepsilon_k^2)$$ Eq. 4.2.19a)

$$J_2(\mu_k+\varepsilon_k)=-J_0(\mu_k)[1-2\varepsilon_k/\mu_k+O(\varepsilon_k^2)]$$ Eq. 4.2.19b)

in which J_0 is the zeroth order Bessel function of the first kind.

Substituting Eq. 4.2.19a) and b) into Eq. 4.2.18 yields,

$$\frac{-4I\mu_k}{R^2}\left[\left(\frac{\mu_k}{R}\right)^2+\frac{Ha^2}{2}\right]+\left[1+\left(\Delta_0-\frac{Ha^2}{2}\right)^2+\left(\frac{\mu_k}{R}\right)^2\left[\left(\frac{\mu_k}{R}\right)^2-2\Delta_0+Ha^2\right]+\frac{4I}{R^2}\left[\left(\frac{\mu_k}{R}\right)^2-\frac{Ha^2}{2}\right]\right]\varepsilon_k+O(\varepsilon_k^2)=0$$ Eq. 4.2.20

Assuming $\Delta_0, Ha^2 \sim O(1)$, and getting rid of all high order truncation error in Eq. 4.2.20, an explicit solution of ε_k is given by

$$\varepsilon_k=\frac{\left[\left(\frac{\mu_k}{R}\right)^2+\frac{Ha^2}{2}\right]}{\left(\frac{\mu_k}{R}\right)^4+\frac{4I}{R^2}\left(\frac{\mu_k}{R}\right)^2+1}\frac{4I\mu_k}{R^2}.$$ Eq. 4.2.21

Substituting Eq. 4.2.21 into Eq. 4.2.17 gives rise to the approximate solution of real roots,

$$s_k=-\frac{Ha^2}{2}+\left(\frac{\mu_k}{R}\right)^2\left[1+\frac{\left(\frac{\mu_k}{R}\right)^2+\frac{Ha^2}{2}}{\left(\frac{\mu_k}{R}\right)^4+\frac{4I}{R^2}\left(\frac{\mu_k}{R}\right)^2+1}\frac{4I}{R^2}\right]^2.$$ Eq. 4.2.22

The values given by Eq. 4.2.22 have errors of less than 0.1% when both $R>1$ and $I<0.015R^2$ are satisfied.

Besides real roots, Eq. 4.2.15 has a pair of complex roots. Their residues correspond to a damped harmonic motion as we will discuss later. Hence, the complex roots are denoted by

$$s_\pm=(-\Delta\pm i)\omega$$ Eq. 4.2.23

where Δ is the logarithmic decrement of the damping oscillation, and ω is the dimensionless oscillation frequency, defined by $\omega=\overline{\omega}/\overline{\omega}_0$.

Substituting Eq. 4.2.23 into Eq. 4.2.15 yields

$$1+(\Delta_0-\Delta\omega)^2-\omega^2+\mathrm{Re}D[(-\Delta\pm i)\omega]=0$$ Eq. 4.2.24a)

$$\pm2\omega(\Delta_0-\Delta\omega)+\mathrm{Im}D[(-\Delta\pm i)\omega]=0$$ Eq. 4.2.24b)

from which Δ and ω are determined. The complex roots for the EMVs are different from those for the OCVs even if the same amount of fluid is tested with the same suspension system. All the difference is modeled by the presence of $Ha^2/2$ in $D(s)$.

4.2.1.3. Transient Angular Displacement

The inverse Laplace transform of Eq. 4.2.13 gives rise to the actual motion of the cup,

$$\alpha(t) = \frac{1}{2\pi i} \int_C \frac{Ha^2 \omega_m D(s) e^{st}}{s^2(2s+Ha^2)[1+(s+\Delta_0)^2+D(s)]} ds \qquad \text{Eq. 4.2.25}$$

where C is any vertical contour in the right side of the complex s-plane so that all points along the contour are guaranteed to be greater than the real part of all poles. Because all poles of the integrand are the simple ones, their residues can be summarized to evaluate the contour integral, yielding

$$\alpha(t) = \alpha_\infty + \alpha_T(t) + \alpha_M(t) \qquad \text{Eq. 4.2.26}$$

where

$$\alpha_\infty = \mathrm{Res}(s=0) = \frac{2\sqrt{2} I \omega_m Ha}{(1+\Delta_0^2)R} \frac{I_2(\frac{RHa}{\sqrt{2}})}{I_1(\frac{RHa}{\sqrt{2}})}, \qquad \text{Eq. 4.2.27a)}$$

$$\alpha_D(t) = \sum \mathrm{Res}(s = s_\pm) = \sum_{s=s_\pm} \frac{Ha^2 \omega_m D(s)}{s(2s+Ha^2)[2(s+\Delta_0)+D'(s)]} e^{st}, \qquad \text{Eq. 4.2.27b)}$$

$$\alpha_T(t) = \sum_{k=1}^{\infty} \mathrm{Res}(s = s_k) = \sum_{k=1}^{\infty} \frac{Ha^2 \omega_m D(s_k)}{s_k(2s_k+Ha^2)[2(s_k+\Delta_0)+D'(s_k)]} e^{s_k t}. \qquad \text{Eq. 4.2.27c)}$$

The actual angular displacement is regarded as a combination of three components of motion, each corresponding to a group of poles. α_∞ is equal to the residue of $s = 0$. It represents the angular displacement of the cup in final equilibrium state when the cup ceases oscillating and retrieves stationary. Instead of being stationary like the cup, the fluid reaches its steady flow state to maintain a constant viscous torque on the cup. The viscous torque is well balanced by the torsional torque due to the twisting of the suspension string with a twist angle of α_∞. α_D is obtained from the residues of complex roots $s_\pm$. It describes a classic damped oscillation of the cup around the initial position. α_T consists of an infinite series of exponential decay terms, each of them corresponding to the residue of a single real root s_k. The magnitude of s_k evaluates the rate at which the kth exponential term decays. The overall motion that α_T describes is nearly close to an exponential decay so that we call it fast decay.

Numerical calculations of Eq. 4.2.27c) can be performed by retaining a number of terms of the series in sequence. Once sufficient terms are taken, the truncation errors can be successfully avoided for two reasons. First, the starting value of each exponential term is in monotonic decreasing sequence. Second, the latter exponential term has faster decay rate as $|s_k| < |s_{k+1}|$. Therefore, the first exponential decay is the strongest one at any time, and the former decay is stronger than the subsequent ones.

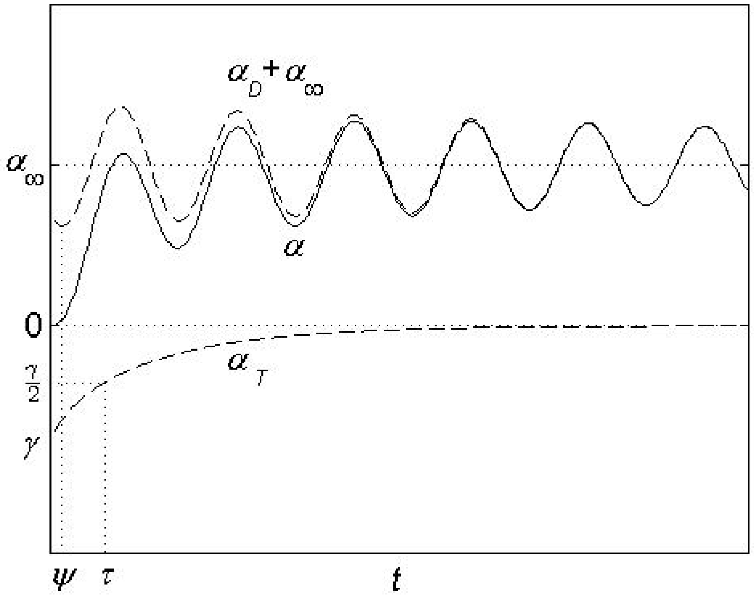

Fig. 4.2.3 Transient angular displacement of typical EMVs

Fig. 4.2.3 shows the transient motion of the cup in a typical EMV, as well as all of its components. $\alpha(t)$, plotted as a solid curve, looks like a damped oscillation with shifting equilibrium points around which the oscillation occurs. The curve is less waved with time and finally becomes a straight line, which is not shown in the figure. Accompanying with the oscillation, the cup consistently twists toward its final equilibrium position. Thus, it is reasonable to decompose the overall transients as two distinct motions. One is the harmonic oscillation damping around the final equilibrium point, denoted by the dashed line of $\alpha_\infty + \alpha_D$ in Fig. 4.2.3, and the other is fast decay α_T.

The EMV might be a more powerful technique comparing with the OCV because it is able to provide more information. Similar to the derivation of Eq. 4.2.26, the inverse Laplace transform of Eq. 4.2.12 gives rise to the angular displacement for an OCV,

$$\alpha(t) = \alpha_0 \sum_s \frac{1+\Delta_0^2}{s[2(s+\Delta_0)+D'(s)]} e^{st}, \qquad \text{Eq. 4.2.28}$$

in which s are the roots of the characteristic equation Eq. 15. They are slightly different from those for the EMVs in that $s = 0$ is no longer a pole, and that $Ha = 0$ in the solution for $s_\pm$ and s_k. A typical transient motion of the cup in an OCV is nearly a damped oscillation as plotted in Fig. 4.2.4. The motion of the cup in an OCV is different from that in an EMV in two aspects. First, fast decay is generally too small to provide any reliable information for measurements. It is deliberately filtered out by ignoring the first few cycles of the oscillation in an OCV measurement. Second, the cup returns its initial position by the end of the oscillation because there is lack of a external restoring force to maintain an angular displacement of the cup. Therefore, besides the damped oscillation, the final equilibrium position and fast decay can be observed in an EMV measurement. Their existence makes it possible that more physical properties may be determined in better accuracy and with faster response time.

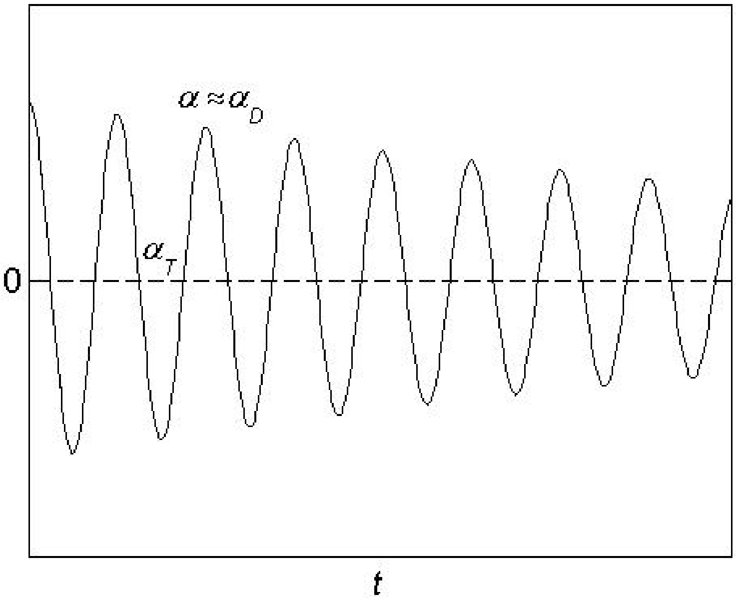

Fig. 4.2.4 Transient angular displacement of typical OCVs

The solutions given by Eqs. 2.27b) and 2.27c) are expressed in terms of a series, which are cumbersome for further analysis. Then, the damped oscillation is rewritten in a common way as

$$\alpha_D(t) = Ae^{-\Delta\omega t}\cos(\omega t + \phi). \qquad \text{Eq. 4.2.29}$$

where A is the amplitude of the oscillation at the initial state and ϕ is the phase angle. The values of A and ϕ are obtained from Eq. 4.2.27b). The phase shift, ψ, defined as

$$\psi = \frac{\pi-\phi}{\omega}, \qquad \text{Eq. 4.2.30}$$

is illustrated in Fig. 4.2.3. It is equivalent to the dimensionless time when the oscillation is at the lowest point.

Meanwhile, fast decay is characterized by its amplitude at the initial moment, γ,

$$\gamma = \alpha_T(0), \qquad \text{Eq. 4.2.31}$$

and half-lift τ, the amount of time required for the decay to fall to $\gamma/2$, such as

$\alpha_T(\tau) = \frac{\gamma}{2}$. Eq. 4.2.32

γ and τ represent the strength and the decay rate of fast decay, respectively. Their values are determined by Eq. 4.2.27c), and their physical meanings are illustrated in Fig. 4.2.3.

It should be noticed that A, ϕ, γ, and α_∞ are correlated to match the initial condition $\alpha(0) = 0$, yielding

$A\cos(\phi) + \gamma + \alpha_\infty = 0$ Eq. 4.2.33

Therefore, any three of A, ϕ, γ, and α_∞ are independent. They are able to exclusively identify the transient angular displacement along with the other three parameters $\varDelta$, ω, and τ.

4.2.2. Understanding of Mechanism

One purpose of this study is to understand the mechanism of EMVs so that some design principles can be put forward. The motion of the cup has been successfully identified by a set of variables. Next, their dependence on design parameters though which the experimental conditions are preset, including $\varDelta_0$, ω_m, I, R and Ha, is discussed on purpose of guiding further experimental design.

Among the design parameters, $\varDelta_0$ has the least significant influence on the angular displacement. $\varDelta_0$ is usually much smaller than unity so that at least a few oscillation can be observed before the oscillation becomes too small to measure. The change of $\varDelta_0$ is limited in a small range, and then has no considerable influence on the motion of the cup except the damping ratio, $\varDelta$. However, $\varDelta - \varDelta_0$ is insensitive to the change of $\varDelta_0$. Because the useful information for measurements is $\varDelta - \varDelta_0$ other than $\varDelta$, the only impact of $\varDelta_0$ on the motion becomes less important. Therefore, the impact of $\varDelta_0$ is not discussed later.

ω_m has a simple but powerful impact on the motion of the cup in an EMV. It varies linearly with the amplitude of all components of the motion according to Eq. 4.2.27. Other parameters relating to time, such as phase shift, decay rate and period are independent of ω_m. The independence is shown by the characteristic equation Eq. 4.2.15 in which ω_m is absent, not a variable in the solutions of all kinds of poles. Hence, altering ω_m is a convenient and efficient method for setting the angular displacement in a moderate range with no need of concerning about any other undesirable changes.

I, R and Ha are the remaining design parameters, which are mainly focused in later discussion. The range of R and Ha, as well as the exact value of I, can be preset by altering the cup geometry, the amount of tested fluid, the suspension wire, the strength of the magnetic field, and so on. They have significant influence on the motion of the cup. At the same time, R and Ha are the target parameters that need to be determined from measurements, as they are actually functions of viscosity and electrical conductance of fluid. It makes them play a more important role to measurements.

The solution given by Eqs. 4.2.26 and 4.2.27 is then programmed to determine the value of all the seven variables under conditions of $\omega_m = 958.3$, $\Delta_0 = 0.005$, $I = 0.01, 0.05$ and 0.1, $R \leq 50$, and $Ha \leq 1$. The values of ω_m is in accordance with the previous experimental study (Li, 2004). The dependence of these variables on R and Ha are plotted in Fig. 4.2.5-4.2.11, respectively, for a variety of I.

4.2.3. Fast Decay

Fast decay arises mainly from the rotational flow induced by the Lorentz force. The motion of the fluid contributes to a pair of interacting physics, each of them giving rise to a component of the flow. First, the oscillation of the wall is able to penetrate a certain distance of layer in the fluid. Such an oscillation mainly affects the behavior of the damped oscillation as we will discuss later. Second, the Lorentz force drives the fluid to form a rotational flow with the assumption that the cup is not in motion. The rotational flow can be modeled by Eq. 4.2.3c) subject to $\Omega(R,t) = \Omega(r,0) = 0$, whose solution consists of an infinite series of exponent decay terms each of which has time constant $1/S_k$ with $S_k = -\left[\frac{Ha^2}{2} + \left(\frac{\mu_k}{R}\right)^2\right]$. The growth of the rotational flow is a process in which magnetic energy continually stores in the flow after overcoming the dissipation effects. The presence of the oscillation requires extra energy, which means it takes longer for the flow to grow. It explains why $|s_k| > |S_k|$. Because the gap between s_k and S_k is small, fast decay is likely to vary with the rotational flow almost at the same rate. Therefore, the features of fast decay are discussed on the basis of the understanding of the rotational flow.

The transients of the rotational flow can be classified according to the value of $\frac{Ha^2R^2}{2}$, which represents the ratio of the electromagnetic force to the viscous force. Because the only variable to adjust $\frac{Ha^2R^2}{2}$ is the strength of the external magnetic field, B, for a specific fluid tested in a certain cup, $\frac{Ha^2R^2}{2}$ acts as the index of B.

In a strong magnetic field with $\frac{Ha^2R^2}{2} \gg 1$, there is a thin boundary layer comparing to the radius of the cup. A steep velocity gradient grows up in the boundary layer, creating a strong viscous force in balance with the Lorentz force. In the remaining space, the flow uniformly accelerates to the rotational rate of the magnetic field, while the Lorentz force dramatically decreases and finally disappears. Thus, the Lorentz force is the dominant mechanism of the flow growth, having the same time scale of $\frac{2}{Ha^2}$ according to Eq. 4.2.4b). It also agrees with the analysis of S_k, which approaches to $-\frac{Ha^2}{2}$ as $\frac{Ha^2}{2} \gg \frac{1}{R^2}$. The relation of $\tau \sim \frac{1}{Ha^2}$ is in accordance with the reciprocal curve of $R = 20$ in Fig. 4.2.5b). It is noteworthy to point out that τ is independent on

R. The independence is well illustrated by the curve of $Ha = 0.5$ in Fig. 4.2.5a), which is flat in the range of $R > 20$.

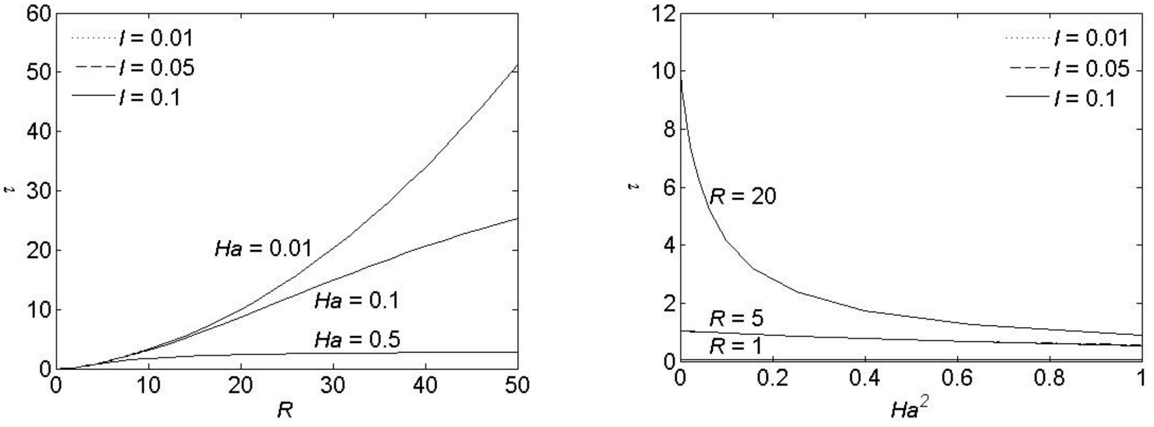

a) τ vs. R

b) τ vs. Ha^2

Fig. 4.2.5 Decay Rate of Fast Decay

When $\frac{Ha^2R^2}{2} \ll 1$, the external magnetic field is too weak to induce a strong flow. The flow remains slow comparing with the rotation of the magnetic field, and the corresponding Lorentz force is almost unvaried throughout the transients. Although the velocity gradient only slightly grows, the viscous force remarkably rises up because of the relative large viscosity, and finally balances with the Lorentz force at steady state. Hence, the viscous term is dominant in Eq. 4.2.4b) and its time scale of R^2 is also the time scale of the flow. All the curves in Fig. 4.2.5a) have nearly parabolic shape for small R such as $\frac{Ha^2R^2}{2} \ll 1$, in accordance with the above analysis.

In the medium magnetic field with $\frac{Ha^2R^2}{2} \sim 1$, the development of the viscous force and the Lorentz force are at the same level and the time scale of the flow is dependent on both R and Ha. The increase of R or the decrease of viscosity requires more time to develop a steeper velocity gradient, as shown in Fig. 4.2.5a). The magnetic field with larger Ha gets stronger to create a larger Lorentz force, which shorten the time that the flow needs to grow, as shown in Fig. 4.2.5b).

The amplitude of fast decay, γ, is impacted not only by the rotational flow, but also by the boundary layer through which the rotational flow is able to oscillate the cup. As either $R \rightarrow 0$ or $Ha \rightarrow 0$, corresponding to the extremely large viscosity of fluids or the absence of the RMF respectively, there is no rotational flow so that $\gamma \rightarrow 0$. As $R \rightarrow \infty$, the rotational flow is regarded as the potential flow which fails to rotate the cup due to the insignificant fluid viscosity. As $Ha \rightarrow \infty$, the applied RMF is so strong as to complete the establishment of steady rotational flow before creating a significant fast decay. Therefore, the magnitude of γ has a hump-shaped dependence on either R or Ha, which is shown by some curves in Fig. 4.2.6. The other monotonic curves will present a hump as well after expanding the range of R or Ha. The dependence of γ is further revealed through the analysis of Eq. 4.2.27c). In a weak magnetic field of $\frac{Ha^2R^2}{2} \ll 1$, $\gamma \sim Ha^2$ and $\gamma \sim R^{4\rightarrow 0}$ where the index is 4 for $R \ll 1$ and 0 for $R \gg 1$. In a strong magnetic field of $\frac{Ha^2R^2}{2} \gg 1$, $\gamma \sim R^{-2}$ and $\gamma \sim Ha^{0\rightarrow -4}$ where the index is 0 for $Ha \ll 1$ and -4 for $Ha \gg 1$.

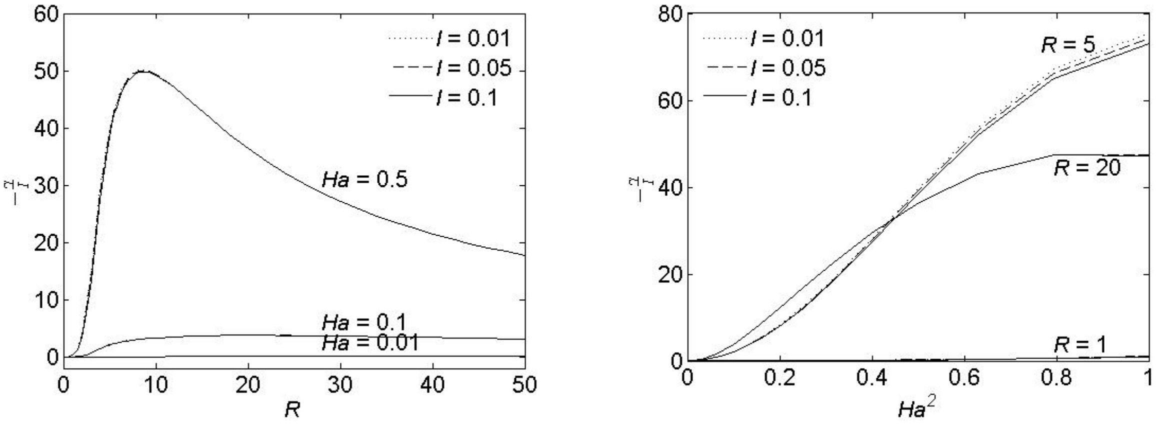

a) γ vs. R b) γ vs. Ha^2

Fig. 4.2.6 Amplitude of Fast Decay

4.2.4. Angular Displacement at Equilibrium

The value of α_∞ completely relies on the viscous torque at equilibrium state. When the new equilibrium is achieved, the steady state flow creates a constant viscous torque on the static cup. The cup deviates away from its initial position by α_∞, and a torsional torque is formed to balance the viscous torque. Any change of the viscous torque leads to a different value of α_∞.

Both R and Ha affect the viscous torque. The stronger magnetic field with larger Ha induces faster rotational flow, resulting to stronger viscous torque. Fig. 4.2.7b) shows α_∞ dramatically increases with the increase of Ha. For less viscous fluid with larger R, the viscous torque or α_∞ tends to decrease as shown in Fig. 4.2.7a), in spite of the slight increase of angular velocity gradient.

The Dependence of Ha and R can be further revealed through the analysis of Eq. 4.2.27a). In a weak magnetic field, $\frac{Ha^2R^2}{2} \ll 1$ such that $\frac{I_2(\frac{RHa}{\sqrt{2}})}{I_1(\frac{RHa}{\sqrt{2}})} \approx \frac{RHa}{4\sqrt{2}}$, and $\alpha_\infty \approx \frac{I\omega_m Ha^2}{2(1+\Delta_0^2)}$. Thus, α_∞ is in proportional to R^0 and Ha^2, agreeing with the flat curve of $Ha = 0.01$ in Fig. 4.2.7a), and the straight line of $R = 1$ in Fig. 4.2.7b). Under conditions of strong magnetic field, $\frac{Ha^2R^2}{2} \gg 1$ such that $\frac{I_2(\frac{RHa}{\sqrt{2}})}{I_1(\frac{RHa}{\sqrt{2}})} \approx 1$, and $\alpha_\infty \approx \frac{2\sqrt{2}I\omega_m Ha}{(1+\Delta_0^2)R}$.

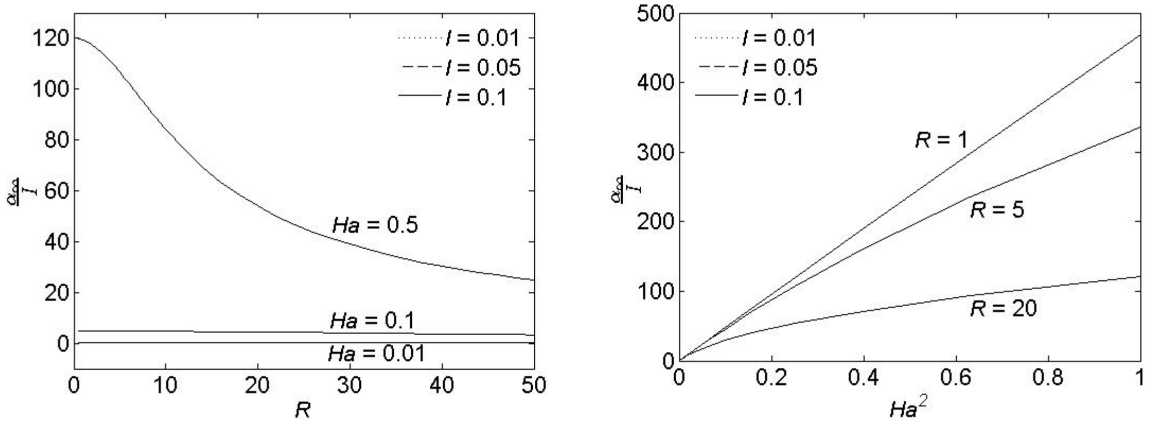

a) α_∞ vs. R b) α_∞ vs. Ha^2

Fig. 4.2.7 Angular Displacement at Equilibrium

4.2.5. Oscillation

The damped oscillation of the cup contributes to the interaction of the viscous torque and the torsional torque. For a specific suspension system, the oscillation is governed by the viscous torque, which is related to the magnitude of the Lorentz force and the structure of the boundary layer. Ha^2 is in proportional to the Lorentz force, while the change of Ha has no impact on the structure of boundary layer. In the comparison, R affects the structure of the boundary other than the Lorentz force. In a small cup with small R, the fluid moves with the cup as a rigid body, and the oscillation occurs everywhere in the fluid. A large cup is the one with large R, in which the oscillation is confined only in a small layer of fluid near the cup wall while there is a rotational flow in the center.

The strength of the oscillation is evaluated by A, its amplitude at the initial moment when the rotational flow has not started yet. Fig. 4.2.8b shows a linear dependence of Ha^2, which is explained by the linear relationship between the Lorentz force and Ha^2. Fig. 4.2.8a) shows a relation of $A \sim R^{-1}$ for large cups. It is because the increase of R or the decrease of viscosity gives rise to a thinner boundary layer, leading to a smaller viscous torque. In a small cup where the boundary layer extends to the center of the cup, the change of viscosity has little or no influence on the structure of the boundary layer, implying $A \sim R^{\sim 0}$.

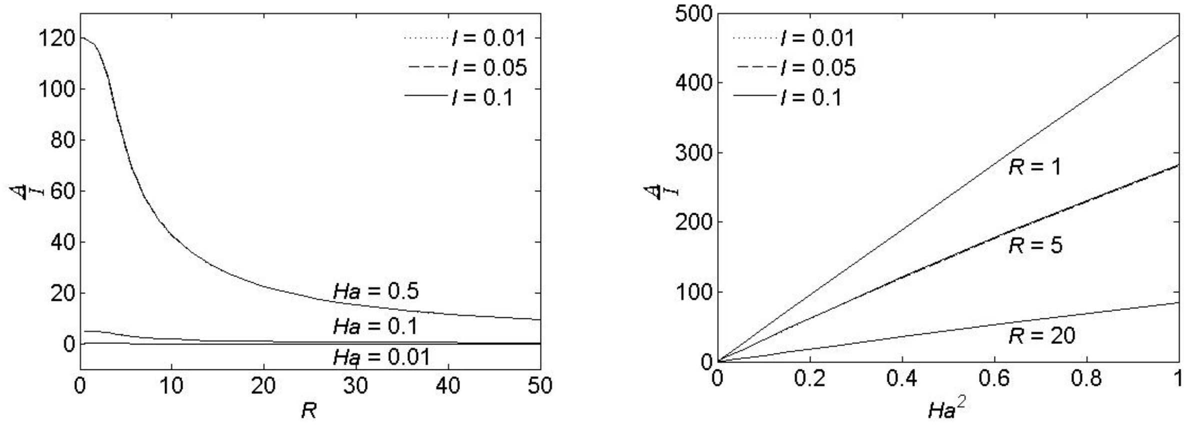

a) A vs. R b) A vs. Ha^2

Fig. 4.2.8 Amplitude of the Damped Oscillation

The damping ratio of the oscillation Δ is always larger than Δ_0 because the viscous effects act as an additional drag to the damping. Similar to A, $\Delta - \Delta_0$ is linearly dependent on Ha^2as shown in Fig. 4.2.9b). It is because the Lorentz force not only creates the oscillation, but also acts as an additional drag force to enhance the damping effects. Fig. 4.2.9a) shows that $\Delta - \Delta_0$ has minimum values at $R \rightarrow 0$ and at $R \rightarrow \infty$. A peak value occurs around $R \approx 5$. The dependence is much stronger in small cups than in large cups.

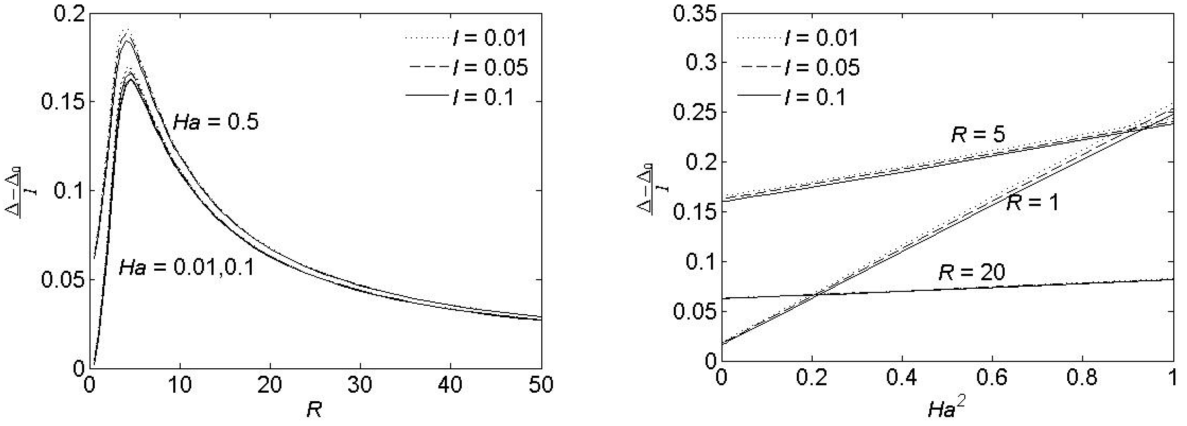

a) $\Delta - \Delta_0$ vs. R b) $\Delta - \Delta_0$ vs. Ha^2

Fig. 4.2.9 Damping Ratio of the Damped Oscillation

Both R and Ha have insignificant influence on the oscillation frequency ω. Fig. 4.2.10a) shows that filling fluid in the cup makes a difference of ω by no more than 5% for a wide variety of R. And the difference caused by the change of Ha is even smaller, such as less than 1%, as shown in Fig. 4.2.10b). Thus, the observation of the oscillation frequency is less important.

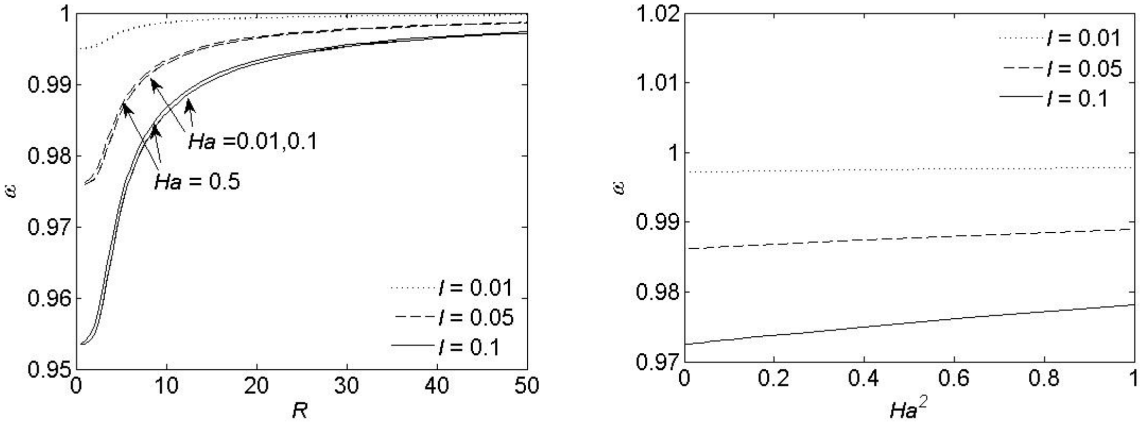

a) ω vs. R

b) ω vs. Ha at $R = 5$

Fig. 4.2.10 Frequency of the Damped Oscillation

The phase-shift of the oscillation mainly reflects the comparison of fast decay with the damped oscillation in strength. Combining Eq. 4.2.30 and Eq. 4.2.33 yields,

$$\cos(\omega\psi) = \frac{1+\gamma/\alpha_\infty}{A/\alpha_\infty} \qquad \text{Eq. 4.2.34}$$

Because ω is almost of unity, the equation gives $\gamma = 0$ as $\psi = 0$, suggesting the absence of fast decay. Larger ψ corresponds to a relative stronger fast decay. Fig. 4.2.11b) shows a linear dependence of Ha^2 like all other parameters describing the oscillation. Fig. 4.2.11a) shows ψ rapidly rises up with the increase of R for small cups, and the rise becomes slow for large cups. The phase-shift is an important parameter for EMV measurements. A large ψ benefits the measurements in which the features of fast decay are mainly concerned. If only the features of the oscillation are used instead, a small ψ is better for getting rid of the influence of fast decay.

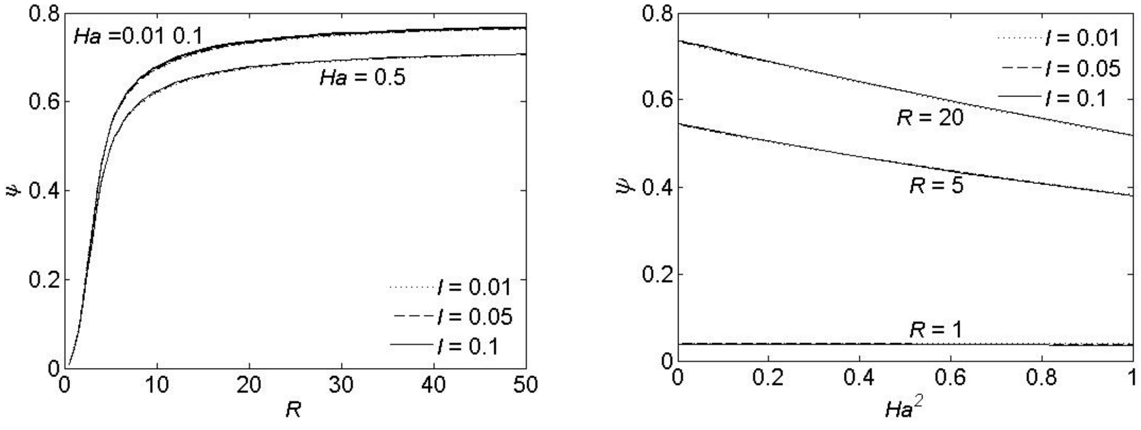

a) ψ vs. R

b) ψ vs. Ha^2

Fig. 4.2.11 Phase shift of the Damped Oscillation

Figs. 2.5-2.11 also show the influence of I on the motion of the cup. The value of I can be easily adjusted in a small range by changing the amount of fluid for a specific suspension system. It is shown from Figs 2.6, 2.7 and 2.8 that the parameters relating to the strength of the motion, such as A, γ, and α_∞, vary nearly linearly with I, because all the curves, plotted as the ratio of them to I, are almost or completely overlapped for a variety of I. $\varDelta - \varDelta_0$ is at the same situation, which almost linear to I as shown in Fig. 4.2.9. In contrast, τ and ψ are slightly dependent or independent on I as the curves for different I are overlapped in Figs. 2.5, and 2.11. Finally, Fig. 4.2.10 shows that the change of ω is nonlinearly dependent on I, and a relative strong dependence occurs at small R. Thus, adjusting I is able to preset $\varDelta - \varDelta_0$ and ω, besides the ability of preset the range of the angular displacement like adjusting ω_m. In general, larger I causes a stronger response of the cup, leading to a higher measurement accuracy.

4.2.6. Practical Implication

The ultimate purpose of this project is to infer the value of viscosity and electrical conductance from the observed motion of the cup. There are two practical methods of EMV measurements, the rapid method and the quasi-steady-state (QSS) method.

The rapid measurement takes advantage of the features of both fast decay and the oscillation. It is called rapid measurement because only the first few cycles are need for data fitting. Some design principles that facilitate the rapid measurement include: a**)** Large R is needed to obtain a sufficiently strong fast decay**.** The phase-shift of the oscillation, ψ, is relative large in large cups, meaning fast decay becomes competitive to the oscillation in magnitude. b) Small Ha is preferred to achieve a high measurement accuracy of R or $\bar{\nu}$. Among all parameters, the decay rate of fast decay, τ, has the strongest dependence on R as $\tau \sim R^2 \sim \bar{\nu}^{-1}$, and it occurs only in the weak magnetic field with $\frac{Ha^2 R^2}{2} \ll 1$. A magnetic field with smaller Ha creates a stronger fast decay as well. c) The determination of Ha or $\bar{\sigma}$ is relatively accurate in comparison with R, because of the fact that there are more parameters with stronger dependence on Ha. Under conditions of large R and small Ha, the amplitude of the damped oscillation, A, is the most sensitive parameter to Ha as $A \sim Ha^2 \sim \bar{\sigma}^1$. The response of other parameters to the change of R and Ha will improve the measurement accuracy. The rapid method has already been exploited in previous experimental studies (Li, 2004). In their experiments, $R = 9.5$, and $Ha = 0.037$.

In contrast, the QSS measurements collect information involved in the quasi-steady state only. After the first few cycles when fast decay completely vanishes, the motion of the cup becomes a pure oscillation around the final equilibrium point. Thus, the system reaches the so-called quasi-steady state. The parameters that can be obtained from the damped oscillation are α_∞, ω and $\varDelta - \varDelta_0$. They are substituted into Eqs. 24a), 24b) and 27a) to determine R and Ha. As ω is insensitive to the change of R and Ha, the measurement accuracy is totally dependent on the dependence of α_∞ and $\Delta - \Delta_0$. The application principles for the QSS measurement include: a) Large Ha is preferred to improve the measurement accuracy of viscosity. According to Fig. 4.2.7b), α_∞ becomes strongly dependent on the change of Ha when $Ha^2 > 0.2$ and $R > 5$, or when $Ha^2 > 0.4$ and $R > 1$. Thus, the determination of viscosity is not only related to the change of $\Delta - \Delta_0$, but also the change of α_∞. b) large I is needed to have $\Delta - \Delta_0$ as large as possible.

There are some additional principles we should pay attentions to, a) The range of the angular displacement can be adjusted by setting appropriate $\omega_m$and I. The motion of the cup should be moderate so that it can be detected. At the same time, it won't be too violent to break down the fragile torsional wire. b) Low frequency RMF with $\overline{\omega}_m < \frac{1}{\overline{R}^2\sigma\mu_0}$, where μ_0 is the permeability of free space, is required to have a Lorentz force linear with r. The relation sets up a maximum limit of ω_m.

4.3. Two Dimensional Model

A 2-D EMV model is established in this section. Our earlier 1D model assumes the contact of fluid to the bottom of the cup has negligible influence on the motion of the cup. The 1D model is applicable only for testing slim fluid column. Even if so, the omission of the bottom effects causes additional measurement error. Thus, we come up with a 2D model to take the bottom effects into account.

4.3.1. Analytical model

4.3.1.1. <u>Mathematic Description</u>

Dimensionless governing equations describing physical phenomena in a cylindrical cup EMV are listed below,

$$\frac{d^2\alpha(t)}{dt^2} + 2\Delta_0\frac{d\alpha(t)}{dt} + \left(1 + \Delta_0{}^2\right)\alpha(t) = M(t) \qquad \text{Eq. 4.3.1a)}$$

$$\frac{\partial\Omega(r,z,t)}{\partial t} = \frac{Ha^2}{2}\left(\omega_m - \Omega(r,z,t)\right) + \frac{\partial^2\Omega(r,z,t)}{\partial r^2} + \frac{3}{r}\frac{\partial\Omega(r,z,t)}{\partial r} + \frac{\partial^2\Omega(r,z,t)}{\partial z^2} \qquad \text{Eq. 4.3.1b)}$$

$$M(t) = \frac{4I}{RH}\left[\int_0^R \left(\frac{r}{R}\right)^3 \frac{\partial\Omega(r,z=0,t)}{\partial z}dr - \int_0^H \frac{\partial\Omega(r=R,z,t)}{\partial r}dz\right] \qquad \text{Eq. 4.3.1c)}$$

in which all parameters have been defined in Eq. 4.2.3, except $H = \frac{\overline{H}}{\delta}$, where $\overline{H}$ is the actual height of liquid column. Eq. 4.3.1a) is the governing equation for the motion of the cup driven by the viscous torque. Eq. 4.3.1b) governs the flow in the cup with the presence of the Lorentz force. Eq. 4.3.3c) describes the viscous torque exerted on the side and bottom walls.

The fluid flow is subjected to boundary conditions,

$$\Omega(r, z = 0, t) = \frac{d\alpha(t)}{dt}$$ Eq. 4.3.2a)

$$\frac{\partial}{\partial z}\Omega(r, z = H, t) = 0$$ Eq. 4.3.2b)

$$\Omega(r = R, z, t) = \frac{d\alpha(t)}{dt}$$ Eq. 4.3.2c)

At the side and bottom walls, the no-slip condition is used. The drag at the top surface of the fluid is ignored. The fluids and the suspension system are at rest before the RMF turns on, so that the initial conditions are given by

$$\Omega(r, z, t = 0) = 0$$ Eq. 4.3.3a)

$$\alpha(t = 0) = 0$$ Eq. 4.3.3b)

Laplace Transform of the governing equations Eq. 4.3.1 with initial conditions Eq. 4.3.3 is written as

$$[1 + (s + \Delta_0)^2]\alpha_L(s) = M_L(s)$$ Eq. 4.3.3a)

$$s\Omega_L(r, z, s) = \frac{Ha^2}{2}\left[\frac{\omega_m}{s} - \Omega_L(r, z, s)\right] + \frac{\partial^2\Omega_L(r,z,s)}{\partial r^2} + \frac{3}{r}\frac{\partial\Omega_L(r,z,s)}{\partial r} + \frac{\partial^2\Omega_L(r,z,s)}{\partial z^2}$$ Eq. 4.3.3b)

$$M_L(s) = \frac{4I}{RH}\left[\int_0^R \left(\frac{r}{R}\right)^3 \frac{\partial\Omega_L(r,z,s)}{\partial z} dr - \int_0^H \frac{\partial\Omega_L(r,z,s)}{\partial r} dz\right]$$ Eq. 4.3.3c)

Similarly, Laplace transform of Eq. 4.3.2 is given by

$$\Omega_L(r, z = 0, s) = s\alpha_L(s)$$ Eq. 4.3.4a)

$$\frac{\partial}{\partial z}\Omega_L(r, z = H, s) = 0$$ Eq. 4.3.4b)

$$\Omega_L(r = R, z, s) = s\alpha_L(s)$$ Eq. 4.3.4c)

Eq. 4.3.3b) with boundary conditions Eq. 4.3.4a)-c) is solved by the method of variable separation,

$$\Omega_L(r, z, s) = \sum_{i=1}^{\infty} \frac{2R}{r\mu_i s_m} \frac{J_1(\mu_i r/R)}{J_0(\mu_i)}\left[1 - \frac{\cosh[(H-z)\sqrt{s_m}]}{\cosh(H\sqrt{s_m})}\right]\left[s s_E \alpha_L(s) - \frac{Ha^2\omega_m}{2s}\right] + s\alpha_L(s)$$
Eq. 4.3.5

with $s_m = s + \frac{Ha^2}{2} + \left(\frac{\mu_i}{R}\right)^2$ and $s_E = s + \frac{Ha^2}{2}$.

Substituting Eq. 4.3.5 into Eq. 4.3.3a) yields,

$$\alpha_L(s) = \frac{Ha^2\omega_m D(s)}{2s^2 s_E[(s+\Delta_0)^2 + D(s) + 1]}$$ Eq. 4.3.6

where,

$$D(s) = 8Iss_E \sum_{i=1}^{\infty} \frac{1}{s_m}\left[\frac{1}{R^2} + \frac{s_E}{\mu_i^2}\frac{\tanh(H\sqrt{s_m})}{H\sqrt{s_m}}\right]. \qquad \text{Eq. 4.3.7a)}$$

Other forms of $D(s)$ are written as

$$D(s) = Iss_E\left[1 - 16s_E \sum_{i=1}^{\infty}\sum_{i=1}^{\infty} \frac{1}{\mu_i^2\lambda_j^2\left[s_E+\left(\frac{\mu_i}{R}\right)^2+\left(\frac{\lambda_j}{H}\right)^2\right]}\right] \qquad \text{Eq. 4.3.7b)}$$

$$D(s) = Iss_E\left[1 - 8s_E \sum_{j=1}^{\infty} \frac{1}{\lambda_j^2 s_n}\left[\frac{I_2(R\sqrt{s_n})}{R\sqrt{s_n}I_1(R\sqrt{s_n})} - \frac{1}{4}\right]\right] \qquad \text{Eq. 4.3.7c)}$$

with $s_n = s + \frac{Ha^2}{2} + \left(\frac{\lambda_j}{H}\right)^2$, and $\lambda_j = \left(j - \frac{1}{2}\right)\pi$. Eq. 4.3.7a)-c) are fully equivalent and interchangeable. The conversion between each other can be deduced by the following series expansion,

$$\frac{I_2(x)}{2xI_1(x)} = \frac{1}{8} - \sum_{j=1}^{\infty} \frac{x^2}{(x^2+\mu_i{}^2)\mu_i{}^2} \qquad \text{Eq. 4.3.8a)}$$

$$\frac{\tanh(x)}{x} = 1 - 2\sum_{j=1}^{\infty} \frac{x^2}{\left[x^2+\lambda_j^2\right]\lambda_j^2} \qquad \text{Eq. 4.3.8b)}$$

Eq. 4.3.7 a) or c) is obtained by converting the infinite double series in Eq. 4.3.7b) to a single series in terms of i or j, respectively. Because only a finite number of terms are taken for numerical calculations of the infinite series, choosing appropriate form of $D(s)$ may reduce the truncation error. Generally, Eq. 4.3.7a) is better for squat liquid column, and Eq. 4.3.7c) for slim liquid column.

4.3.1.2. Features of characteristic equations

The inverse transform of Eq. 4.3.6 is taken to obtain the actual angular displacement of the cup. Similar to the 1D EMV model, Eq. 4.3.6 is a single-value function with three groups of poles: zero pole, an infinite number of negative real poles, and a pair of conjugate complexes. The poles besides $s = 0$ are roots of the characteristic equation,

$$1 + (s + \Delta_0)^2 + D(s) = 0 \qquad \text{Eq. 4.3.9}$$

The features of negative real roots are first examined. Substituting Eq. 4.3.7b) into Eq. 4.3.9 yields,

$$-\frac{1+(s+\Delta_0)^2}{s\left(s+\frac{Ha^2}{2}\right)} = Iss_E\left[1-16s_E\sum_{i=1}^{\infty}\sum_{i=1}^{\infty}\frac{1}{\mu_i^2\lambda_j^2\left[s_E+\left(\frac{\mu_i}{R}\right)^2+\left(\frac{\lambda_j}{H}\right)^2\right]}\right] \qquad \text{Eq. 4.3.10}$$

When both sides are plotted as a function of s to locate these negative roots, the same scheme to Fig. 4.2.2 will be obtained. Yet S_{ij}, which confines the interval ends, is given by $-\left[\frac{Ha^2}{2}+\left(\frac{\mu_i}{R}\right)^2+\left(\frac{\lambda_j}{H}\right)^2\right]$, rather than by $-\left[\frac{Ha^2}{2}+\left(\frac{\mu_i}{R}\right)^2\right]$ for the 1D EMV model. The presence of $\left(\frac{\lambda_j}{H}\right)^2$ contributes to the bottom effects. As H approaches infinite, $\left(\frac{\lambda_j}{H}\right)^2$ approaches zero, meaning the impact from the bottom is negligible comparing with the side wall. Just like the 1D model, there exists a single root s_k in the interval between any two consecutive S_{ij}. For instance, the largest root s_1 is always less than S_{11}, and larger than the second large S, either S_{12} or S_{21}. Numerical calculations are used to solve s_k in a sequence starting from s_1. The truncation error is sufficiently small when the last s is tenth larger than s_1 in magnitude.

Next, we solve for complex poles. The complex roots are defined as the same to that of 1D model, Eq. 4.2.23 is rewritten here as,

$$s_{\pm} = (-\Delta \pm i)\omega \qquad \text{Eq. 4.3.11}$$

Substituting Eq. 4.3.11 into Eq. 4.3.9 yields

$$1+(\Delta_0-\Delta\omega)^2-\omega^2+\mathrm{Re}D[(-\Delta\pm i)\omega]=0 \qquad \text{Eq. 4.3.12 a)}$$

$$\pm 2\omega(\Delta_0-\Delta\omega)+\mathrm{Im}D[(-\Delta\pm i)\omega]=0 \qquad \text{Eq. 4.3.12 b)}$$

from which Δ and ω are determined.

4.3.2. Transient Angular Displacement

The actual angular displacement of the cup is obtained by the residue theorem in a way as we did when developing the 1D model. The results are pretty similar,

$$\alpha(t) = \alpha_\infty + \alpha_T(t) + \alpha_T(t) \qquad \text{Eq. 4.3.13}$$

with

$$\alpha_\infty = \mathrm{Res}(s=0) = \frac{\omega_m}{1+\Delta_0^2}\lim_{s\to 0}\frac{D(s)}{s}, \qquad \text{Eq. 4.3.14a)}$$

$$\alpha_D(t) = \sum \mathrm{Res}(s=s_\pm) = \sum_{s=s_\pm}\frac{Ha^2\omega_m D(s)}{s(2s+Ha^2)[2(s+\Delta_0)+D'(s)]}e^{st}, \qquad \text{Eq. 4.3.14b)}$$

$$\alpha_T(t) = \sum_{k=1}^{\infty} \mathrm{Res}(s = s_k) = \sum_{k=1}^{\infty} \frac{Ha^2 \omega_m D(s_k)}{s_k(2s_k + Ha^2)[2(s_k + \Delta_0) + D'(s_k)]} e^{s_k t}. \quad \text{Eq. 4.3.14c)}$$

α_∞, α_D and α_T represent the angular position at final equilibrium, the damped oscillation, and the fast decay, respectively. It is noted that the modification of $D(s)$ is the only change as the 1D solution extends to the 2D one.

4.4. Numerical Experiments

Numerical experiments are performed to better illustrate the usage of rapid measurement method and QSS measurement method. The noises in real experiments are simulated, and they produce different measurement errors dependent on the measurement method, the process of processing data, and the experimental conditions. The measurement errors are compared to seek for the optimal experimental conditions and the better measurement method.

4.4.1. Description of Experiments

To numerically generate experimental data with desired Ha and R, Eqs. 3.13 and 3.14 are first calculated for a lifelong motion of the cup under conditions of $\Delta_0 = 0.0017$, $I = 0.0262$, $H/R = 11.83$ and $\omega_m = 958.3$. These conditions agree with the previous experiments. N Number of calculations are carried out in each cycle, and the time difference between any two consecutive calculations is equal. Next, small disturbances are added up to the calculated $\alpha(t)$ to simulate the noises from real measurements. They are assumed to follow the normal distribution with mean 0 and standard deviation 0.01. Finally, the generation of data are repeated 10 times, each of which is separately fitted for the corresponding Ha and R. The mean of the ten values is taken as the final result.

The generated data are fitted to determine Ha and R, just like the data processing in real experiments. In rapid measurement method, the cycles before the quasi-steady state are generally used for calculations. The QSS time is defined as the moment when fast decay falls to 0.01γ, or the start of the quasi-steady state. In some cases that fast decay vanishes too fast to form a few cycles, such as the one with QSS time of 11.4 as shown in Fig. 4.4.1, 8 cycles are used instead. Overall, the duration in which the data are used for fitting is between 0 and the maximum of QSS time and 50, as shown in Fig. 4.4.2. The values of Ha and R are then determined by the method of least squares, to yield the best fit between the solution of Eqs. 3.13 and 3.14 and these data.

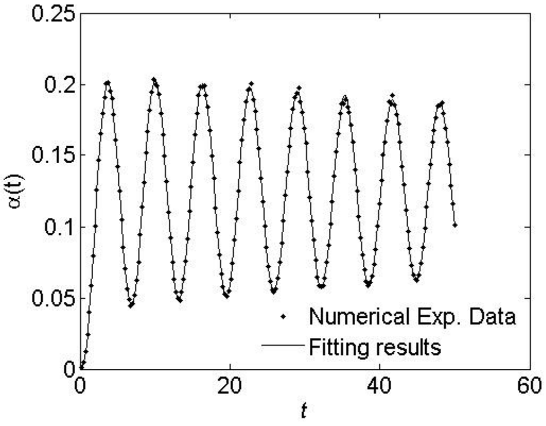

Fig. 4.4.1 Numerical Experiment with $R = 5, Ha = 0.1$ and $N = 25$

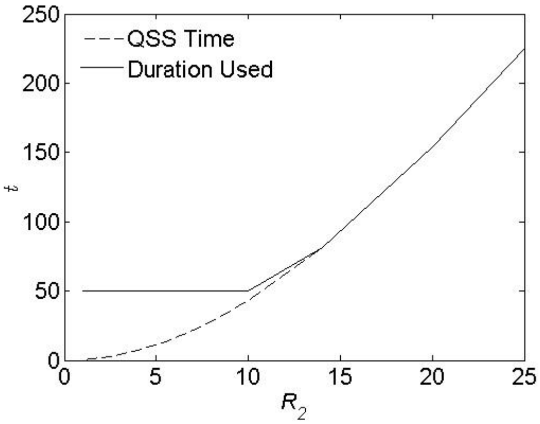

Fig. 4.4.2 Duration used for Rapid Measurements at $Ha = 0.1$

In the QSS method, all the cycles after the QSS time are compared with the model to fit the values of Δ and α_∞. They are substituted to the coupled equations of Eqs. 2.24a), 2.24b) and Eq. 4.3.14a), from which Ha, R and ω are solved.

It is apparent that the fitted values of Ha and R are different from those used for the generation of original data. The difference is the measurement errors caused by the noises in measurements. It is noteworthy to mention that the measurement errors caused by the uncertainties of Δ_0, I, H, and ω_m are not taken into account, as their true values are used during fitting. Regardless of the influence of all the other uncertainties, the relative measurement errors of electrical conductance and viscosity are given by

$$Er_\sigma = \left|\frac{Ha_m^2 - Ha_a^2}{Ha_a^2}\right| \times 100\% \qquad \text{Eq. 4.3.15a)}$$

$$Er_\upsilon = \left|\frac{R_m^2 - R_a^2}{R_a^2}\right| \times 100\% \qquad \text{Eq. 4.3.15b)}$$

where Er notes for the relative measurement error, the subscript a for the actual or original values, and the subscript m for the measured or fitted values.

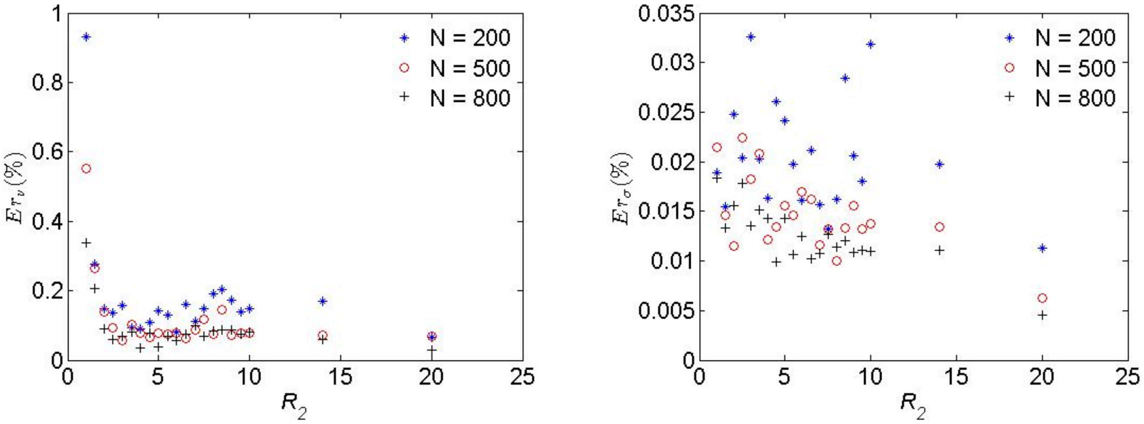

Fig. 4.4.3 Comparison of Errors from Rapid measurements at $N = 200,500$ and 800 ($Ha = 0.01$)

Numbers of points in a cycle affects the measurement errors. Fig. 4.4.3 compares the relative errors of electrical conductance and viscosity measured from the rapid method for $N = 200,500$ and 800. The differences of the relative errors between $N = 500$ and $N = 800$ are not considerable, suggesting that 500 points per cycle is a sufficient number for fitting. Nonetheless, $N = 200$ is used for all latter calculations to speed up the computation.

4.4.2. Measurement Errors

Fig. 4.4.4 plots the relative errors of electrical conductance and viscosity measured by the rapid method. Two conclusions are drawn through the observation of these figures. First, the measurements have higher accuracy for $Ha \leq 0.1$, as the measurement errors at $Ha = 0.56$ are much larger than those at $Ha = 0.01$ and 0.1. The errors at $Ha = 0.1$ are pretty close to those at $Ha = 0.01$. Second, the measurements with $R < 2.5$ should be avoided as they lead to much larger errors.

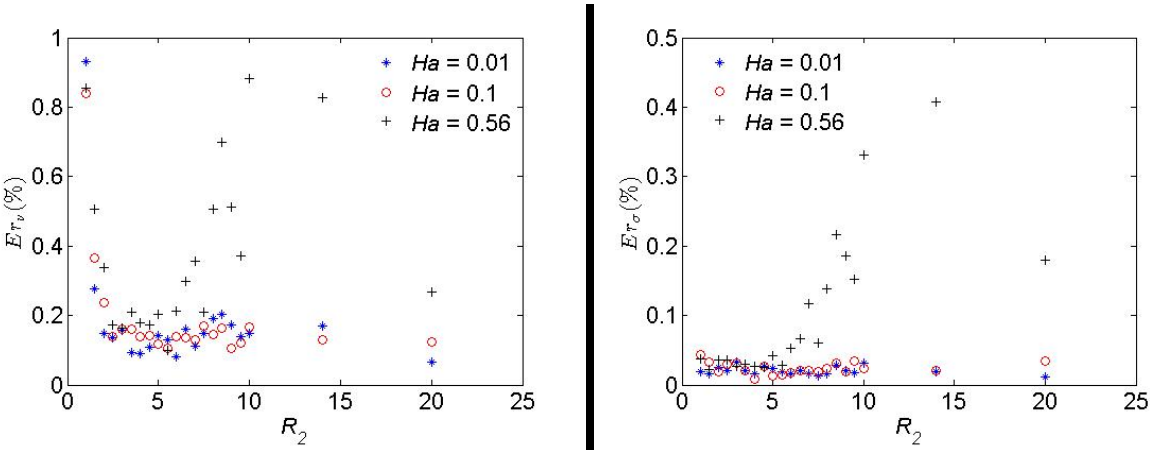

Fig. 4.4.4 Relative Errors by Rapid Measurements

Fig. 4.4.5 plots the relative errors of electrical conductance and viscosity measured by the QSS method. The features of measurement errors can be well explained by the dependence of α_∞ and $\Delta - \Delta_0$ as show in Fig. 4.2.7 and 2.9. First, the errors of viscosity tend to increase with the increase of R_2 for $Ha = 0.01$ and 0.1. Because α_∞ is barely dependent on R_2 for small Ha as shown in Fig. 4.2.7a), the viscosity is determined only from the dependence of $\Delta - \Delta_0$, which becomes weaker for larger R_2 as shown in Fig. 4.2.7b). Thus, the increase of R_2 leads to larger errors. Second, when Ha rises up to 0.56, the increase of R_2 significantly reduces the errors in the range of $5 < R_2 < 15$. It is because the strong dependence of α_∞ plays an important role to improving the measurement accuracy.

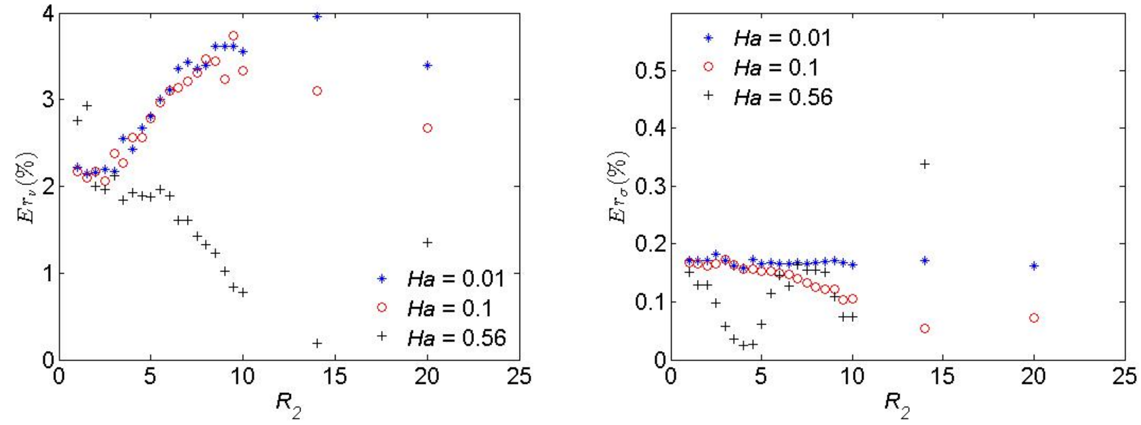

Fig. 4.4.5 Relative Errors by QSS Measurements

By comparing the measurement errors from both methods, it is noticed that the rapid method generally has better measurement accuracy. When appropriate Ha and R are set, the measurement errors of viscosity are as low as 0.15% or so by the rapid method, against 1% or so by the QSS method. And the errors of electrical conductance are about 0.02% by the rapid method, against 0.1-0.2% by the QSS method. A better accuary is achieved by the rapid method, because it takes full usage of all the information.

5. NEW STEPPED CYLINDER DESIGN

An analytical model for the stepped-cylindrical EMV will be developed in this section. We have established two models for a single-cylindrical EMV in which fluid is hold in a cylindrical cup. Such an EMV is improved by replacing with a stepped-cylinder cup, which consists of a squat cylindrical container attached to a tube of narrow diameter. The improved EMV is called a stepped-cylindrical EMV.

Simultaneous measurement of density together with viscosity and electrical conductance improves the applicability of the EMV method. Density of the fluid is of importance not only because it is one of the essential physical properties, but also because its value must be known to calculate Ha and I in the EMV measurements. If density can be determined from the EMV measurements to save extra efforts, it becomes more convenient to use the EMVs. The same desire exists for the traditional oscillating viscometers as well.

It is possible for a stepped-cylindrical EMV to fulfill the purpose of simultaneous measurement of density. According to our 1D model, the change of density in a cylindrical cup does change any experimental conditions but the Hartmann number, Ha. Because both electrical conductance and density are coupled in Ha, it rules out any feasibility of measuring them at the same time. In practical, the value of density is usually obtained from other references or experiments, leaving the electrical conductance to be determined from the EMV measurements. When a stepped-cylindrical cup is used instead, the volume change of fluid is capable of significantly changing the momentum inertia, to which the motion of the cup is extremely sensitive. Thus, it becomes feasible to measure density through the observed motion of the cup.

The replacement of the stepped-cylinder cup is also expected to improve the measurement accuracy. Evaporation effects and meniscus effects have been suggested to be two major sources of measurement errors for the OCV measurements. Evaporation effects occurs as the fluid evaporates in the closed cup, resulting into the reduce of fluid and extra damping effects due to the vapor. Meniscus effects occurs due to the meniscus shape in the upper surface of fluids close to the side wall of the cup. It changes the height of the fluid column as well as the viscous shear. They can affect the EMV measurements in the same way. However, when fluid is hold in a stepped-cylindrical cup, the empty space above the fluid and the upper surface of the fluid are reduced because of the narrow size of the tube. Thus, evaporation effects and meniscus effects can be significantly suppressed.

In this section, an analytic model for the stepped-cylindrical cup is established on purpose of verifying the feasibility of simultaneous measurement of density, viscosity, and electrical conductance. Due to the common features between EMVs and OCVs, the replacement can also be applied to the traditional OCVs to perform simultaneous measurement and to improve measurement accuracy.

5.1. Analytical Model

5.1.1. Physical Description

Fluid is hold in a stepped-cylindrical cup in the improved stepped-cylindrical EMV. The cup consists of a cylinder container connected a tube. The tube is much smaller than the container in diameter as schemed in Fig. 5.1.1. The fluid fills the whole container and part of the tube, leaving the upper part of the tube empty. The fluid in the tube is much less than that in the container in volume. When the fluid changes in volume due to thermal expansion, the fluid column rises up or falls down in the tube.

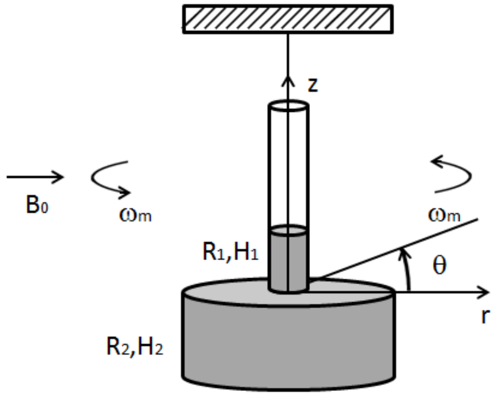

Fig. 5.1.1 Schematic of a stepped-cylindrical EMV

5.1.2. Mathematic Description

The physical mechanisms in a single-cylindrical EMV are identical to the single-cylindrical EMVs as described before. The motion of the cup is described by the following dimensionless equation with its initial condition,

$$\frac{d^2\alpha(t)}{dt^2} + 2\Delta_0\frac{d\alpha(t)}{dt} + (1+\Delta_0^2)\alpha(t) = M(t) \qquad \text{Eq. 5.1.1a)}$$

$$\alpha(t=0) = 0 \qquad \text{Eq. 5.1.1b)}$$

To model the motion of the fluid, the following assumptions are used: a) Fluid flows around the z direction, while no secondary motion exists. This assumption eliminates the convective acceleration term in the Navier-Stokes equation. b) The viscous force at the interacting surface through which the tube is connected to the container has insignificant influence on the flow in the tube. c) The connection between the tube and the container has negligible influence on the flow inside the container so that the container is simply regarded as an enclosed cylindrical cup.

This assumption is acceptable when the tube is much narrower than the container. d) There is no slip of fluid at all walls.

Based on these assumptions, the flow in the tube is described by the following governing equation, as well as its boundary and initial conditions,

$$\frac{\partial \Omega_1(r,z,t)}{\partial t} = \frac{Ha^2}{2}\left(\omega_m - \Omega_1(r,z,t)\right) + \frac{\partial^2 \Omega_1(r,z,t)}{\partial r^2} + \frac{3}{r}\frac{\partial \Omega_1(r,z,t)}{\partial r} \qquad \text{Eq. 5.1.2a)}$$

$$\frac{\partial}{\partial z}\Omega_1(r, z=0, t) = \frac{\partial}{\partial z}\Omega_1(r, z=H_1, t) = 0 \qquad \text{Eq. 5.1.2b)}$$

$$\Omega_1(r=R_1, z, t) = \frac{d\alpha(t)}{dt} \qquad \text{Eq. 5.1.2c)}$$

$$\Omega_1(r, z, t=0) = 0 \qquad \text{Eq. 5.1.2d)}$$

where Ω_1, R_1, and H_1 are the angular velocity of fluid, and the radius and the height of the fluid column in the tube, respectively. Because there is no viscous effects at the top and bottom surfaces, the flow is uniform along the z direction, becoming an 1D phenomena.

The flow in the container is governed by

$$\frac{\partial \Omega_2(r,z,t)}{\partial t} = \frac{Ha^2}{2}\left(\omega_m - \Omega_2(r,z,t)\right) + \frac{\partial^2 \Omega_2(r,z,t)}{\partial r^2} + \frac{3}{r}\frac{\partial \Omega_2(r,z,t)}{\partial r} + \frac{\partial^2 \Omega_2(r,z,t)}{\partial z^2} \qquad \text{Eq. 5.1.3a)}$$

$$\Omega_2(r < R_2, z=0, t) = \Omega_2(r, z=-H_2, t) = \Omega_2(r=R_2, z, t) = \frac{d\alpha(t)}{dt} \qquad \text{Eq. 5.1.3b)}$$

$$\Omega_2(r, z, t=0) = 0 \qquad \text{Eq. 5.1.3c)}$$

where Ω_2, R_2, and H_2 are the angular velocity of fluid, and the inner radius and the height of the container, respectively.

The viscous torque is caused by the viscous shear on all the walls, yielding

$$M(t) = -4\frac{I_1}{R_1}\frac{\partial \Omega_1(r=R_1,t)}{\partial r} + \frac{4I_2}{R_2H_2}\left[\int_0^{R_2}\left(\frac{r}{R_2}\right)^3 \frac{\partial \Omega_2(r,z=-H_2,t)}{\partial z}dr - \int_{-H_2}^{0}\frac{\partial \Omega_2(r=R_2,z,t)}{\partial r}dz - \int_{R_1}^{R_2}\left(\frac{r}{R_2}\right)^3 \frac{\partial \Omega_2(r,z=0,t)}{\partial z}dr\right] \qquad \text{Eq. 5.1.4}$$

where I_1 and I_2 are the dimensionless moment inertia of fluid in the tube and in the container, respectively, with $I_1 = \frac{\pi}{2}\bar{\rho}\bar{R}_1^4\bar{H}_1/\bar{I}_0$ and $I_2 = \frac{\pi}{2}\bar{\rho}\bar{R}_2^4\bar{H}_2/\bar{I}_0$.

5.1.3. Transient Angular Displacement

Laplace transform method is used to solve Eqs. 4.2.1-4.2.4 as we have done in last two sections.

The Laplace form of its angular velocity in the tube is the same to Eq. 5.1.8, which is rewritten as

$$\Omega_{L1}(r,s) = \left[s\alpha_L(s) - \frac{Ha^2\omega_m}{s(2s+Ha^2)}\right]\frac{R}{r}\frac{I_1\left(r\sqrt{s+\frac{Ha^2}{2}}\right)}{I_1\left(R\sqrt{s+\frac{Ha^2}{2}}\right)} + \frac{Ha^2\omega_m}{s(2s+Ha^2)} \qquad \text{Eq. 5.1.5}$$

Because the flow is symmetric around the half-height plane in the container, Ω_{L2} can be easily obtained from Eq. 4.3.5 by adapting the height to $H_2/2$,

$$\Omega_{L2}(r,z,s) = \sum_{i=1}^{\infty}\frac{2R_2}{r\mu_i s_m}\frac{J_1(\mu_i r/R_2)}{J_0(\mu_i)}\left[1 - \frac{\cosh[(H_2/2+z)\sqrt{s_m}]}{\cosh(H_2\sqrt{s_m}/2)}\right]\left[ss_E\alpha_L(s) - \frac{Ha^2\omega_m}{2s}\right] + s\alpha_L(s), \qquad \text{Eq. 5.1.6}$$

with $s_m = s + \frac{Ha^2}{2} + \left(\frac{\mu_i}{R_2}\right)^2$ and $s_E = s + \frac{Ha^2}{2}$.

Substituting Eqs. 4.2.5 and 4.2.6 into the Laplace form of Eqs. 4.2.4 and 4.2.1, the angular displacement of the cup is given by

$$\alpha_L(s) = \frac{Ha^2\omega_m D(s)}{2s^2 s_E[1+(s+\Delta_0)^2+D(s)]} \qquad \text{Eq. 5.1.7}$$

where,

$$D(s) = \frac{4I_1 s\sqrt{s_E}}{R_1}\frac{I_2(R_1\sqrt{s_E})}{I_1(R_1\sqrt{s_E})} + 8I_2 ss_E\sum_{i=1}^{\infty}\frac{1}{s_m}\left[\frac{1}{R_2^2} + \frac{2s_E}{\mu_i^2}\frac{\tanh(H\sqrt{s_m}/2)}{H\sqrt{s_m}}\right] + 8I_2 ss_E\sum_{i=1}^{\infty}\left(\frac{R_1}{R_2}\right)^2\frac{J_2(\mu_i R_1/R_2)}{\mu_i^2 J_0(\mu_i)}\frac{\tanh(H\sqrt{s_m}/2)}{H\sqrt{s_m}} \qquad \text{Eq. 5.1.8}$$

The solution is not different from those established for the 1D and 2D model, except the expression of $D(s)$. The first term in the RHS of Eq. 5.1.8 contributes to the viscous shear on the tube, the second one results from the contact of fluid with all the surfaces of an imaginary enclosed container, and the third one compensates for the loss of the contact surfaces due to the opening at the top walls.

In a similar way to infer the expression of the actual angular displacement of the 1D model, the inverse Laplace transform of Eq. 5.1.8 yields

$$\alpha(t) = \alpha_\infty + \alpha_T(t) + \alpha_T(t) \qquad \text{Eq. 5.1.9}$$

with

$$\alpha_\infty = \mathrm{Res}(s=0) = \frac{\omega_m}{1+\Delta_0^2}\lim_{s\to 0}\frac{D(s)}{s}, \qquad \text{Eq. 5.1.9a)}$$

$$\alpha_D(t) = \sum \mathrm{Res}(s = s_\pm) = \sum_{s=s_\pm} \frac{Ha^2 \omega_m D(s)}{s(2s+Ha^2)[2(s+\Delta_0)+D'(s)]} e^{st}, \qquad \text{Eq. 5.1.9b)}$$

$$\alpha_T(t) = \sum_{k=1}^{\infty} \mathrm{Res}(s = s_k) = \sum_{k=1}^{\infty} \frac{Ha^2 \omega_m D(s_k)}{s_k(2s_k+Ha^2)[2(s_k+\Delta_0)+D'(s_k)]} e^{s_k t}. \qquad \text{Eq. 5.1.9c)}$$

5.2. Results and Analysis

The study is to examine the feasibility of simultaneously measuring the density, viscosity, and electrical conductance in a stepped-cylindrical EMV. Because the replacement of the stepped-cylindrical cup cause no difference in the measurements of viscosity and electrical conductance, as we will show later, our analysis mainly focus on the impact of various density on the motion of the cup.

The motion of the cup is exclusively characterized by a group of dimensionless numbers, including γ, τ, α_∞, A, ω, ψ and Δ, which are defined by Eqs. 5.1.29-32. They are determined by comparing Eqs. 5.1.29-32 with the solution of Eq. 5.1.9. In our calculations, $H_2 = 2R_2$, $I_2 = 0.02$, $H_1 = R_1$ and $Ha = 0.1$ unless other specific values are given. A series of R_1/R_2 of 0.01, 0.1 and 0.2 are used to examine the impact of the geometry of the cup. In extreme case of $R_1/R_2 = 0.01$, the stepped-cylindrical cup functions as an enclosed cylindrical container full of fluid in terms of the EMV measurements, in spite of the mass exchange between the container and the tube.

5.2.1. Measurement of Viscosity and Electrical Conductance.

The response of the motion of the cup to the change of viscosity is shown in Figs. 4.2a) and b). The independent variable R_2 acts as viscosity as R_2 is a function of only viscosity for a specific system. The values of R_1, H_1, and H_2 adapt to the change of R_2 in calculations, assuming the cup is unchanged in geometry. It is seen from Figs. 4.2a)-d) that the curves of τ and Δ are completely or almost overlapped for a variety of R_1/R_2. Such a feature exists for the remaining dimensionless numbers, γ, A, α_∞, ψ, and ω, which are not plotted.

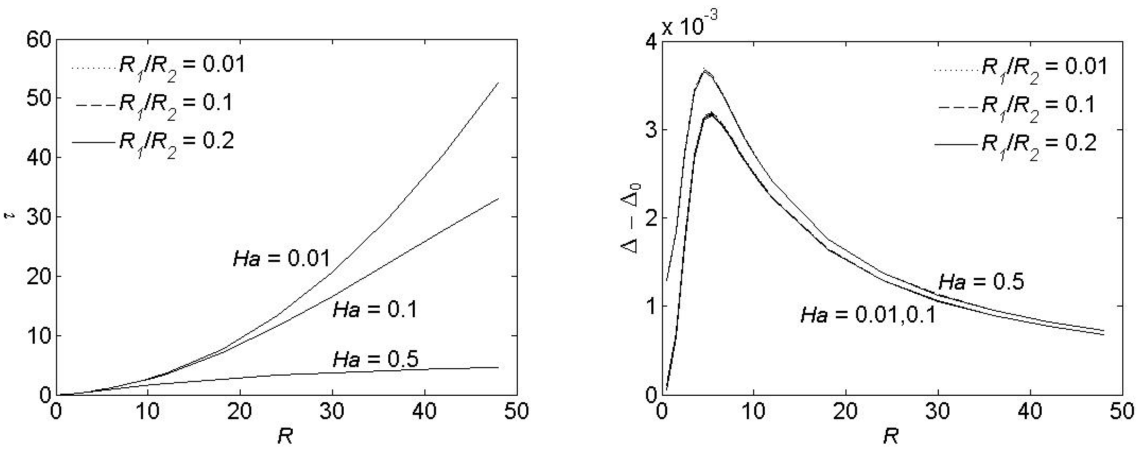

a) τ vs. R_2 b) Δ vs. R_2

Fig. 5.2 Response of Angular Displacement to Change of Viscosity

Figs. 4.3a) and b) plot τ and Δ with the change of electrical conductance, respectively, as examples of the response of the motion of the cup. Similar to Fig. 5.2, all curves are overlapped with each other for a variety of R_1/R_2.

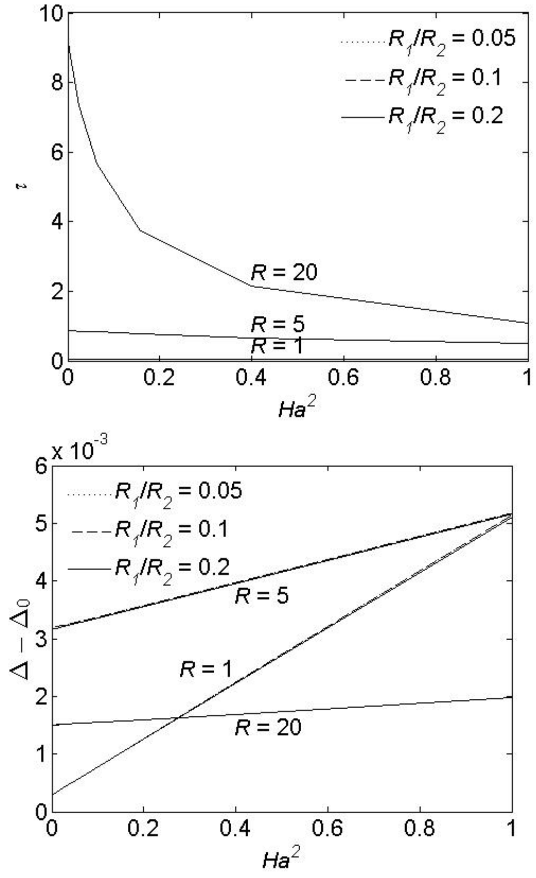

a) τ vs. Ha^2 b) Δ vs. Ha^2

Fig. 5.3 Response of Angular Displacement to Change of Electrical Conductance

The independence of R_1/R_2 shown in Figs 4.2 and 4.3 implies that the addition of the tube has no impact on the measurements of viscosity and electrical conductance of fluid in the container, provided that the tube is much narrower than the container. It is explained by the fact that the moment of inertia of the fluid in the tube is less than that in the container by a few orders of magnitude, as the moment of inertia has a fourth power relationship with the diameter. According to our 1D single-cylindrical model, the strength of all components of the angular displacement varies linearly with the moment of inertia of fluid. It means that the motion of the cup is mostly controlled by the fluid in the container, while the fluid in the tube causes only a negligible disturbance. Therefore, in terms of the measurements of electrical conductance and viscosity, a stepped-cylindrical EMV works just like a single-cylindrical EMV with an enclosed cup full of fluid.

5.2.2. Measurement of Density

In a specific suspension system, the variation of density affects the motion of the cup mainly via changing I_2 and Ha, and they they follow the relationship of $\rho \sim I_2 \sim Ha^{-2}$. I_1 is the remaining parameter that is subject to the change of density. However, the change of I_1 is less than that of I_2 by a factor of $(R_1/R_2)^2$. For instance, when half of the fluid is expelled out of the container due to thermal expansion in a stepped-cylindrical cup with $R_1/R_2 = 0.1$, I_2 will decrease by half, while I_1 increases by only $0.005I_2$. As a consequence, the overall moment of ineria of fluid in a stepped-cylindrical cup strongly relies on density, although the total mass of fluid never changes in such an enclosed system. The variation of moment of inertia distinguishes the stepped-cylindrical EMV from the single-cylindrical EMV.

The response of angular displacement to the change of density is plotted in Fig. 5.4a)-g). As the density varies from 0.3 to 1 in these figures, the corresponding Ha^2 decreases from 0.033 to 0.01, and I_2 increases from 0.06 to 0.2.

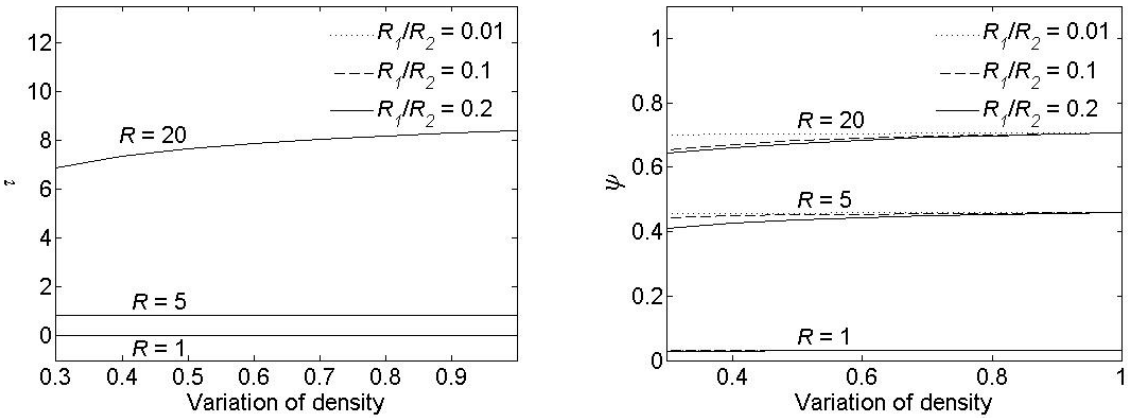

a) τ vs. Variation of Density

b) ψ vs. Variation of Density

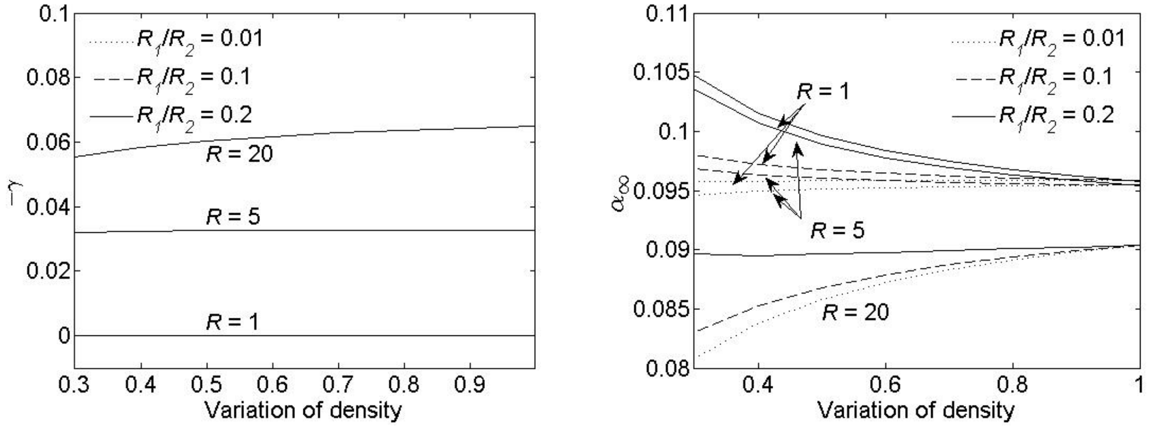

c) γ vs. Variation of Density

d) α_∞ vs. Variation of Density

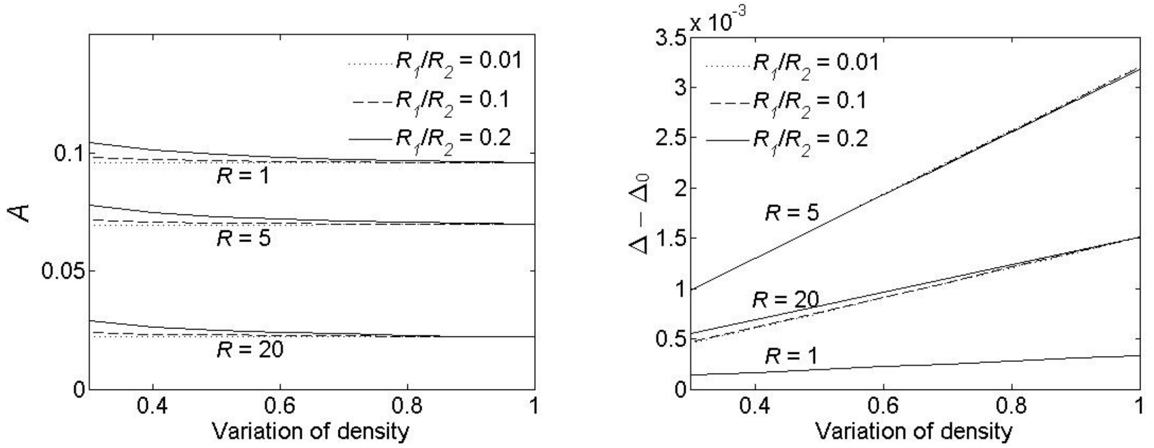

e) A vs. Variation of Density

f) Δ vs. Variation of Density

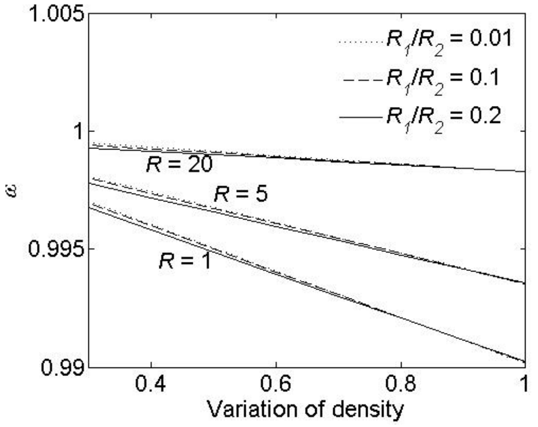

g) ω vs. Variation of Density

Fig. 5.4 Response of Angular Displacement to Change of Density

Generally, the response to the change of density is in accordance with our earlier analyses from the 1D single-cylindrical model, if we regard the repsonse as the co-contribution of changes of both I_2 and Ha. For example, τ is indepdent of the change of moment of inertia according to the 1D model. Hence, the change of Ha alone contributes the most to the variation of τ. It explains that the curves in Fig. 5.4a) agree well with the ones in Fig. 5.5b) for Ha^2 between 0.033 and 0.01. Another example is the variation of Δ. It should be seen from Fig. 5.9b) that the decease of Ha^2 from 0.033 to 0.01 linearly decreases $\Delta - \Delta_0$ by only less than 10%, while the increase of I_2 from 0.06 to 0.2 almost triples $\Delta - \Delta_0$. As a result of the overwhelming contribution of I_2, the curves of $\Delta - \Delta_0$ straightly clime in Fig. 5.4f), with slopes corresponding to the values of $(\Delta - \Delta_0)/I$ in Fig. 5.9b).

In addition, the response to the change of density is slightly dependent on the value of R_1/R_2. Some curves are clearly varied for a variety of R_1/R_2 in Fig. 5.4. The dependence is attributed to the different change of I_1 in the tubes with different R_1, even if the fluid exchange is the same.

Overall, $\Delta - \Delta_0$ is the most senstive parameter with the change of density. Actrually, the other parameters only slightly reponds to the change of density in comparison with the repsonses to changes of electrical conductance or viscosity. Because the information collected from the motion of the cup is much more than what is necessary for determing the electrical conductance and visocity, the dependence of $\Delta - \Delta_0$ can be saved somehow to measure the density. If doing so, the increase of $(\Delta - \Delta_0)/I_2$ is likely to reduce the errors of measureing density. The largest value of $(\Delta - \Delta_0)/I_2$ occures at $R_2 = 5$ according the 1D single-cylindrical model.

5.3. Step Cylinder Summary

An analytical model for a stepped-cylindrical EMV has been established with a few assumptions: the uncoupling of fluid flow in the tube and in the container, negligible advective flow, and negligible opening effects on the flow in the container. Calculations are carried out to plot the response of the motion of the cup to the change of viscosity, electrical conductance, and density in stepped-cylindrical EMVs. From the analysis of the responses, it is concluded that a stepped-cylindrical EMV with a narrow tube is not quite different from a single-cylindrical EMV in terms of measuring electrical conductance and viscosity. The analysis also suggests the feasibility of simultaneously measuring density, because the damping ratio of the oscillation is very sensitive to the change of density.

In future studies, numerical simulations for the behavior of a stepped-cylindrical EMV are needed to examine the accuracy of the current model. Based on the simulation results, the current model will be corrected in need, so that it is applicable for predicting electrical conductance, viscosity, and density in sufficiently high accuracy.

6. EXPERIMENTAL

6.1. General Principle

The measurement principle of this proposed project will be the oscillation type and will be based on the previous work on the transient torque and oscillation-cup viscometer. The advantage of this non-intrusive, contactless technique method is its operation at high temperatures, sealed sample container, and possible adaptation to glovebox application. For instance, the PI's previous research for NASA was on compound semiconductor melts containing mercury, cadmium, and tellurium, which has a high vapor pressure (up to 30 atm), high temperature (up to 1100 C), and a toxic vapor.

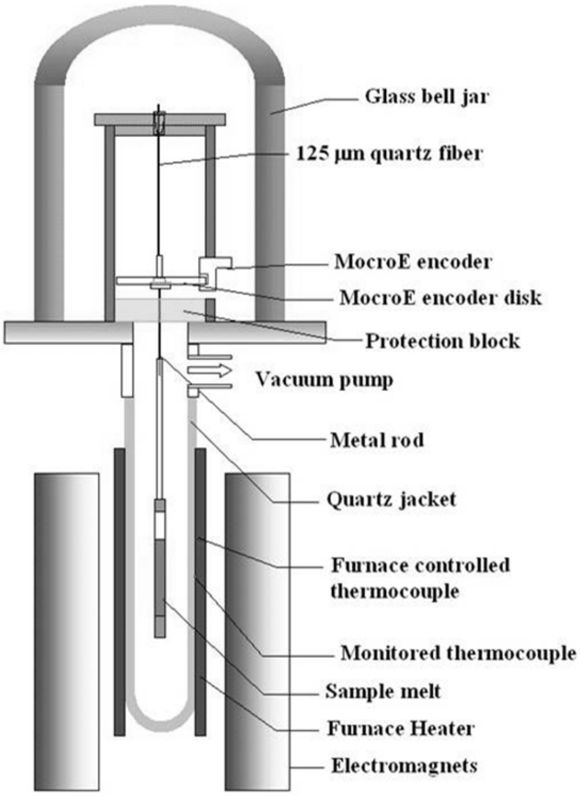

FIGURE 6.1: Schematic of the transient-torque/oscillation cup measurement system.

The schematic diagram of the transient torque/oscillation cup viscosity measurement system is shown in Figure 2. The melt sample is sealed inside a quartz ampoule, and the ampoule is suspended by a long quartz fiber or tungsten wire to form a torsional oscillation system. For the transient torque method, a rotating magnetic field is used to induce a rotating flow in the conductive melt, which causes the ampoule to rotate and oscillate around its vertical axis. A high resolution angle detector is used to measure the torsional oscillation angle of the ampoule. Based on the transient behavior of the angle after the rotating magnetic field is applied, the viscosity of the melt can be determined based on the melt viscous force on the ampoule wall. In addition, the electrical conductivity of the melt can also be determined simultaneously with viscosity. For the operation in oscillation cup mode, an initial torsional oscillation of the ampoule will be damped down after the rotating electromagnetic field is turned off. The viscous damping of the ampoule oscillation by the fluid can be used to calculate the fluid viscosity. There are two physically interacting systems involved: a torsional oscillation system consisting of the ampoule assembly suspended by the fiber, and the liquid flow driven by the rotating magnetic field. The interaction between the two systems is on their interface: the viscous shear of the liquid exerts a torque on the ampoule inner wall under the no-slip boundary condition for the liquid. These two systems can be described by respective governing equations with initial and boundary conditions. For ampoule torsional oscillation, the deflection angle of the ampoule at time t, α(t), measuring from the initial position when the fluid is motionless, can be described by the following oscillation equation:

$$I\frac{d^2\alpha(t)}{dt^2}+C\frac{d\alpha(t)}{dt}+k\alpha(t)=M(t), \qquad \text{Eq. 6.1}$$

where *I* is the moment of inertia of the ampoule assembly without the liquid, *C* is the damping coefficient which is mainly related to the internal friction of the fiber suspending the ampoule assembly (not the damping of the liquid inside the ampoule) and *k* is the torsional spring constant of the fiber. The torque exerted on the ampoule wall *M(t)* by the liquid shear inside the ampoule, which is a function of the viscous shear on the wall, is expressed by:

$$M(t)=-2\pi R^2 h\rho\nu\left.\frac{dV_\theta(r,t)}{dr}\right|_{r=R} \qquad \text{Eq. 6.2}$$

where *R* is the inner radius of the ampoule, *h* is the height of the fluid, ρ is the density of the fluid, ν is the kinematic viscosity of the fluid, and V_θ *(r, t)* is the tangential fluid velocity in cylindrical coordinates *(r, θ, z)*. The liquid flow can be treated as two dimensional planar and axis-symmetric because the height of the fluid column is much larger than its diameter. Therefore, the Navier-Stokes equation for the laminar flow has only the tangential component

$$\frac{\partial V_\theta(r,t)}{\partial t}=\frac{f}{\rho}+\nu\left(\frac{\partial^2 V_\theta(r,t)}{\partial r^2}+\frac{1}{r}\frac{\partial V_\theta(r,t)}{\partial r}-\frac{V_\theta(r,t)}{r^2}\right), \qquad \text{Eq. 6.3}$$

where *f* is the Lorentz body force cause by the rotating magnetic field. Equations 1-3 can be solved with proper initial and boundary conditions to describe the transient deflection angle. Because the parameters in these equations can be determined, the unknown liquid properties, viscosity and electrical conductivity, can be obtained by solving the inverse problem with coupled fluid flow and ampoule oscillation.

The instrument parameters, namely, the moment of inertia (*I*), the damping coefficient (*C*), and the torsional spring constant (*k*) for the suspended-ampoule assembly must be determined accurately. Specifically, the instrument parameters (*I, C, & k*) of each ampoule assembly need to be determined due to potential differences in each individual ampoule. The method determines the instrument parameter (*I, C, & k*) can be similar to that used in the oscillation cup method described by Thresh, which uses a free oscillation process by adding two additional metal rings with known moments to the oscillation system. The damping constant, as a property of the tungsten wire or quartz fiber, is measured using a solid metal sample attached to the same fiber suspension by conducting a free oscillation experiment. For samples that solidified at room temperatures, the solidified sample can be used instead of using a different solid to determine the actual damping constant of the system.

There will be significant technical challenges to develop a viscosity measurement system that can measure melts up to 1400 C, which is the typical range for fuel melts. The challenges include material selection for the oscillation apparatus, ampoule material selection and the coatings for the interior of the ampoule to prevent chemical interactions of the melt and the ampoule. Due to the high operational temperatures, most components must be rated for high temperatures and the system must be designed and built with the intention for the eventual use for U-Pu-Zr based alloys. Another challenge is how to make a furnace that can maintain the required temperature while having minimum interference with the electromagnetic field. System shakedown, tuning, and calibration also require significant experience and time.

The scientific merit of this project has three main aspects in advancing the state of knowledge in measurement science, and the fuel fabrication program of FCRD. First, there is no such measurement system in this temperature range for nuclear fuels in the world. The new transient torque/oscillation cup system will provide a unique capability for the measurement of viscosity, which is an advance in the general measurement of science and technology. Second, the capability of determination of required properties for the advanced fuel program provides needed fundamental information for the understanding of the behavior of the melts, because viscosity is the most important property to show melt structure and phase transformations. Third, the viscosity data obtained can significantly improve the accuracy of computational modeling of the casting process for metal fuels because, as stated earlier, there is no such data available and viscosity is the most important fluid property that governs the melt flow.

After the transient torque viscometer was set up, a seven nines grade mercury sample was used to verify the transient torque method for determining electrical conductivity and viscosity. This is because the electrical conductivity and viscosity of mercury are easily measured in the temperature range from room temperature to 473 K and the data for mercury are published by Dyos and Farell. The electrical conductivity and the viscosity of mercury at 326.6, 351.8, and 377.0 K were measured using a transient torque viscometer for the verification of the transient torque method. The main advantage of this method is that the measurement of both electrical conductivity and viscosity can be completed in 1 or 2 min, as opposed to the 1- or 2-h measurement required using the oscillation cup method, which can only be used to measure viscosity. Thus, the transient torque method is a non-intrusive method that is capable of rapid and simultaneous determination of the electrical conductivity and viscosity of a liquid.

6.2. Experimental Parameters

The torsion wire chosen for ampoule suspension is a quartz fiber instead of a tungsten wire, which is usually used for the oscillation cup viscometers. The quartz fiber experiences almost no plastic deformation as a function of time, and the torsional spring constant is also smaller to enable a longer oscillation period, which reduces relative measurement errors. The quartz fiber is 125 μm in diameter and approximately 26.2 cm long. One end of the fiber is glued to an aluminum disk, and the other end is glued to the center of the encoder stand, as shown in Fig. 4.2. The ampoule containing the sample is attached to the center of the encoder stand by a rigid metal and quartz tube to reduce the effect of "wobbling motion" on the measurements. The ampoule is positioned at the center of the RMF by adjusting the position of the aluminum disk on top of the assembly.

The RMF is generated by a set of electromagnets. Each electromagnet consists of a series of coils placed in the stator core and connects to form 3-phase Y-connection windings. A Pacific 330-AMX series power supply is used to provide power for each phase. The power supply is capable of separately adjusting the voltage applied to each phase of the electromagnets in order to obtain a suitable magnetic field at the center of the electromagnets for the transient torque viscometer.

A uniform magnetic field was required for the transient torque method to carry out the measurement of the electrical conductivity and viscosity of the liquid sample. By adjusting the voltage applied to each phase of the electromagnets, an fairly uniform rotating magnetic field can be obtained at the center of electromagnets. A Hall effect probe was used to measure the strength of RMF in a cylindrical coordinates. The origin of the cylindrical coordinate is the center of the electromagnet. First, the Hall effect probe was placed at the origin position in the middle of electromagnets. The strength RMF(θ) of the magnetic field was measured along the azimuthal direction (θ). The RMF(θ) measurement was carried out by rotating the probe in a 10° increment until the probe was back to the starting position. Second, the strength RMF(z) of the magnetic field was measured along the vertical direction (z) at the center of the electromagnets. Each measurement was carried out with an interval of 0.5 cm away from the origin position along the z-axis. Third, the strength RMF(r) of the magnetic field was measured along the radial direction (r). Each measurement was carried out with an interval of 0.5 cm away from the origin position along the r-axis. One component of RMF(r) is RMF(r(r)), which was the magnetic field strength measured along a r-axis when the probe was perpendicular to the r-axis. Another component of RMF(r) is RMF(r(Q)), which was the magnetic field strength measured along the r-axis when the probe was parallel to the r-axis.

The furnace that was used to heat the sample is placed in the middle of the electromagnets. It is made of a ceramic outer shell to allow penetration of the electromagnetic field. The heating elements are wound longitudinally to minimize the effect on the RMF inside the furnace of the magnetic field generated by the ac current through the heating element during heating. It was found that an approximately 2% reduction in the strength of the RMF occurred when an 8 amp AC current was used to heat up the furnace.

A MicroE Gold 1400 transmissive rotary encoder was used to measure the angular displacement of the ampoule. It consists of a sensor and a diffraction grating plate. Using a MC2000 motion board provided by MicroE, the resolution of the angular displacement is less than 2.7□10-7 degrees. A Visual Basic program was developed to communicate with the MC2000 motion board and to record the angular displacement of the ampoule. The maximum frequency of the data acquisition of the MC2000 motion board is 40 Hz.

The ampoule and the encoder system are enclosed in a vacuum chamber. The pressure in the chamber is maintained at approximately 2.6×10-4 atm during the measurements. The reduction in the air pressure significantly reduces the background noise associated with the measurements of the ampoule deflection angle. A big change in pressure is also used as an indicator of ampoule failure due to the high vapor pressure of the melt sample. When the pressure exceeds a pre-selected set point, in cases of ampoule failure, the power to the transient torque viscometer would be automatically turned off to keep the sample from continuously heating up.

6.3. Results and Discussion

A seven nines grade mercury (47.1 grams) sample was sealed in a fused silica ampoule (approximately 10 cm long with a 9 mm nominal inner diameter and 15 mm nominal outer diameter). The ampoule was positioned in the middle of the electromagnets, as indicated in the schematic of the transient torque viscometer (Fig. 6.1). The data acquisition system for measuring the deflection angle of the ampoule was initialized when the liquid mercury was approximately motionless in the ampoule. At this point, the RMF was turned on. The interaction between the RMF and the mercury generated a Lorentz force which induced a liquid flow in the same direction as that of the RMF. The flow in the mercury sample caused the ampoule to rotate around its vertical axis. At the same time, the torsion fiber provided a restoring torque which induced a torsional oscillation of the ampoule.

Fig. 6.2 shows the ampoule deflection angle of mercury at 377 K versus time, which was measured using the transient torque viscometer. Initially, the sample and the ampoule were at rest, and there was a small oscillation noise around the equilibrium position of 0 degree angle. An RMF of approximately 71 Gauss was turned on at about 77 s. The ampoule immediately responded to the mercury flow induced by the Lorentz force and started to rotate. At the same time, an oscillatory motion was superimposed on the ampoule rotation due to the restoring torque generated by the torsion fiber. The amplitude of the oscillation was approximately 0.4 degree, and its period was approximately 16 s. After about 100 s, the flow in the mercury was no longer accelerated by the RMF, and the ampoule oscillated around the new equilibrium position of approximately –1.0 degree. At about 263 s, the RMF was turned off. After another 100 s, the flow due to the RMF was diminished, and the ampoule oscillated around the original equilibrium position at a 0 degree angle. From the experimental curve shown in Fig. 38, the electrical conductivity and viscosity of mercury can be determined. The principle and theory behind the determination of the electrical conductivity and the viscosity from the data shown in Fig. 38 are discussed in the following sections.

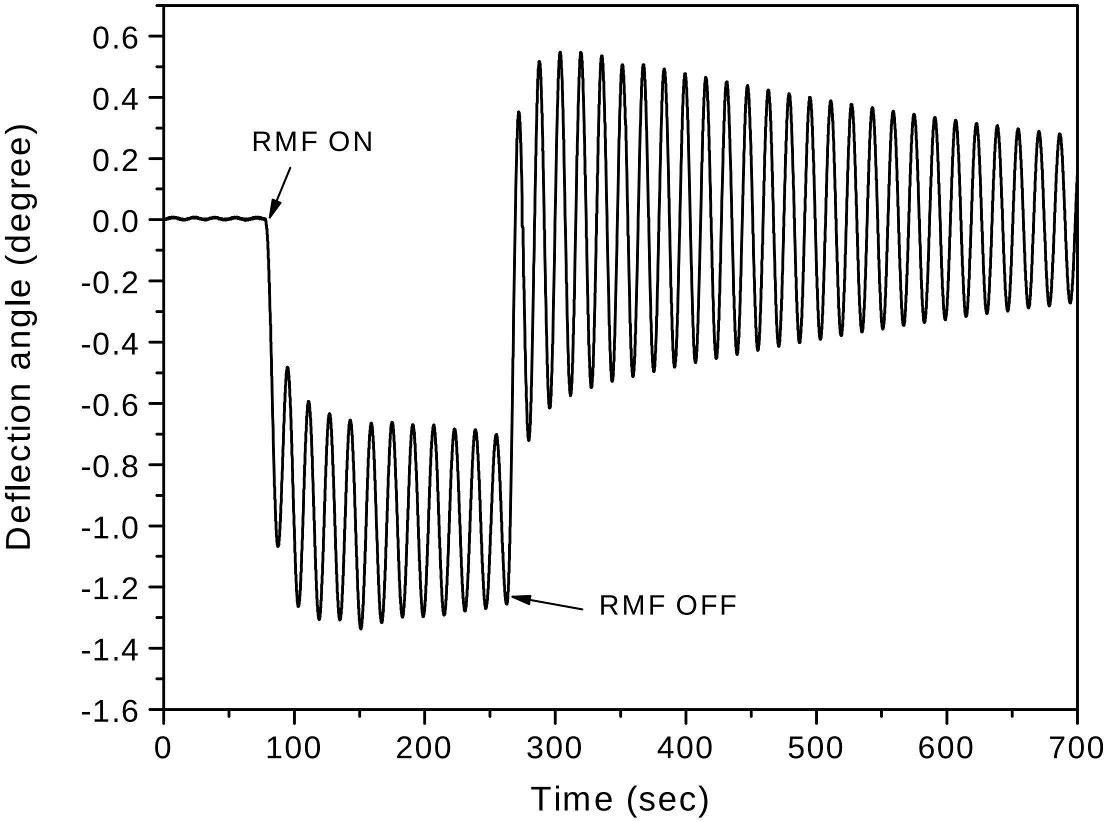

Fig. 6.2. Measured ampoule deflection angle vs. time for mercury at 377 k.

To determine the electrical conductivity and viscosity, the instrument parameters, namely the moment of inertia (*I*), the damping coefficient (*C*), and the torsional spring constant (*k*) for each fiber-ampoule assembly, must be determined accurately, as well as the strength of the RMF (B_0). Specifically, the instruments parameters (*I*, *C*, *k*) of each ampoule assembly, which were used in each numerical analysis (numerically solving Eqs. 14-21) to determine the electrical conductivity and the viscosity, need to be determined, due to the slight difference of each individual ampoule assembly. The method used to determine instrument parameters (*I*, *C*, *k*) is the same method used in the oscillation cup method described by Thresh. This method uses an RMF-free oscillation process at room temperature by adding two additional metal rings with known different moments of inertial (ΔI_1 and ΔI_2) to the torsional oscillation system. B_0 is accurately calibrated experimentally using either a solid or liquid with known electrical conductivity by conducting a transient torque experiment. B_0 only needs to be measured once for the viscometer. The theory and procedures for determining the instrument constants (*I, C, k*) and B_0 are described in detail below.

The rotation angle of the ampoule assembly, $\alpha(t)$ at time t, can be expressed by a different form of Eq. 14 as follows:

$$I\frac{d^2\alpha(t)}{dt^2}+2I\omega_0\Delta_0\frac{d\alpha(t)}{dt}+I\omega_0^2\left(1+\Delta_0^2\right)\alpha(t)=M(t), \qquad \text{Eq. 6.4}$$

where I is moment of inertia of the ampoule assembly without a sample, $\omega_0 = 2\pi/T_0$ is the oscillation frequency of the empty ampoule assembly in a vacuum, T_0 is the corresponding period of oscillation, and Δ_0 is the damping logarithmic decrement for the fiber-ampoule assembly without a sample. $M(t)$ is the torque on the inner ampoule wall, which is generated by the interaction of the RMF and the sample in the ampoule. The damping coefficient, C, and spring constant, k, can be expressed by:

$$C=2I\omega_0\Delta_0 \qquad \text{Eq. 6.5}$$

and

$$k=I\omega_0^2\left(1+\Delta_0^2\right). \qquad \text{Eq. 6.6}$$

Since Δ_0 is three orders of magnitude smaller than 1, the spring constant can be rewritten as follows:

$$k=I\omega_0^2. \qquad \text{Eq. 6.7}$$

To calculate C, and k, the moment of inertia of the empty ampoule assembly (I), the angular frequency of the empty ampoule assembly (ω_0), and the logarithm decrement of the empty ampoule assembly (Δ_0) need to be determined.

The moment of inertia of the empty ampoule assembly (I) is determined by measuring the angular frequencies (ω_1 and ω_2) after adding two metal rings with known moments of inertia, ΔI_1 and ΔI_2, on the ampoule assembly containing a sample. It should note that the spring constant (k) is a constant for the torsional system with or without adding the two metal rings on the fiber-ampoule torsional oscillation system. If a metal ring with moment of inertia (ΔI_1 or ΔI_2) is added to the fiber-ampoule torsional oscillation system, the sprint constant (k) can be expressed as follows:

$$k=\left(I+\Delta I_1\right)\omega_1^2 \qquad \text{Eq. 6.8}$$

or

$$k=\left(I+\Delta I_2\right)\omega_2^2 \qquad \text{Eq. 6.9}$$

Therefore,

$$k = I\omega_0^2 = (I + \Delta I_1)\omega_1^2 = (I + \Delta I_2)\omega_2^2 . \qquad \text{Eq. 6.10}$$

By regrouping Eq. 6.10, the moment of inertia (I) of the empty ampoule assembly without the metal ring added can be calculated from the following equation:

$$I = \frac{\Delta I_2\omega_2^2 - \Delta I_1\omega_1^2}{\omega_1^2 - \omega_2^2} . \qquad \text{Eq. 6.11}$$

The angular frequency with the metal ring added on the ampoule-oscillation system, such as ω_1 and ω_2, and the logarithmic decrement with the metal ring added on the ampoule-oscillation system, such as Δ_1 or Δ_2, are determined by the RMF-free oscillation, which is the same as that using the oscillation cup method. It should be noted that the measured RMF-free logarithmic decrement of the amplitude, such as Δ_1 or Δ_2, is not $\mathit{\Delta}_0$ in Eq. 6.4. $\mathit{\Delta}_0$ is the logarithmic decrement of the fiber-ampoule system without a liquid inside the ampoule and without the addition of the metal rings. Δ_1 or Δ_2, are the logarithmic decrement of the fiber-ampoule system with a sample inside the ampoule when the two metal rings were added, respectively. For an RMF-free oscillation, $\alpha(t)$ can also be written in an oscillation motion as follows:

$$\alpha(t) = \alpha_0 + amp \exp\left(-\frac{\Delta/2\pi}{T}t\right)\cos[\omega(t - t_0)], \qquad \text{Eq. 6.12}$$

where α_0 is the initial angular position before the ampoule assembly oscillation starts, *amp* is the amplitude of the oscillation, Δ is the damping logarithm decrement of the ampoule containing a liquid, $\omega = 2\pi/T$ is the angular frequency of the oscillation, T is the corresponding oscillation period, and t_0 is oscillation starting time. By a standard least root-mean-square fitting of the experimental data to Eq. 28, α_0, *amp*, Δ, ω, and t_0 can be obtained. Table 6 lists a fitting result of an ampoule assembly oscillation with a metal ring added and the mercury sample sealed in the ampoule at room temperature. Fig. 40 also shows this fitting curve and the experimental curve of RMF-free ampoule assembly oscillation. After ω_1 and ω_2, and Δ_1 and Δ_2, are determined using this method, the moment of inertia I is calculated from Eq. 6.11. The spring constant k and the angular frequency ω_0 of the fiber-ampoule oscillation system without the sample sealed in the ampoule are then calculated from Eq. 6.10.

Because the sample needed to be sealed in the ampoule before any experimental parameter determination was carried out, it is impossible to measure the logarithmic decrement of the empty fiber-ampoule system ($\mathit{\Delta}_0$). By using an approximation, the logarithmic decrement of a fiber-ampoule system with solid sample sealed in the ampoule ($\mathit{\Delta}_s$) is used instead of the logarithmic decrement of the fiber-ampoule system with no sample inside the ampoule. This is because the damping coefficient of the empty ampoule assembly is mainly from the internal friction inside the fiber and not from the solid sample. For a liquid sample, such as mercury, at room temperature the logarithmic decrement of the empty ampoule system ($\mathit{\Delta}_0$) is used as the value of the logarithmic decrement of the fiber-ampoule system with a solid sealed in the ampoule (Δ_s). In this study with mercury as a sample, a zinc metal sample with high electrical conductivity at room temperature was chosen. Table 7 shows a set of the determined experimental parameters for the numerical analysis.

With all the instrumental parameters (I, C, k) determined, the viscosity and nominal Lorentz force generated by the RMF of the liquid sample can be calculated by the numerical solution of above equations and boundary conditions. The computation uses a control volume method for the flow calculation, with two hundred radial nodes along the radial direction and time steps of 0.01 second. A 4th-order Runge-Kutta method was used. An iterative process is used to solve the coupled oscillation and flow problem simultaneously. A best fitting procedure was used to achieve a least root-mean-square error between the computation result and the experimental data to obtain the viscosity and Lorentz force. Table 8 shows the numerical fitting results for the viscosity and Lorentz force from the experimental data of mercury at different temperatures.

Table 1: Fitting results of the RMF-free oscillation for the mercury ampoule assembly with a metal ring added

Oscillation parameter	Fitting result	Fitting error
α_0 (degree)	-0.01838	0.00004
amp (degree)	2.0242	0.0002
t_0 (sec)	314.0310	0.0003
Δ	4.3×10^{-3}	0.0001
ω (1/sec)	0.35403	0.00001

Table 2: Experimental parameters for a mercury sample at 377 k

Suspension wire	125µm diameter quartz fiber 26.2 cm length
Sample Material	Mercury
Density	1.340×10^{4} kg/m^3
Height	5.392×10^{-2} m
Radius	4.557×10^{-3} m
Suspension System	
Moment of Inertia (I)	1.866×10^{-5} kg m^2
Torsional Spring Constant (k)	2.888×10^{-6} kg m^2/s^2
Damping Coefficient (C)	2.494×10^{-8} kg m^2/s
Angular frequency of RMF	377 Rad/s (60) (Hz)

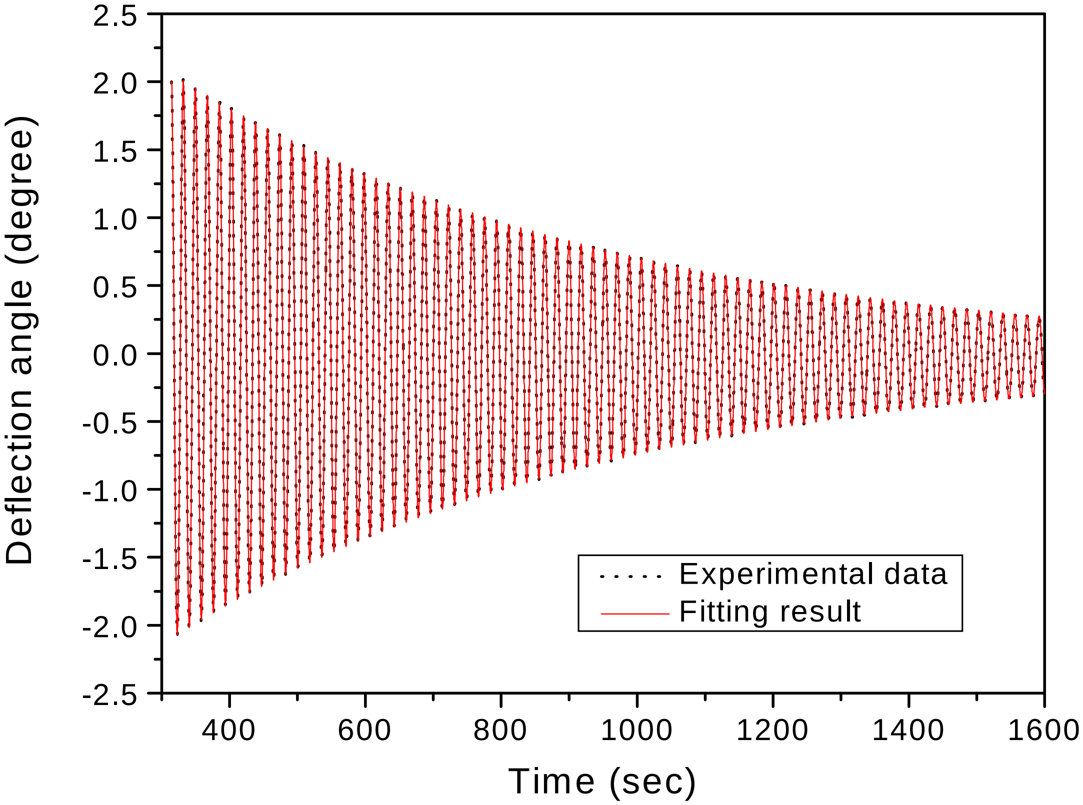

Fig. 6.3. Fitting results and RMF-free oscillation of the ampoule assembly containing a mercury sample sealed in the ampoule at room temperature with a metal ring added.

Table 3: Numerical fitting results for viscosity and Lorentz force from experimental data for mercury sample

Temperature (K)	Kinematic Viscosity (m^2/s)	Lorentz Force (N/m^3)
301.3	1.122×10^{-7}	6.604
326.6	1.038×10^{-7}	6.498
351.8	0.966×10^{-7}	6.389
377.0	0.913×10^{-7}	6.249

The electrical conductivity of liquid mercury can be calculated from Lorentz force using Eq. 19 if the B_0 is known. In our study, B_0 is accurately determined by using a mercury sample at 301.3 K, which has a known electrical conductivity of 1.051×10^6 $\Omega^{-1}m^{-1}$. The Lorentz force of mercury induced by the RMF at 301.3 K was 6.604 N/m^3. B_0 is then calculated from Eq. 17. After the B_0 is determined, the unknown electrical conductivity of the liquid mercury at 326.6, 351.8, and 377.0 K can be calculated from the Lorentz force, which is the fitting result from the numerical analysis, at each temperature. Thus the viscosity and electrical conductivity of mercury is simultaneously determined by the transient torque method.

The results for the viscosity and electrical conductivity of mercury at selected temperatures as determined by the transient torque method are compared in Table 9 with the published data. The published viscosity data for mercury was determined by Menz using the oscillation cup method. The kinematic viscosities of mercury as determined in this study at 301.3, 326.6, 351.8, and 377 K are, respectively, 1.122×10^{-7}, 1.038×10^{-7}, 0.966×10^{-7}, and 0.913×10^{-7} m^2/s. The maximum difference between the viscosity values determined in this study and published values is 1.28%. The published electrical conductivity data of mercury at selected temperatures are measured using four-probe method. In this study the electrical conductivities of mercury at 326.6, 351.8, and 377 K were then determined to be 1.030×10^6, 1.010×10^6, and 0.982×10^6 $\Omega^{-1}m^{-1}$. A maximum difference between the published value of electrical conductivity and that determined in this study at 351.8 K was 1.134%. Overall, there is excellent agreement between the electrical conductivity and the viscosity as determined using the current method and the published electrical conductivity and viscosity data for mercury.

As seen in Table 9, the difference between the published values of viscosity and electrical conductivity and those measured in this study increases as the temperature increases. For the viscosity measurement, the liquid flow cannot be treated exactly as two-dimensional planar and axisymmetric because the temperature in the mercury is slightly non-uniform (about 3K top hotter) along the z-axis. As the temperature of the mercury is increased, the temperature difference between the top and the bottom of mercury sample slight increases. Thus, the increasing difference between the published viscosity values and those determined in this study may be due to this phenomenon. For the electrical conductivity measurement, the standard value was the electrical conductivity value of mercury at room temperature. After the mercury sample was heated, the temperature of the electromagnets was increased. The increased temperature of the electromagnets caused the reduction in the strength of the rotating magnetic field. Therefore, the difference between the published electrical conductivity values and those determined in this study increased as the temperature increased.

Table 4: Comparison of experimental results of mercury with published data

T	Kinematic viscosity (m^2/s)	Electrical conductivity ($\Omega^{-1}m^{-1}$)

(K)	Present	Published (Menz, 1966)	Difference	Present	Published (Dyos, 1992)	Difference
301.0	1.122×10^{-7}	1.121×10^{-7}	0.01%	$1.051\times10^{6*}$	1.051×10^{6}	-
326.6	1.038×10^{-7}	1.040×10^{-7}	0.20%	1.030×10^{6}	1.027×10^{6}	0.25%
351.8	0.966×10^{-7}	0.976×10^{-7}	1.03%	1.010×10^{6}	0.999×10^{6}	1.13%
377.0	0.913×10^{-7}	0.925×10^{-7}	1.28%	0.982×10^{6}	0.972×10^{6}	1.09%

*Standard value

If desired, the transient torque viscometer can also be used as an oscillation cup viscometer. The experimental data from 350 s on, in Fig. 41, is actually oscillation damping by the fluid without RMF stirring. The logarithmic decrement can be obtained to calculate the viscosity of the fluid using Roscoe's equation (Eq. 5). It is apparent from Fig. 41 that the time needed for the oscillation cup measurement is much longer than that for the transient torque method. Fig. 41 also shows that the transient torque numerical simulation result correctly predicts the oscillation cup portion of the experimental data, which is the data after 350 s. In other words, the viscosity results from the two methods are the same in our experimental setup.

7. UNCERTAINTY EVALUATION

7.1. Uncertainty Propagation of Oscillation Cup Technique

The uncertainty resulting from such a viscometer with either viscosity-computation method is not thoroughly explored in previous works and frequently consists of order of magnitude considerations. To explore the uncertainties from such a measurement, numerical simulations of the viscometer were used in this study to estimate viscosity uncertainties using the Monte Carlo method. Such an approach is needed because of the iterative nature of the viscosity computation. The result of the study, the uncertainty level and the extent of the contributions from different parameters, can be used for the design and optimization of oscillating-vessel viscometers.

For the initial design and evaluation with the focus on the uncertainty assessment, numerical simulation of the viscometer is used to estimate viscosity uncertainties through the Monte Carlo method. The simulation computes the system response for a particular set of inputs (viscosity, moment of inertia, spring constant and hysteretic damping), and the viscosity is calculated using two methods: the Roscoe approximate solution and a numerical-fit method. For numerical fitting, a residual function of the logarithmic decay of oscillation amplitude and oscillation period is developed to replace the residual function of angular oscillation, which is mathematically stiff.

The results of this study indicate that the method using computational solution of the equations and fitting for the parameters should be used, since it almost always out-performs the Roscoe approximation in uncertainty. The hysteretic damping and spring stiffness uncertainties translate into viscosity uncertainties almost directly, whereas the moment of inertial and vessel-height uncertainties are magnified approximately two-fold. As the hysteretic damping increases, so does the magnification of its uncertainty, therefore it should be minimized in the system design. The result of this study provides a general guide for the design and application of all oscillation-vessel viscosity measurement systems.

7.2. Monte Carlo Methods

The governing differential equations of flow and oscillation are simplified by the assumption that the flow is one-dimensional inside a long, oscillating cylinder. The fluid flow and vessel oscillation equations are solved numerically to simulate the behavior of the system after release from an initial displacement, thereby generating a system response in the form of angular oscillation verses time after release. Two methods of computing viscosity from the system response are considered: Roscoe's approximate analytical method and a numerical-fit procedure. The expected viscosity uncertainty from each computation method from a system response is quantified using Monte Carlo uncertainty analysis.

The simulation computes the system response for a particular set of material and geometric inputs (viscosity, moment of inertia, spring constant and hysteretic damping) by numerically solving the system's governing differential equations, using second-order finite differences in space and a second-order Runge–Kutta method in time.

To quantify the uncertainty from indirect computational methods such as the Roscoe's and the numerical-fit viscosity computation, Monte Carlo uncertainty analysis was performed using a particular viscometer, and the results from the analysis are only valid for that exact configuration. In this procedure, an uncertainty was assumed for one or more of the viscometer's design parameters and from these assumed uncertainties a set of viscometer designs were generated which vary from the device of interest according to the assumed uncertainties in a Gaussian fashion. This set of theoretical viscometers served as inputs to a series of simulations to compute each viscometer's system response for a known viscosity. Using this set of system responses as inputs to a viscosity-computation algorithm (Roscoe or numerical-fit), a set of viscosities were computed. Because the uncertainties are built into the input distribution, the resulting viscosity distribution differed from the actual viscosity; it is this difference which allowed the uncertainty to be computed. A diagram of the process is shown in Figure 7.1.

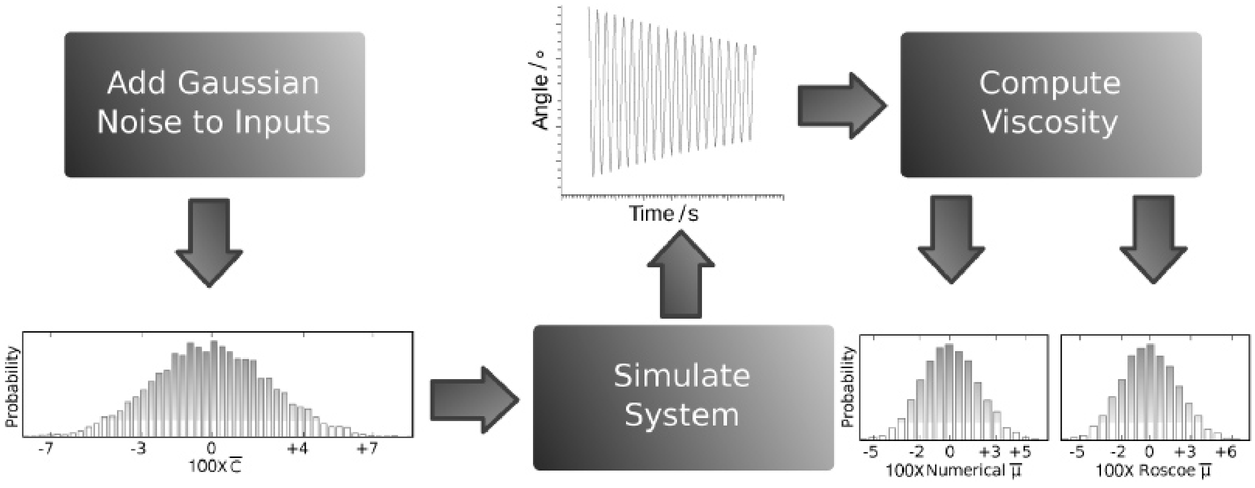

Figure 7.1. Monte Carlo uncertainty analysis.

As can be seen in figure 7.1, an input distribution was generated for parameters and used as input to series of simulations. Each simulation produced the system response for a particular value from this distribution. The set of system responses which correspond to the distribution of ***C*** were used as inputs to the viscosity computation. The viscosity computation was given all the data concerning the inputs except for the parameter of interest. For that parameter, only the mean of the input distribution was given to simulate the uncertainty in that parameter. Using an inaccurate value as an input to the viscosity computation results in a error in the computed viscosity. Thus, a distribution of viscosities was produced from each computation method which corresponds to the input distribution used. Comparing the viscosity distribution against the input distribution yields important information about the uncertainty due to any particular parameter (Colman, 2009, Greenland, 2001, Cox, 2006). To ensure the validity of the results, enough points were considered in the distributions so that they accurately approximate the chosen distribution.

7.3. Uncertainty Results and Discussion

The Monte Carlo uncertainty program was run with both the Roscoe and numerical-fit methods to analyze the uncertainties expected from a viscometer similar to one used to measure mercury. By using parameters from the mercury viscometer, the choice of values for the simulations is reasonable and relevant. Comparing the computed viscosity to the input viscosity yields the error. Many simulations are run in Monte Carlo fashion to characterize the error of each method across a range of input parameters.

7.3.1. Code Performance

Because the numerical viscosity computation and the Monte Carlo process both require many system simulations to be executed, the total computational cost of the code is quite large.

Fortuitously, the code is easily parallelized to run on a cluster computer, thereby dramatically reducing the actual real time of the computation. All computations were done on a small 12-core 64-bit AMD Athlon cluster in less than 24 h.

7.3.2. Predicted Uncertainties

The results of the simulations are presented in figure 7.2 in terms of the relative uncertainty of viscosity ***μ*** as a function of one specific parameter and the uncertainty of that parameter at 1% or 5%. Four lines are presented in each plot, two for each method of viscosity computation. The two series represent the 1% and 5% relative uncertainty of the input variable at a 95% confidence level, while the plots show the uncertainty in the computed viscosity at a given range of parameter.

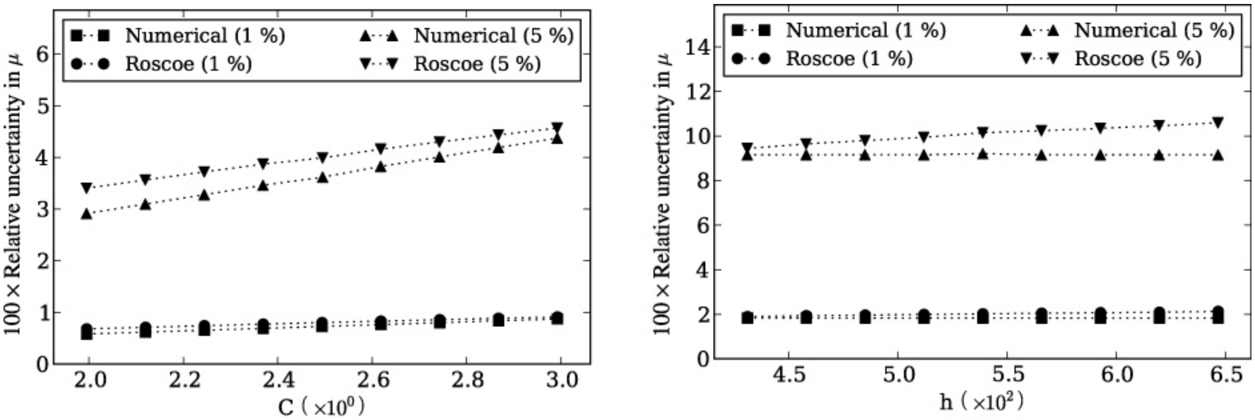

(a) Uncertainty from hysteretic damping

(b) Uncertainty from vessel height

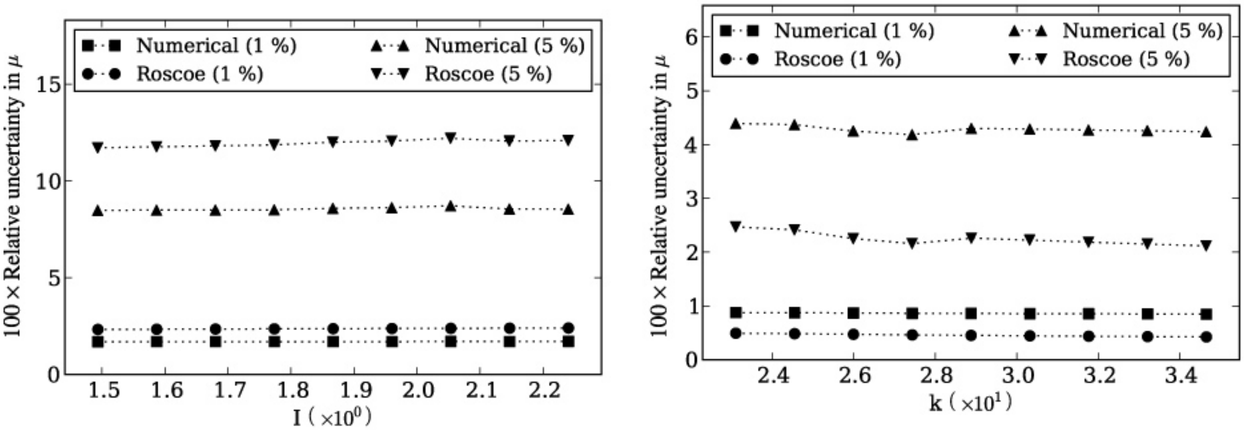

(c) Uncertainty from moment of interia

(d) Uncertainty from spring stiffness

Figure 7.2. Viscosity uncertainty computed using either Roscoe's or the numerical method at specified parameter value and its uncertainty range of either 1% or 5%.

A trend to consider is the increasing uncertainty of both methods with increasing hysteretic damping in the suspension thread, shown in figure 7.2(***a***). This suggests that the hysteretic damping must be either very well known or kept to a very small value to minimize the uncertainty in viscosity results. Ideally, the value of the hysteretic damping constant should be very small and accurate. The uncertainty in viscosity is shown to be almost independent of the range of values of vessel height $\boldsymbol{h}$, moment of inertia $\boldsymbol{I}$ and spring stiffness $\boldsymbol{k}$. Therefore, the design of the viscometer should only minimize the uncertainty of these parameters rather than their values.

The uncertainty due to the moment of inertia ($\boldsymbol{I}$) and the vessel height ($\boldsymbol{h}$) is approximately magnified by a factor of two as shown in figure 7.2, while the uncertainty from the hysteretic damping $\boldsymbol{C}$ and spring stiffness $\boldsymbol{k}$ is approximately the same as the input uncertainty. Thus, the accuracy of the first two values is critical to obtaining accurate results.

Figure 7.3 shows the viscosity uncertainty as the uncertainty of an input parameter changes. The increase of uncertainty in viscosity is shown to increase linearly with the parameter uncertainty. The combined overall uncertainty for the case of all inputs being equally uncertain is shown in figure 6. A major advantage of the Monte Carlo uncertainty method over the Taylor's series method is that correlated uncertainties are included in the analysis. Additionally, even though the range of variables examined is fixed for each computation, they can be varied to explore any potential viscometer design, so long as the assumptions made in the derivation of the governing differential equations are maintained.

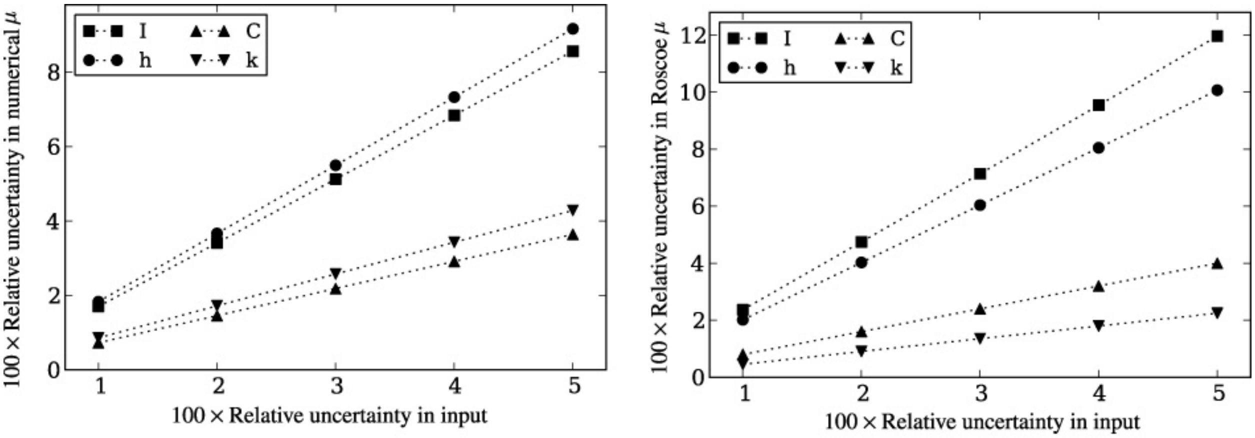

(a) Numerical-fit method

(b) Roscoe method

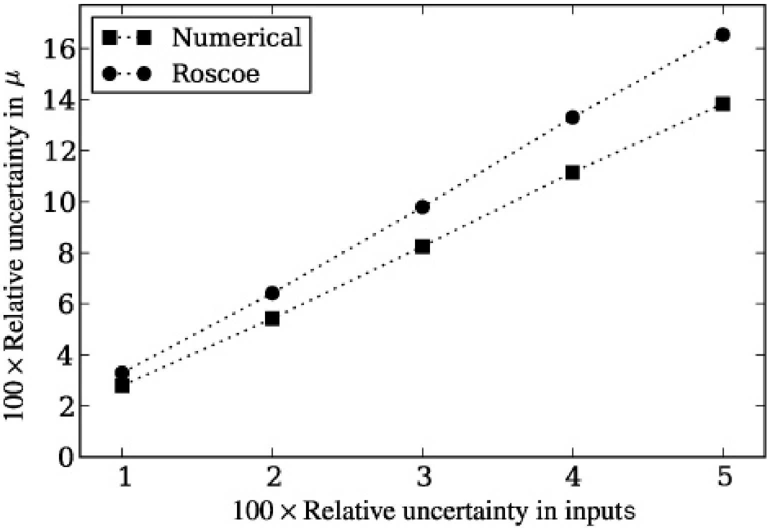

Figure 7.3. Overall uncertainty in viscosity as a function of the uncertainty range of parameters.

The results obtained from these simulations agree reasonably well with the work of Gruner and Hoyer (2009). Although the methodologies used were somewhat similar, the parameters which were varied and the combination of their effects makes it difficult to compare their results directly with those obtained in this work. If one assumes that the input uncertainties are all in the 0% to 3% range, then figure 7.3 suggests that their results fall in the same range as those reported here.

From these results it can be observed that the hysteretic damping in the suspension thread should be as low as possible to minimize the uncertainty increase associated therewith. Additionally, any measurement of the moment of inertia or vessel height should be very precise, since the relative uncertainty in that measurement will be effectively doubled in the computed viscosity.

7.4. Sensitivity of Transient Torque Method

7.4.1. Introduction

The equations of motion are solved numerically during the curve fit, since no analytical solutions are known for this system. The numerical solution uses the control volume finite element method (CVFEM) to discretize the equations in space, while a Crank-Nicholson method is used for time integration. This results in a method that is formally second order in space and time, and also very stable from the implicit component of the time integration.

Because CVFEM solvers are not commonly encountered, a brief overview of the method is provided here. As the name of the method suggests, CVFEM solvers result from the combination of ideas from traditional finite volume (FVM) and finite element methods (FEM) (Rousse, 2000). A FEM-style mesh and shape functions are used to discretize the domain and provide an interpolated solution between grid points. This allows the method to be used as complex geometries, or to provide clustered nodes near important features. Using this discretization control volumes (often called cells) are defined around the nodes in the mesh, and using the divergence theorem a conservation law can be enforced for each volume; this technique is sometimes called a dual-mesh, since the same domain is broken up into both elements and cells. A diagram of the elements and control volumes used in this solver is found in figure 2.

To enforce a conservation law, traditional FVM methods are used for each cell. The conservation equation is integrated over space and time, the divergence theorem is applied, and approximations are then used for most terms in the resulting expression. The results of the first two steps for the present problem are listed in equation (9). CVFEM solvers differ from more traditional FVM solvers in the last step by using the interpolation from the finite elements to provide the approximations for terms instead of local finite difference methods. The use of finite differences in FVM solvers has led some to call them finite difference methods (FDM), or more correctly, CVFDM; the latter name should be preferred to distinguish them from both CVFEM solvers and simpler FDM solvers.

$$\begin{aligned}\left[\int_V \rho V_\phi \mathrm{d}V\Big|_{\Delta t}\right] &= \int_{\Delta t}\int_V \rho f_\phi \mathrm{d}V\mathrm{d}t \\ &+ \int_{\Delta t}\int_{\partial V} \mu \nabla V_\phi \cdot \overrightarrow{\mathrm{d}S}\mathrm{d}t \\ &- \int_{\Delta t}\int_V \mu \frac{V_\phi}{r^2}\mathrm{d}V\mathrm{d}t\end{aligned} \tag{9}$$

For a more general solver it is desirable to move all the terms in equation (9) to one side and then call the expression the residual for the cell, as shown in equation (10). When the residual is zero, the conservation law holds for the the cell and the governing equation is satisfied in an integral sense. To solve the system at each time step, the residuals for all cells are forced to zero.

$$\begin{aligned}R(V_\phi) = &\left[\int_V \rho V_\phi \mathrm{d}V\Big|_{\Delta t}\right] \\ &- \int_{\Delta t}\int_V \rho f_\phi \mathrm{d}V\mathrm{d}t \\ &- \int_{\Delta t}\int_{\partial V} \mu \nabla V_\phi \cdot \overrightarrow{\mathrm{d}S}\mathrm{d}t \\ &+ \int_{\Delta t}\int_V \mu \frac{V_\phi}{r^2}\mathrm{d}V\mathrm{d}t\end{aligned} \tag{10}$$

A novel method is used to incorporate the solid body rotation into the simulation; a boundary element was created which accounts for the momentum transport between the fluid and body, thus coupling the two systems through the same momentum transport mechanics as in the fluid solver. This element references the current ampoule displacement angle to compute the reactive force of the spring. The angle itself is simply the time integration of the body’s angular velocity.

The residual contribution from the solid body mechanics is shown in equation (11), where ***M*** is the moment of inertia converted into an effective mass at the outer radius of the ampoule.

$$
\begin{aligned}
R\left(V_\phi\right) &= M\frac{\mathrm{d}V_\phi}{\mathrm{d}t} + CV_\phi + k\alpha \\
&= \int_{\Delta t} M\frac{\mathrm{d}V_\phi}{\mathrm{d}t}\mathrm{d}t + \int_{\Delta t}\left(CV_\phi + k\alpha\right)\,\mathrm{d}t \qquad (11) \\
&= \left[MV_\phi\big|_{\Delta t}\right] + \int_{\Delta t}\left(CV_\phi + k\alpha\right)\,\mathrm{d}t
\end{aligned}
$$

A multivariate Newton s method is used to solve the equations at each step, although only a single iteration is required since the problem is linear. This method was chosen because the mathematics of the solver are straight forward and allow for added complexity if it becomes needed. The method comes from the Taylor's series expansion of the residual vector for all degrees of freedom in the problem, as seen in (12). By forcing the perturbed residual to zero and recognizing the residual's derivative as the Jacobian, the final method is found in equation (13).

$$
\overline{R}\left(\overline{V}_\phi^i + \overline{\delta}\right) = \overline{R}\left(\overline{V}_\phi\right) + \frac{\partial\overline{R}}{\partial\overline{V}_\phi}\left(\overline{V}_\phi^i\right)\overline{\delta} + \mathrm{H.O.T.} \qquad (12)
$$

$$
\begin{aligned}
\underline{J}\left(\overline{V}_\phi^i\right) &= \frac{\partial\overline{R}}{\partial\overline{V}_\phi}\left(\overline{V}_\phi^i\right) \\
\overline{R}\left(\overline{V}_\phi^i + \overline{\delta}\right) &\rightarrow 0 \qquad\qquad (13) \\
\underline{J}\left(\overline{V}_\phi^i\right)\overline{\delta} &= -\overline{R}\left(\overline{V}_\phi\right)
\end{aligned}
$$

Evaluation of the Jacobian $\underline{J}$ is accomplished through automatic differentiation. Since the simulation is written in Fortran 2003, this is implemented using operator overloads on a dual number derived data-type which uses the chain rule to track derivatives of calculations made. Automatic differentiation has applications in several areas, including the evaluation of Jacobian matrices for Newton iteration (Spall, 2013). The system of equations that result from (13) are tridiagonal in form and are solved using a version of the Thomas algorithm.

During simulation runs, the spatial and temporal discretizations were refined until the solution no longer changed appreciably.

7.4.1.1. 3.2. Curve fitting

A curve fit is used to match the viscosity and magnetic force constant needed to duplicate the results from experiment. This is done by first fitting a tension spline to the experimental data, which allows it to be sampled at arbitrary points in time. Next, a candidate fit is compared against this spline by defining a residual function $R(\nu, f_0) = \sqrt{\sum_i \left[\left(\alpha_s(t_i) - \alpha_e(t_i)\right)^2\right]}$, where $\alpha_s(t_i)$ is the simulation s angle and $\alpha_e(t_i)$ is the experiment s angle at the discrete time value $\boldsymbol{t_i}$. This residual function is then minimized using the Nelder-Mead simplex method with the inputs limited to a variation of no more than 20% of the nominal value (Olsson, 1975).

3.3. Sensitivity studies

Since previous studies of the uncertainty in oscillating cup viscometer measurements noted a linear relationship between the uncertainty of input parameters and the resultant uncertainty of the viscosity, a full Monte Carlo simulation was deemed unnecessary for the present work (Horne, 2012). Since the experimental data from the only RMF viscometer experiment is available for use, the parameters of that physical experiment were used as the baseline values for the simulations, and deviations from this baseline were simulated.

The effects of each input parameter were first considered by trying to fit the experimental data using the numerical simulations, but with the parameter of interest perturbed by a relative value. This potentially resulted in altered fit results for the sample viscosity and or body force constant. The relationship between the input error and the output error (assuming the experimental data to be correct) is the subject of the present study.

In addition to single-parameter studies, certain combinations of input parameters were systematically varied simultaneously and independently to look for effects on the results from variation in two parameters. While initial efforts included a full parameter space exploration, the results showed that only two input parameters must be simultaneously considered to capture all effects of interest; this fact, combined with the computational cost of full parameter space exploration, resulted in only two parameter comparisons being made.

7.4.2. 4. Result and analysis

To ensure that the assumed values for the simulations are relevant, the design parameters from viscometer in the literature were selected for this work. The experimental parameters of the measurement under analysis can be found in Table 5.

Table 5. Experimental parameters and conditions.

Parameter	Symbol	Value	Units
Material	Hg	Mercury	---
Temperature	T	377	K
Density	ρ	13.384x10^{3}	Kg-m^{-3}
Viscosity	ν	92.1x10^{-9}	m^{2}-s^{-1}
Body force constant	f_0	?4.683x10^{-4}	N-kg^{-1}
RMF Frequency	ω	377.0	rad-s^{-1}
Moment of inertia	I	1.867x10^{-5}	Kg-m^{2}
Damping constant	C	2.494x10^{-8}	N-m-s

Parameter	Symbol	Value	Units
Spring constant	k	$2.888\text{x}10^{-6}$	N-m
Height of ampoule	h	$53.9\text{x}10^{-3}$	m
Radius of ampoule	R	$4.557\text{x}10^{-3}$	m

Experimental data was compared against the simulation results for the baseline viscometer and refined in space and time until an adequate match was obtained. The actual simulations are refined slightly beyond this level to allow for tighter step size requirements as the input parameters are varied. A comparison of the simulation and experimental data is shown in Figure 7.4.1.

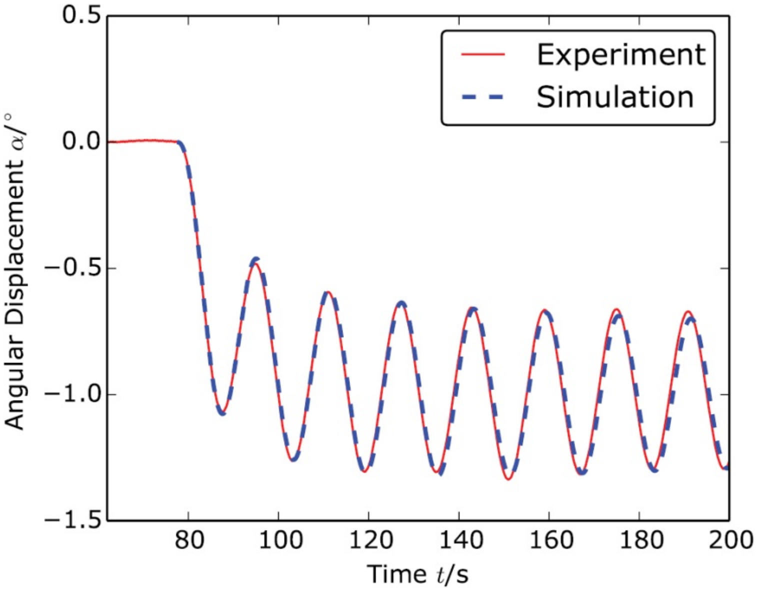

Figure 7.4.1: Comparison of simulation with experimental data

The simulation is begun right at the moment when the RMF is switched on, since prior to this the system is at rest. The transient response of the viscometer can be clearly seen as it adjusts motion of the sample induced by the magnetic field, and the momentum gained from the transition starts an oscillation of the system similar to conventional viscometer operation.

The results of the sensitivity analysis for both the sample viscosity and body force constant versus all the considered input parameters can be found in Figure 7.4.2. The most noticeable characteristic of the sensitivity results is the noise in the results, which is caused by regression error in the curve fitting process. While this could be cleaned up by tightening the convergence criteria for the curve fitting process and smoothing neighboring points, leaving the noise present in the results presents a better representation of the errors as they are likely to occur in an actual measurement.

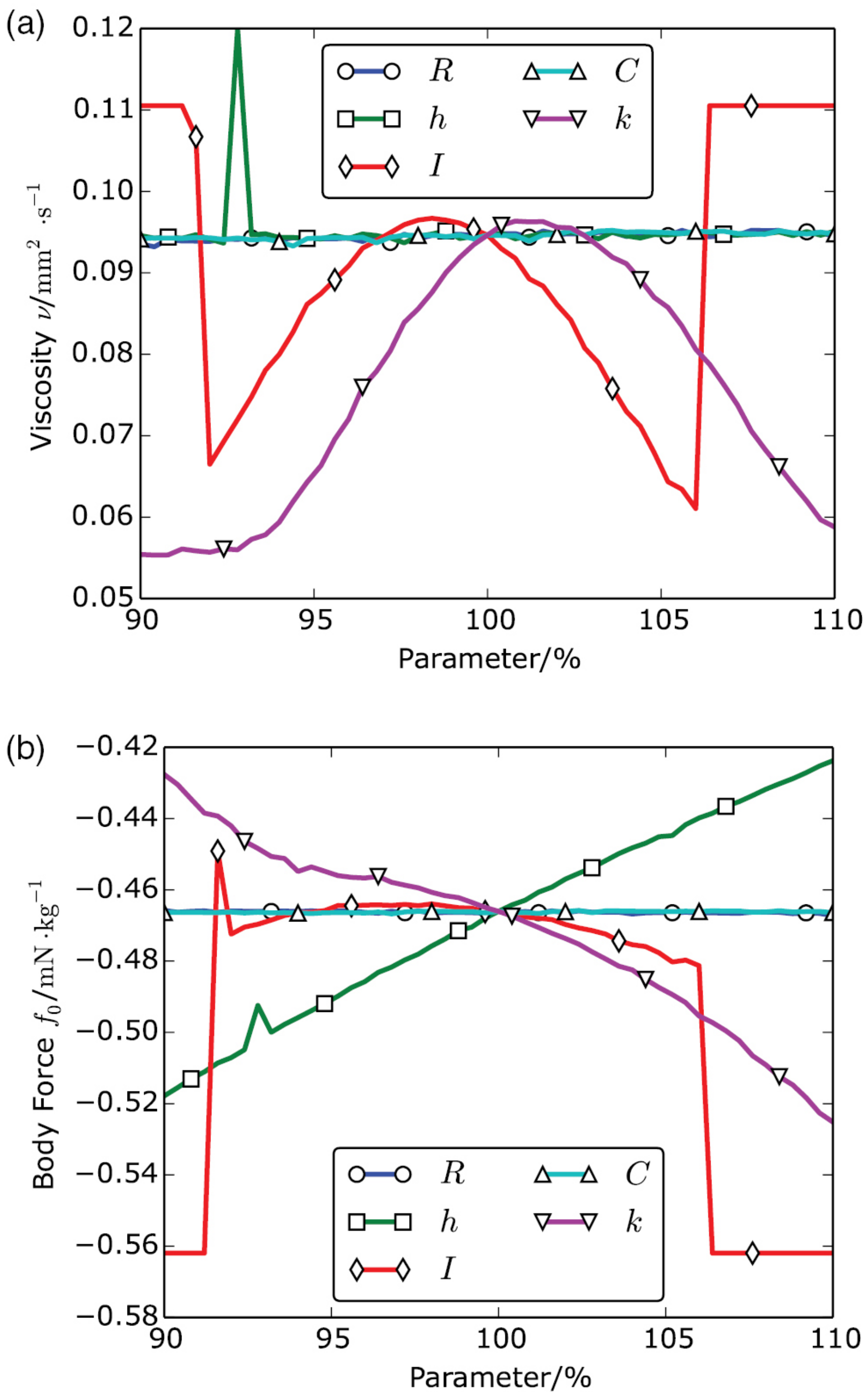

Figure 7.4.2. Variation of the viscosity and body force constant (f_0) versus error in input parameters. (*a*) viscosity variation versus errors, (*b*) body force constant variation versus errors.

Also easily observed is the regression failure present in the results when the moment of inertia (***I***) is too far off the actual value. This is caused by the change in oscillation period cause by variation in $\boldsymbol{I}$ which cannot be accounted for by other variables, especially the viscosity and body force constant, and has been observed in previous analysis (Horne 2012). This problem can be remedied by allowing $\boldsymbol{I}$ to vary during the fitting process and then verifying that the fitted moment of inertia matches the measured value afterwards. Otherwise, it can be seen from the data that it must be known to within 5% to obtain a fitted result, and that even within that range any error in $\boldsymbol{I}$ will strongly affect the computed viscosity. The effects from error in $\boldsymbol{I}$ on $\boldsymbol{f}_0$ are much less pronounced than for viscosity, since the magnetically induced fluid velocity has the strongest influence on the angular offset caused by the motion, and not the oscillations which the moment of inertia has such a profound effect on.

Further inspection of Figure 7.4.2 shows that two of the considered input parameters seem to have no systematic effect on the fitted results whatsoever; these parameters are the vessel's outer radius ($\boldsymbol{R}$) and the damping constant of the suspension thread ($\boldsymbol{C}$). While it may surprise no one that the vessel radius can cancel out all of the calculations, the insignificance of the damping constant is interesting and specific to the RMF viscometer operation. In the traditional oscillating cup viscometer method, the logarithmic decrement from which the viscosity is computed includes effects from both the viscous fluid flow and the hysteretic damping within the suspension thread; the latter value must be known to compute the former, as the two affect the system oscillation in roughly the same manner. For this property to be unimportant to the RMF-based viscometer represents a significant advantage and must be a consequence of the measurement's reliance on transient behavior instead of semi-steady state operation.

The error caused in the body force constant seems to directly relate to errors in the thread spring stiffness. This can be explained by the fact that both the body force constant and spring constant have a strong effect on the offset angle at which the system oscillates after the RMF is activated. An increase in spring constant will decrease this angle as the same viscous drag from the sample results in less displacement, while an increase in body force constant will increase the displacement as a greater fluid velocity, and thereby, viscous drag is induced. These effects are readily seen in the figure as $\boldsymbol{f}_0$ decreases to compensate for increases to $\boldsymbol{k}$. Nonlinearity in the momentum conservation equation causes the nonlinear relationship between $\boldsymbol{f}_0$ and $\boldsymbol{k}$.

It is interesting to note the similarity of the error in viscosity due to the moment of inertia and spring constants, where both show a roughly parabolic trend offset from the correct value. The similar behavior of the two parameters can be explained by their close relation in the natural frequency of an undamped system, where $f_n \propto \sqrt{k/I}$. Thus, error in either $\boldsymbol{I}$ or $\boldsymbol{k}$ will result in errors in the predicted oscillation frequency of the system, and therefore, to bad fit. The position of $\boldsymbol{k}$ in the numerator of the fraction is likely the reason that moderate (~10%) errors in $\boldsymbol{k}$ do not cause regression failure as they do with errors in $\boldsymbol{I}$. This relationship between $\boldsymbol{k}$ and $\boldsymbol{I}$ was further explored by considering the error in both viscosity and body force constant as a function of spring stiffness and moment of inertial simultaneously. The results of this exploration can be seen in figure 7.4.3.

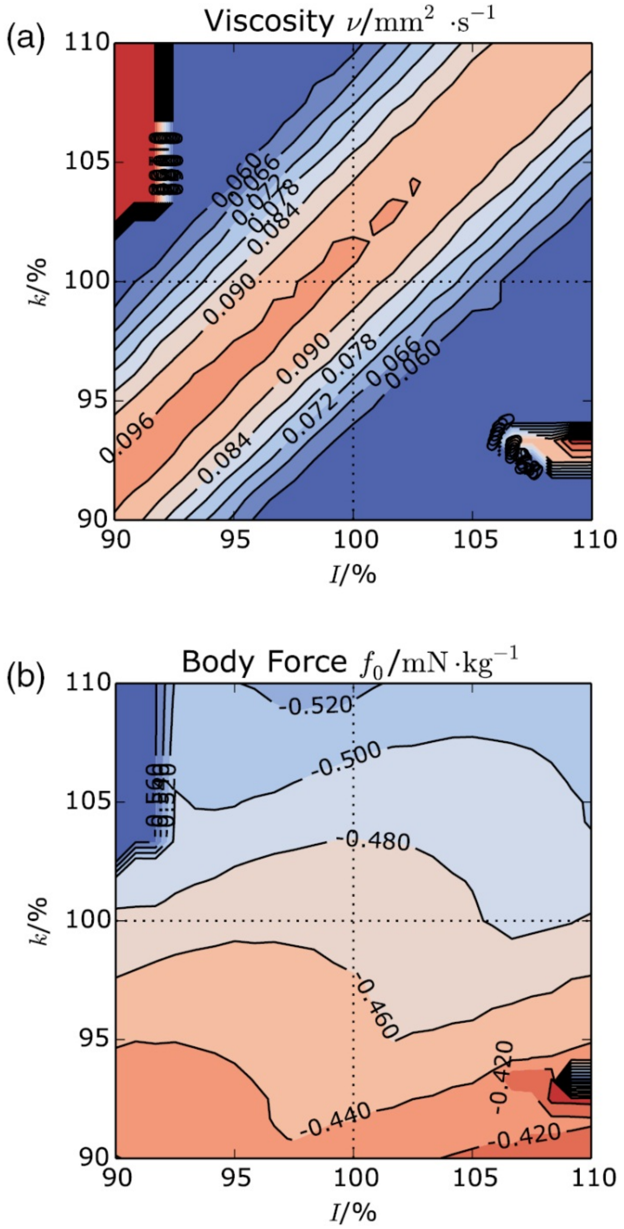

Figure 7.4.3. Variation of the viscosity and body force constant (f_0) versus moment of intertia (I) and spring stiffness (k). (a) Viscosity variation, (b) body force constant (f_0) variation.

The search for correlation between ***k*** and ***I*** in Figure 7.4.3(***a***) proved to be quite fruitful, as the natural frequency explanation of the characteristics in the single variable sensitivity study are confirmed by the new data. It can be clearly seen in the figure that the computed value for the viscosity remains largely unchanged so long as the ratio ***k***/***I*** is held constant as demonstrated by the 45 degree angle visible in the equally-scaled relative errors. Even more convincing is the absence of such a trend in the computed body force constant in Figure 7,4,3(***b***). While the spring stiffness influence on $\boldsymbol{f}_0$ is fairly strong, so long as regression error does not occur, ***I*** has little effect on its value; these trends are clearly visible in the data. Also of note are the regions of regression error visible in both plots of figure 7.4.3 where the ratio k/I deviates too greatly from its correct value.

The vessel height seemingly has little effect on the computed viscosity, while the relationship to the computed body force constant appears to be linear as seen in Figure 7.4.2(***b***). An increase in ***h*** will directly increase the viscous force acting on the viscometer from the fluid, but will not affect the moment of inertia, since the two are assumed to be measured separately. While this results in an increased effect on the mean offset angle with the RMF active, it does not significantly affect the effective damping cause by the fluid on the viscometer. Upon further investigation, the moment of inertia was found to experience a decreased range of regression success with decreased values of ***h***, as can be seen in Figure 7.4.4.

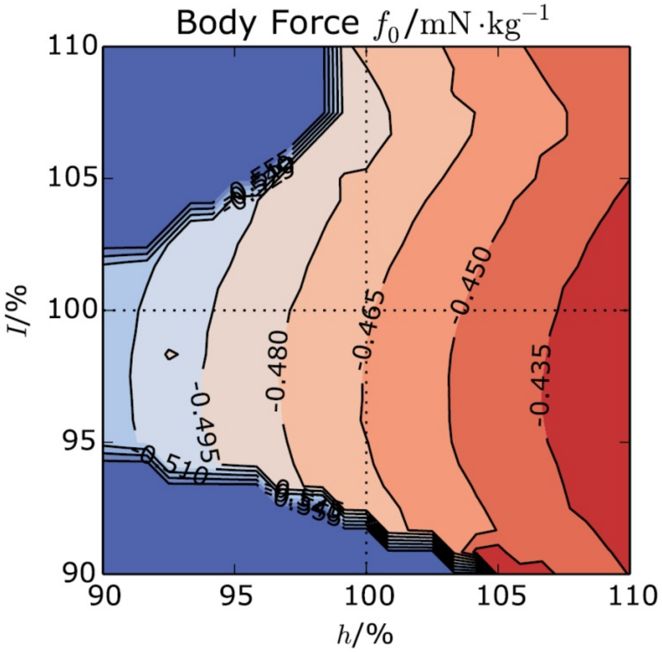

Figure 7.4.4. Body force constant (f_0) versus vessel height (h) and moment of inertia (I).

The derivatives of both the body force constant and viscosity as computed in the sensitivity studies are found in Table 6. Assuming a roughly linear relationship between input and output, which seems reasonable given the data, the expected measurement uncertainties can be computed using the Taylor's series method of uncertainty propagation without the need for a full Monte Carlo simulation.

Table 6: Computed derivatives for each input parameter.

	Viscosity		*Body force constant*	
	Derivative	Units	Derivative	Units
R	$1.47\text{x}10^{0}$	$\frac{\text{mm}^2\text{s}^{-1}}{\text{m}}$	$-5.08\text{x}10^{-1}$	$\frac{\text{mNkg}^{-1}}{\text{m}}$
h	$5.58\text{x}10^{?2}$	$\frac{\text{mm}^2\text{s}^{-1}}{\text{m}}$	$8.54\text{x}10^{0}$	$\frac{\text{mNkg}^{-1}}{\text{m}}$
I	$1.34\text{x}10^{4}$	$\frac{\text{mm}^2\text{s}^{-1}}{\text{kg}\cdot\text{m}^2}$	$-7.74\text{x}10^{3}$	$\frac{\text{mNkg}^{-1}}{\text{kg}\cdot\text{m}^2}$
C	$3.50\text{x}10^{5}$	$\frac{\text{mm}^2\text{s}^{-1}}{\text{N}\cdot\text{m}\cdot\text{s}}$	$1.53\text{x}10^{5}$	$\frac{\text{mNkg}^{-1}}{\text{N}\cdot\text{m}\cdot\text{s}}$
k	$6.81\text{x}10^{4}$	$\frac{\text{mm}^2\text{s}^{-1}}{\text{N}\cdot\text{m}}$	$-1.18\text{x}10^{5}$	$\frac{\text{mNkg}^{-1}}{\text{N}\cdot\text{m}}$

From the computed sensitivities and assuming that all input parameters are known to within 1% using Gaussian statistics, the expected uncertainties of the new measurement are 1.25% for the body force constant and 3.5% for the viscosity. It must be stressed that these values assume a particular input uncertainty which is, in fact, unknown. These uncertainty results are similar to those found in the literature for the traditional oscillating-cup viscometer design, suggesting that while the RMF viscometer demonstrates numerous advantages, improved precision is likely not one of them.

8. CONCLUSIONS

Metallic fuels have exceptional transient behavior, excellent thermal conductivity, and a more straightforward reprocessing path, which does not separate out pure plutonium from the process stream. Fabrication of fuel containing minor actinides and rare earth (RE) elements is generally done by melt casting in an inert atmosphere. For the design of a casting system and further scale up development, computational modeling of the casting process is needed to provide information on melt flow and solidification for process optimization. Therefore, there is a need for melt viscosity data, the most important melt property that controls the melt flow.

This project investigated in detail viscosity measurement techniques that use fully sealed melt sample with no Americium vapor loss at temperatures relevant to the casting process. The project focused on developing mathematical models to establish the measurement method, building a prototype system, and quantifying the uncertainty range. The result of the project indicates that the oscillation cup technique is applicable for melt viscosity measurement. Detailed mathematical models of innovative sample ampoule designs were developed to not only determine melt viscosity, but also melt density under certain designs. Measurement uncertainty were analyzed and quantified. The result of this project can be used as the initial step toward the eventual goal of establishing a viscosity measurement system for radioactive melts.

The motion of the cup in an electromagnetic viscometer was modeled with the 1D assumption. The motion is decomposed to three components, namely the angular displacement at equilibrium, fast decay, and the damped harmonic oscillation. The impact of experimental design parameters on the angular displacement has been investigated. Based on the understanding of the EMV mechanism, two measurement methods are suggested, and some general guidance are put forward for experimental design. When the rapid method is applied, large cups submerged in weak magnetic field is preferred. In contrast, large Ha is the better choice if using the QSS method.

An analytical model was established for a 2D cylinder EMV. Numerical experiments within common experimental conditions are performed. Experimental data with external noises are firstly generated from the 2D model, and then fitted to determine viscosity and electrical conductance by the rapid method and by the QSS method. The measurement errors are resulted without the consideration of uncertainties of all parameters. Some conclusions are drawn from the analysis of the measurement errors: a) The rapid method has a great advantage over the QSS method with significantly improved accuracy, b) When using the rapid method, $Ha < 0.1$ and $R > 3$ are preferred to obtain relative high measurement accuracy, and c) Measurement of electrical conductance has much higher accuracy than viscosity.

The experimental system showed viability of viscosity measurement using sealed samples. The calibration indicates the data are well in line with published viscosity information. From the results of the uncertainty analysis, several conclusions can be drawn. First, a residual function based on oscillation period and logarithmic decay of oscillation amplitude should be used for numerical fitting. A residual based on angular displacement is mathematically stiff. Second, the numerical-fit method generally produces better results, but the step size for actual computation of viscosity must be kept very small to ensure good results. Third, a larger value of damping generates increased uncertainty; therefore its value should be minimized as much as possible regardless of its uncertainty. The other parameters considered do not exhibit this behavior, thus their values do not need to be minimized. The viscosity uncertainty doubles due to uncertainty in the vessel height $\boldsymbol{h}$ and moment of inertia $\boldsymbol{I}$, therefore these values must be known very accurately. The viscosity uncertainty varies nearly linearly with the uncertainty of either individual parameters or all the parameters. This all demonstrates that the methods used here can be used to design a viscometer that minimizes the resulting uncertainty in measured viscosities.

From the transient analysi, it must be concluded that the error modes in the RMF-based viscometer measurement are quite different from the logarithmic decrement method traditionally used. While the moment of inertia for the viscometer must be accurately known for both methods, other parameters which have great sway on the accuracy of the traditional technique don't matter at all for the RMF variant. These benefits alone would warrant further study, but when combined with the possibility to measure the electrical conductivity and viscosity so rapidly that their variation with temperature could be reasonably developed demonstrates the new methods dramatic superiority for electrically conducting liquids. Given the advantages, even though the resulting viscosity values are likely to be only as precise as the results of the more traditional measurement, the new method is clearly superior to the old. More careful considerations of the viscometer design, as well as even simulated experiments with more advantageous geometries should be conducted.

9. REFERENCES

Bakhtiyarov, S. and R. Overfelt, Electrical conductance measurements in liquid metals by rotational technique. Journal of materials science, 1999. 34(5): p. 945-949.

Beckwith, D.A. and G.F. Newell, Theory of oscillation type viscometers: The oscillating cup. Zeitschrift für angewandte Mathematik und Physik ZAMP, 1957. 8(6): p. 450-465.

Coleman H W and Steele W G 2009 Experimentation, Validation, and Uncertainty Analysis for Engineers (New York: Wiley)

Cox M G and Siebert B R L 2006 The use of a Monte Carlo method for evaluating uncertainty and expanded uncertainty Metrologia 43 S178–88

Dyos, G. T. , T. Farrell, Electrical Resistivity Handbook, Peter Peregrinus Ltd., London, United Kingdom, 1992.

Fedorov, G.B. and Smirnov, E.A., Sov. J. At. Energ. 25 (1968) 795: cited in : P. Chiotti, V.V. Akhachinskij, I. Ansara and M.H. Rand, The Chemical Thermodynamics of Actinide Elements and Compounds, Part 5 IAEA, Vienna, 1981.

Greenland S 2001 Sensitivity analysis, Monte Carlo risk analysis, and Bayesian uncertainty assessment Risk Anal. 21 579–84

Grove, G.R., “Reactor Fuels and Materials Development, Plutonium Research,” 1966 Annual Report, MLM-1402.

Grove, G.R., “Reactor Fuels and Materials Development, Plutonium Research,” 1967 Annual Report, MLM-1445.

Gruner S and Hoyer W 2009 A statistical approach to estimate the experimental uncertainty of viscosity data obtained by the oscillating cup technique J. Alloys Compounds 480 629–33

Gruner, S. and W. Hoyer, The dynamic viscosity of liquid Cu–Si alloys. Journal of Alloys and Compounds, 2008. 460(1): p. 496-499.

Horne K, Ban H, Fielding R and Kennedy R 2012 Monte carlo uncertainty estimation for an oscillating-vessel viscosity measurement Metrologia 49 577

Iida, T., Guthrie, R.I.L., The Physical Properties of Liquid Metals (Clarendon Press, Oxford, 1988).

Kanno, Masayoshi; Yamawaki, Michio; Koyama, Taddafumi and Morioka, Nobuo; “Thermodynamic activity measurements of U-Zr alloys by Knudsen effusion mass spectrometry”, J. Nucl. Mater., 1988, vol. 154, p. 154.

Kehr, M., W. Hoyer, and I. Egry, A new high-temperature oscillating cup viscometer. International Journal of Thermophysics, 2007. 28(3): p. 1017-1025.

Kennedy, J. Rory; Lambregts, Marsha J.; Maddison, Andrew P. “Thermal Conductivity Of Minor Actinide Doped Pu-Zr And U-Pu-Zr Transmutation Fuels,” Transactions of the American Nuclear Society, v 91, Transactions of the ANS - 2004 Winter Meeting, 2004, p 457-458.

Kestin, J. and G.F. Newell, Theory of oscillation type viscometers: The oscillating cup. Zeitschrift für angewandte Mathematik und Physik ZAMP, 1957. 8(6): p. 433-449.

Krall, A., et al., Feasibility of simultaneous viscosity and density measurements of a fluid from the motion of an oscillating disk. Fluid phase equilibria, 1987. 36: p. 207-218.

Li, C., et al., Thermophysical properties of HgTe and Hg< sub> 0.9</sub> Cd< sub> 0.1</sub> Te melts. Journal of Non-Crystalline Solids, 2014. 391: p. 54-60.

Li, C., H. Ban, B. Lin, R. N. Scripa, C.-H. Su, S.L. Lehoczky, Transient Torque Method: A Fast And Non-Intrusive Technique To Simultaneously Determine Viscosity And Electrical Conductivity Of Semiconducting And Metallic Melts, Review of Scientific Instruments, Vol. 75, No. 9, pp. 2810-2816, 2004.

Li, C., R. N. Scripa, H. Ban, B. Lin, C.-H. Su, S.L. Lehoczky, Thermophysical Properties and Structural Transition of Hg0.8Cd0.2Te Melt, Journal of Non-Crystalline Solids, Vol. 351, pp. 1179-1184, 2005.

Li, C., Su, C.-H., Lehoczky, S.L., Scripa, R.N., Lin, B., and Ban, H., Thermophysical Properties of Liquid Te: Density, Electrical Conductivity, and Viscosity, Journal of Applied Physics, Vol. 97, #083513,: pp. 1-7, 2005.

Massalski, T.D., Murrey, J.L., Bennett, L.H.and Bakder, H., “Binary Alloy Phase Diagrams (American Society for Metals, Ohio, 1986, p. 2151

Matsui, Tsuneo; Natsume, Tetsuya and Naito, Keiji; “Heat Capacity Measurements Of U0.80zr0.20 And U0.80mo0.20 Alloys From Room Temperature To 1300 K”, J. Nucl. Mater., 1989, vol. 167, p. 152.

Menz, W, F. Sauerwald, m. V. von, K. Fischer, Acta Metall. 14 (1966) 1617

Nakamura, Jin-ichi; Takahashi, Yoichi; Izumi, Shin-ichiro and Kanno, Masayoshi, “Heat Capacity Of Metallic Uranium And Thorium from 80 to 1000 K”, J. Nucl. Mater., 1980, vol. 88, p. 64.

Nieuwoudt, J., J. Kestin, and J. Sengers, On the theory of oscillating-body viscometers. Physica A: Statistical Mechanics and its Applications, 1987. 142(1): p. 53-74.

Nieuwoudt, J., J. Sengers, and J. Kestin, On the theory of oscillating-cup viscometers. Physica A: Statistical Mechanics and its Applications, 1988. 149(1): p. 107-122.

Ofte, D, Rohr, W.G., J. Nucl. Mater. 15, 231, 1966

Olsson D M and Nelson L S 1975 The nelder-mead simplex procedure for function minimization Technometrics 17 45–51

Rodríguez, R. J., Sari, C. and Criado Portal, A. J., "Investigation of the Np-Zr and U-Zr-Np systems", Journal of alloys and compounds, 1994, vol. 209, p. 263.

Roscoe, R., Viscosity determination by the oscillating vessel method I: theoretical considerations. Proceedings of the Physical Society, 1958. 72(4): p. 576.

Rousse D R 2000 Numerical predictions of two-dimensional conduction, convection, and radiation heat transfer. I. Formulation Int. J. Therm. Sci. 39 315–31

Rousse D R, Gautier G and Sacadura J F 2000 Numerical predictions of two-dimensional conduction, convection, and radiation heat transfer. II. Validation Int. J. Therm. Sci. 39 332–53

Sasaki, H., et al., Temperature dependence of the viscosity of molten silicon measured by the oscillating cup method. Japanese journal of applied physics, 1995. 34(part 1): p. 3432-3436.

Sato, Y., et al., Viscosities of Fe–Ni, Fe–Co and Ni–Co binary melts. Measurement Science and Technology, 2005. 16(2): p. 363.

Spall R E and Yu W 2013 Imbedded dual-number automatic differentiation for computational fluid dynamics sensitivity analysis J. Fluids Eng. 135 014501

Takahashi, Yoichi; Yamamoto, Kazutaka; Ohsato, Tetsuo; Shimada, Hiroshi and Terai, Takayuki, "Heat capacities of Uranium-Zirconium alloys from 300 to 1100 K", J. Nucl. Mater., 1989, vol. 167, p. 147.

Takahashi, Yoichi; Yamawaki, Michio and Yamamoto, Kazutaka; "Thermophysical properties of Uranium-Zirconium alloys", J. Nucl. Mater., 1988, vol. 154, p. 141.

Torklep, K. and H. Oye, An absolute oscillating-cylinder (or cup) viscometer for high temperatures. Journal of Physics E: Scientific Instruments, 1979. 12(9): p. 875.

Touloukian, Y.S., Thermophysical Properties of High Temperature Solid Materials, Macmillan, New York, 1967.

Tsai, H.C, Olander, D.R., The viscosity of Molten Uranium Dioxide, J. Nuc., Mat., 44, 83-86, 1972.

Volz, M. and K. Mazuruk, Thermoconvective instability in a rotating magnetic field. International journal of heat and mass transfer, 1999. 42(6): p. 1037-1045.

Wang, D. and R. Overfelt, Oscillating cup viscosity measurements of aluminum alloys: A201, A319 and A356. International journal of thermophysics, 2002. 23(4): p. 1063-1076.

Woodley, R.E., The viscosity of Molten Uranium Dioxide, J. Nuc. Mat., pp. 103-106, 1974.

Yu W and Blair M 2013 Wenbin yu, maxwell blair Comput. Phys. Commun. 184 1446–52

Zegler, S.T., O'Boyle, D.R., Blumenthal, B., Walter, C.M., and Rhude, H.V., "Structure and Transformations in U-Pu-Zr and U-Pu-Ti Alloys," Annual Progress Report for 1965, Metallurgy Division, ANL-7155.